Combinaison de la diffusion diffuse thermique de la diffusion inélastique des rayons X et des calculs ab inito pour l'étude de la dynamique de réseau

Björn Wehinger

UNIVERSITÉ DE GRENOBLE

THÈSE

Pour obtenir le grade de

DOCTEUR DE L'UNIVERSITÉ DE GRENOBLE

Spécialité : **Physique**

Arrêté ministériel : août 2006

Présentée par

Björn Wehinger

Thèse dirigée par **Alexeï Bosak**
et codirigée par **Michael Krisch**

préparée au sein d'**Installation Européenne de Rayonnement Synchrotron**
et d'**École Doctorale de Physique Grenoble, France**

On the combination of thermal diffuse scattering, inelastic x-ray scattering and *ab initio* lattice dynamics calculations

Thèse soutenue publiquement le **3 Juillet 2013**,
devant le jury composé de :

M Jens Kreisel
professeur et directeur de recherche au CRP Gabriel Lippmann, Belvaux, Président et Rapporteur

M Peter Blaha
professeur de la Technische Universität Wien, Rapporteur

M Hans-Beat Bürgi
professeur de l'Universität Bern et de l'Universität Zürich, Examinateur

M Helmut Schober
chercheur à l'Institut Laue-Langevin, Grenoble et professeur de l'Université Joseph Fourier, Grenoble, Examinateur

M Alexeï Bosak
chercheur à l'installation Européenne de Rayonnement Synchrotron, Grenoble, Directeur de thèse

M Michael Krisch
chercheur à l'installation Européenne de Rayonnement Synchrotron, Grenoble, Co-Directeur de thèse

Abstract

The classical methods in the study of lattice dynamics, such as inelastic neutron and x-ray scattering, are and will remain flux-limited, consequently the measurements are time consuming. To maximise the yield of these techniques, measurement strategies need to be established prior to the experiment. These strategies can be elaborated and optimised by lattice dynamics calculations and thermal diffuse scattering. Measuring thermal diffuse scattering is a simple experiment where extended regions of reciprocal space can be rapidly explored in detail and characteristic features of the lattice dynamics identified. Slower spectroscopy measurements can then be applied on the selected regions of interest to gain access to the energy and intensity of individual vibrations. Moreover, in some cases the input of thermal diffuse scattering may become so constraining for the (quasi)harmonic lattice dynamic calculation, that inelastic scattering experiment will not be a necessary ingredient for the recovery of a self-consistent picture of the dynamics.

In the frame of this work, the combination of thermal diffuse scattering, inelastic x-ray scattering and lattice dynamics calculations from first principles (*ab initio*) is applied to study the lattice dynamics of single crystals. Both diffuse scattering intensities and inelastic spectra determined by experiment are compared to the ones calculated *ab initio*. The combination of these three techniques gives access to the full lattice dynamics in the harmonic description and permits valuable new insights into the vibrational properties.

The reader will be introduced to the key formalism of lattice dynamics, inelastic and thermal diffuse scattering. Methods for the calculation of vibrational properties from first principles are discussed, followed by a guideline for well converged calculations. The experimental techniques used in this work are presented and new possibilities for combined studies examined.

The methodology is illustrated for several benchmark systems. Two silica polymorphs - coesite and α-cristobalite – were chosen as examples for covalent systems and investigated in detail. The experimentally validated calculation was used for the analysis of eigenvectors and eigenvalues of different modes, and their contribution to the total and partial density of vibrational states. Comparison with the most abundant silica polymorph - α-quartz - and germanium oxide in α-quartz structure reveals distinct similarities and differences in the low-energy vibrational properties. Metallic tin polymorphs were chosen to study the influence of the electron subsystem on inter-ionic interactions and the lattice dynamics. Tin

exhibits both interesting structural properties and a complex Fermi surface. An unusual asymmetry of thermal diffuse scattering is observed which can be explained within the frame of harmonic lattice dynamics. Finally, the established method is applied to ice which exhibits not only characteristic thermal diffuse scattering but also static contributions from the hydrogen disorder.

The methodology proposed in the present work provides a powerful tool in the study of lattice dynamics and will be applicable to a large variety of systems. The studies can be extended to extreme conditions involving very high pressures and a large temperature range. It may be also used to study localised properties of atomic vibrations in systems with broken symmetries, e.g. disorder or surface effects.

Résumé (français)

Les méthodes classiques dans l'étude de la dynamique de réseau, comme la diffusion inélastique des neutrons et des rayons X, sont et vont rester limitées en flux. En conséquence les mesures sont coûteuse en temps. Pour optimiser le rendement de ces techniques, la stratégie de mesure doit être préparée avant l'expérience. Cette stratégie peut être élaborée et optimisé par des calculs de la dynamique de réseau et de la diffusion diffuse. La mesure de la diffusion diffuse thermique est une expérience simple où les régions étendues dans l'espace réciproque peuvent être explorées rapidement et en détails, ce qui permet d'identifier les caractéristiques dans la dynamique de réseau. Une méthode spectroscopique peut être appliquée ensuite sur les régions d'intérêt donnant accès à l'énergie et à l'intensité des vibrations individuelles. Dans certains cas, la diffusion diffuse thermique devient tellement contraignante pour les calculs de la dynamique de réseau (quasi)harmonique, que l'expérience de diffusion inélastique n'est plus un ingrédient nécessaire dans la reconstruction d'une image cohérente de la dynamique.

Dans le cadre de ce travail la combinaison des techniques utilisant la diffusion thermique, la diffusion inélastique des rayons X et les calculs réalisés à partir des premiers principes (*ab initio*) est proposée pour l'étude de la dynamique de réseau de monocristaux. Les intensités de diffusion diffuse ainsi que les spectres inélastiques observés sont comparés à ceux calculés *ab initio*. Ces techniques combinées donnent accès à la description complète de la dynamique de réseau en approximation harmonique, et fournissent des informations supplémentaires précieuses.

Le lecteur sera initié au formalisme de la dynamique de réseau et à celui de la diffusion inélastique et thermique. Les méthodes de calculs des propriétés vibrationnelles issues des calculs *ab initio* vont être introduites suivant un ensemble d'étapes menant à la convergence et donc à la validation de l'ensemble des calculs. Les techniques expérimentales utilisées tout au long de cette étude ainsi que les nouvelles possibilités s'ouvrant désormais grâce aux études combinées, serons présentées. La méthodologie sera illustrée par plusieurs systèmes de référence. Dans le cadre des systèmes à liaisons covalentes, deux polymorphes de silice - coésite et cristobalite - sont à l'étude. Les calculs expérimentaux validés sont utilisés pour l'étude des vecteurs propres, des valeurs propres et de leur contributions a la densité d'états vibrationnels (partiel et total). La comparaison avec le polymorphe de silice le plus abondant - α-quartz - et l'oxide de germanium

en structure de α-quartz - révèle des ressemblances et des différences distinctes dans les propriétés vibrationnelles à basse énergie. Les polymorphes d'étain ont été choisis pour étudier l'impact du sous-système électronique sur les interactions inter-ioniques et la dynamique de réseau de monocristaux. L'étain manifeste des propriétés structurelles intéressantes, et une surface de Fermi relativement complexe. On observe une asymétrie inhabituelle au niveau de la diffusion diffuse, propriété qui peut s'expliquer dans le cadre d'une approximation harmonique de la dynamique de réseau. Enfin, la méthode élaborée est appliquée à de la glace, ce qui démontre non seulement une diffusion thermique caractéristique mais également des contributions statiques provenant du désordre de l'hydrogène.

La méthodologie proposée fournit un outil puissant pour l'étude de la dynamique de réseau et sera applicable à une large variété de systèmes. Les études peuvent être étendues à des conditions extrêmes impliquant de très hautes pressions et une large gamme de températures. Cette méthodologie peut également être utilisée pour étudier les propriétés localisées de vibrations atomiques dans les systèmes avec des symétries brisées, par exemple des systèmes avec du désordre ou des effets topologiques.

Phantasie ist wichtiger als Wissen, denn Wissen ist begrenzt.
Albert Einstein

Contents

List of Figures

List of Tables

Acronyms

ESRF	European Synchrotron Radiation Facility
DFPT	density functional perturbation theory
IXS	inelastic x-ray scattering
INS	inelastic neutron scattering
FWHM	full-width-half-maximum
TDS	thermal diffuse scattering
VDOS	density of vibrational states
X-VDOS	generalised x-ray weighted density of vibrational states

Chapter 1

Introduction

1.1 General overview

The scattering of monochromatic X-rays from a perfect and infinite crystal lattice results in discrete reflections. In a real crystal the atoms located on the lattice points fluctuate around their equilibrium positions. These fluctuations result in temperature dependent vibrations but remain finite at zero temperature. In a quantum mechanical picture the vibrations take discrete energies and are described in the frame of lattice dynamics. The traditional way to study so-called phonon excitations experimentally is inelastic neutron or x-ray scattering (Hippert et al., 2006). Employing these methods one can actually measure the phonon energy at a chosen point in reciprocal space and obtain some limited information on amplitude and direction of the vibrations. The phonons, which span typically an energy range of up to a few hundreds meV, also influence the absolute intensity of Bragg reflections and give rise to diffuse scattering in-between the Bragg spots. This so-called thermal diffuse scattering (TDS) contains valuable information on the lattice dynamics, and can be measured with a detector which does not allow for a discrimination of the different phonon energies. Historically, TDS from X-rays was the first technique to be proposed to study phonon dispersion relations (Faxén, 1923, Waller, 1923) and became popular in the study of elastic constants in the 1950s (Wooster, 1962). The currently available high flux and brilliant x-ray beams from synchrotrons in combination with bi-dimensional single photon counting x-ray detectors with good quantum efficiency and low noise led to a revival of TDS studies. By the use of force constant models it is possible to determine the phonon dispersion relations (Holt et al., 1999, 2001, Xu et al., 2008). The accuracy of the extracted phonon dispersion relations is thus model dependent. Nevertheless, TDS is very powerful because the intensity distribution of a large volume in three dimensional reciprocal space can be determined in a very reasonable time. Char-

acteristic scattering intensity distributions can be traced and inelastic scattering measurements can be performed at selected points in reciprocal space.

The classical methods in the study of lattice dynamics such as triple axis inelastic neutron scattering (INS) and inelastic x-ray scattering (IXS) are typically very time demanding, even with the most advanced spectrometers. Time-of-flight neutron scattering is more efficient, as it allows for a measurement of phonon energies in a large volume of reciprocal space. As for triple axis INS the ratio of energy resolution to incoming energy $\Delta E/E$ is only in the order of 10^{-2} whereas IXS spectrometers can be realised with meV resolution and $\Delta E/E$ in the order of 10^{-7}. The resolution in momentum transfer is much better defined in scattering experiments using X-rays, where it is also decoupled from the energy resolution. INS involves a complex resolution function with dependency on both, energy and momentum transfer. The difficulties in focusing neutrons results furthermore in the requirement of large samples.

In this work the combination of IXS, TDS and *ab initio* lattice dynamics calculations is proposed to get access to the full lattice dynamics in single crystals. The measurement of TDS is a simple experiment where extended regions of reciprocal space can be rapidly explored in detail. Characteristic features in the lattice dynamics can be localised and selected for an energy resolved measurement employing IXS. The scattering intensities, which contain informations on the phonon eigenvectors, are calculated *ab initio* and compared to the experiment. With the validated calculation it is then possible to get new insights into the lattice dynamics. Benchmark studies were performed for covalent frameworks (silica polymorphs and ice) and metallic systems (tin polymorphs).

The work is structured as follows. Chapter 1 provides a general overview and the motivation for the investigated systems. The theoretical background and the key formulas for computing the scattering intensities are presented in Chapter 2. Chapter 3 provides an introduction to *ab initio* lattice dynamics calculations. The experimental set-ups and the implementation of an instrument for the combined study of TDS and IXS is discussed in Chapter 4. Details of the data analysis can be found in Chapter 5. Results obtained on the benchmark systems are presented and discussed in Chapter 6. Chapter 7 summarises the findings, discusses the impact of the actual study, and provides an outlook for future applications.

1.2 Lattice dynamics in silica polymorphs

At very low energies, the atomic vibrations in crystals are described by sound waves, discussed within the long wavelength limit in Section 2.5. In this energy region the density of vibrational states (VDOS), $g(E)$, follows the Debye model $g(E) \sim E^2$, which is valid for an elastic continuum. The VDOS exhibits an excess

over the Debye level, as the wave vector approaches the zone boundary of the Brillouin zone. This is due to the fact that the initially linear dispersion becomes flat, which results in so-called Van Hove singularities (Van Hove, 1953).

The VDOS of glasses also exhibits an excess of states over the Debye law, the so-called 'Boson peak'. The temperature dependence of the magnitude of this peak obeys the Bose statistics, which explains the origin of its name. The Boson peak appears at an energy of a few meV, where the VDOS of the corresponding crystal usually does not show any distinct feature. The difference in energy between the Boson peak and the Van Hove singularities in the corresponding crystals was considered to be large enough to attribute the origin to different physical phenomena. In fact, the origin of the Boson peak in glasses was thought to originate from disorder and generally accepted to be a glass specific feature. In most of the models proposed so far the appearance of the Boson peak is attributed for example to instabilities of vibrational modes due to saddle points in the energy landscape (Grigera et al., 2003), locally favoured structures (Tanaka, 2001), vibrations of clusters (Duval et al., 1990), librations (Buchenau et al., 1984), coherent motions (Angell, 1995) of molecular fragments, or the breakdown of the continuum approximation (Monaco and Giordano, 2009), to name a few of them.

Only a few works consider the Boson peak and the van Hove singularities as related phenomena (Schirmacher et al., 1998, Taraskin et al., 2001). Recently it was shown for a sodium silicate glass (Chumakov et al., 2011) that the Boson peak in the glass appears at the same energy as the Van Hove singularities in the corresponding crystal if the densities are matched. The phenomenon was thus suggested to originate not from disorder but from the difference in density and sound velocities of the glassy and crystalline counterparts.

In a very recent work (Chumakov et al., 2013) we could show for various glassy and crystalline SiO_2 polymorphs that the excess states over the Debye law in the VDOS in absolute numbers are very similar for glasses and crystals with matched densities. The excess states in the systems with matched densities are found to be located at the same energies and to provide the same heat capacity. The appearance of the Boson peak in glasses at lower energies than the Van Hove singularities in crystals as well as the difference in heat capacity is thus not due to disorder but because the density of a glass is typically lower than the density of the corresponding crystal.

In the frame of this work one step further is undertaken, namely the clarification of the reciprocal space positions and the nature of the associated vibrations. The combination of thermal diffuse scattering (TDS), inelastic x-ray scattering (IXS) and lattice dynamics calculations from first principles is used for the study of lattice dynamics at arbitrary momentum transfers. The lattice dynamics of the silica polymorphs coesite and α-cristobalite are investigated in detail and compared

with the most abundant silica polymorph α-quartz and α-GeO_2.

The knowledge of the full lattice dynamics allows the localisation of critical points, which actually lead to the occurrence of Van Hove singularities, in 3D reciprocal space and the attribution of its vibrational character and the topology in energy-momentum space. The low energy region of the lattice dynamics gives valuable insight for understanding the compression mechanism and phase transitions. Coesite in particular has furthermore an interesting geological relevance, see Chapter 6.

1.3 Lattice dynamics in metallic tin

The lattice dynamics in metals is influenced by the conducting electrons. The Fermi surface, which defines the surface in electron momentum space that separates occupied from unoccupied states, is one of the key concept for the physics in metals. The shape of the Fermi surface is decisive for their electric, magnetic and thermal properties. In the context of lattice dynamics the almost free electrons at the Fermi surface play a crucial role; they can couple to the phonons resulting in abrupt variations in the phonon dispersion relations (Kohn, 1959), so-called Kohn anomalies. The electron phonon coupling is responsible for the Cooper-pair formation in conventional super conductors and an important concept in the theory of spin and charge density waves. Changes in the Fermi-surface topology lead to anomalies in thermodynamic and elastic properties and leave their fingerprint in the lattice dynamics.

The Fermi surface of metals consists in general of surfaces from different bands. If a piece of a given Fermi surface is superposed to another piece by a translational vector in reciprocal space, the Fermi surface is said to be nested by this vector. For a reasonable simple Fermi surface some anomalies in the phonon dispersion relations can be assigned to specific nesting vectors. This was for example possible in the case of vanadium (Bosak et al., 2008). When all the Fermi surfaces are combined together, the resulting patterns can be decomposed into nested Fermi surfaces if the avoided crossings of these surfaces are neglected (Whangbo et al., 1991). Some anomalies in the phonon dispersion relations can be assigned to such hidden Fermi surface nesting.

Pronounced anomalies in the phonon dispersion relations lead to characteristic variations in the TDS intensities. A tracing of the intensity variations in three dimensional reciprocal space can eventually be used to map out the shape of Fermi surface sections (Bosak et al., 2009b).

In the frame of this work the metallic polymorphs of tin, which show interesting structural properties on one hand and a complex Fermi surface on the other hand, are investigated. Tin shows in fact a marked crystal anisotropy and crystallises to a

non-centrosymmetric environment of atoms at room temperature (β-tin). Alloying tin with indium results in substitutionally disordered crystals with a primitive hexagonal lattice containing one atom per unit cell, called γ-tin. It is a convenient model system in the study of lattice dynamics and electron-phonon interactions, because its phonon dispersion relations consists only of acoustic branches and it is stable at ambient conditions. The strong influence of the electron sub-system on inter-ionic interactions and its influence on the lattice dynamics are subject of a detailed study in this work. The combination of TDS, IXS and lattice dynamics calculations from first principles is again proposed as an effective strategy to study atypical features in the lattice dynamics.

1.4 Lattice dynamics in ice

Water exhibits a very simple structure at molecular level. However, the hydrogen-bonded network of water molecules within its crystalline structure results in a complex phase diagram with at least 16 and at least 2 amorphous forms of ice showing interesting physical and chemical properties (Bartels-Rausch et al., 2012, Petrenko and Whitworth, 1991). More than 60% of the fresh water on the Earth is kept in the form of ice. Ice Ih is the only ice existing in the crust, while the metastable ice Ic is suspected to form in the atmosphere (Kuhs et al., 2012, Murray et al., 2005) It has been proposed that snow crystals may start growing at low temperatures from a cubic symmetry with stacking disorder before transforming to the hexagonal structure (Kobayashi and Kuroda, 1987, Kuhs et al., 2012). Stacking faults are indeed frequent also in ice Ih and contribute to diffuse scattering (Oguro and Hondoh, 1988). In the ice-Ih phase the oxygen atoms are arranged in a wurzite structure, and the hydrogen atoms are placed randomly according Pauling's ice rules (Pauling, 1935). The hydrogen disorder, however, affects the positions of oxygen atoms, resulting in a deviation of their crystallographic position by up to several hundreds of an Ångstom (Kuhs and Lehmann, 1986).

The dynamical properties of ice have been subject of many studies and interesting features were observed. The investigation by x-ray scattering of amorphous ice, for example, revealed a narrow width of phonon excitations in amorphous ice in contrast to the broad features usually observed in amorphous systems and the absence of a dominant excess of low-energy modes (Koza et al., 2004, Schober et al., 2000). Ultrasonic measurements reveal negative Grüneisen and Bridgman parameters, indicating phase transitions due to elastic instabilities (Gromnitskaya et al., 2001). Anomalous features in the lattice dynamics are responsible for the negative thermal expansion at low temperatures and the softening of transverse acoustic modes an important concept in pressure induced amorphisation (Strässle et al., 2004).

Structure and dynamical properties of the most usual polymorph ice Ih have been also the focus of many theoretical studies. The disorder of both hydrogen and oxygen atoms makes the problem theoretically challenging. *Ab initio* lattice dynamics calculations have been carried out for different phases, phonon dispersion relations and densities of vibrational states are reported (Adeagbo et al., 2005, Cote et al., 2003). A pressure dependent study of ice XI, the ordered version of ice Ih, using density functional perturbation theory (DFPT) was carried out by Umemoto et al. (2004). The authors find that pressure induces a mechanical instability, which is initiated by the softening of an acoustic phonon occurring at an incommensurate wavelength, followed by the collapse of the entire acoustic band and by the violation of the Born stability criteria (these criteria require all principal minor of the elastic tensor to be positively defined). Phonon dispersion relations, measured by INS, are exclusively documented for D_2O (Bennington et al., 1999, Fukazawa et al., 2003, Renker, 1969). The only detailed study of x-ray diffuse scattering on H_2O ice is dated back to 1949 (Owston, 1949), where the technique was quite limited.

In this work we investigate single crystals of ice-Ih, extracted from the subglacial Vostok lake accretion ice layer by means of diffuse and inelastic x-ray scattering. *Ab initio* calculations and Monte-Carlo modelling are used to rationalise the experimental results.

Introduction

1.5 Aperçu général (français)

La diffusion des rayons X monochromatiques d'un cristal parfait et infini produit des réflexions discrètes. Dans un vrai cristal les atomes situés sur les nœuds du réseau vibrent autour de leurs positions d'équilibre. Ces fluctuations entraînent des vibrations collectives des atomes dépendant de la température et toujours présentes au zéro absolu. Selon la mécanique quantique, ces vibrations se caractérisent par des énergies discrètes et sont décrites dans le cadre de la dynamique de réseau. La manière traditionnelle expérimentale d'étudier les excitations de phonons est la diffusion inélastique des neutrons et des rayons X (Hippert et al., 2006). Ces méthodes donnent accès à l'énergie des phonons à un point choisi dans l'espace réciproque. Elles contiennent également des informations limitées sur l'amplitude et la direction des vibrations. Les phonons réduisent l'intensité absolue des réflexions de Bragg et donnent lieu à une diffusion diffuse entre les spots de Bragg. Cette diffusion diffuse thermique (TDS) contient des informations précieuses sur la dynamique de réseau, même si celle-ci est mesurée à partir d'un détecteur qui ne permet pas une discrimination des énergies de phonons. Les phonons couvrent typiquement une gamme d'énergie allant jusqu'à quelques centaines de meV. La TDS de rayons X a été proposée comme première technique dans l'étude de dispersion des phonons (Faxén, 1923, Waller, 1923) devenant populaire pour l'étude des constantes élastiques dans les années 1950 (Wooster, 1962). Le flux élevé et la brillance actuellement disponible du rayonnnement synchrotron en combinaison avec des détecteurs bidimensionnels qui présentent une bonne efficacité quantique et un faible bruit du fond, ont mené à la renaissance des études TDS. En utilisant un modèle de constantes de force, il est possible d'exploiter la dispersion des phonons (Holt et al., 1999, 2001, Xu et al., 2008). La précision de la dispersion des phonons extrait du TDS est donc dépendante du modèle. Néanmoins, la TDS est une technique très puissante car la cartographie de la distribution des intensités permet une exploration rapide et détaillée des régions étendues dans l'espace réciproque. Cela permet d'identifier les caractéristiques de la dynamique de réseau. Une méthode spectroscopique comme la diffusion

inélastique peut être appliquée ensuite sur les régions d'intérêt. Elle offre l'accès à l'énergie et l'intensité des vibrations individuelles.

La spectrométrie à neutrons triple axe et la diffusion inélastique des rayons X (IXS) sont généralement très coûteuses en temps, même avec les spectromètres les plus avancés. La spectrométrie de neutrons à temps de vol est plus efficace, car elle permet une mesure des énergies des phonons en régions étendues dans l'espace réciproque. Cependant, comme pour la spectrométrie à neutrons triple axe, le ratio de la résolution en énergie a l'énergie incidente $\Delta E/E$ est seulement de l'ordre de 10^{-2}, alors que les spectromètres IXS peuvent réaliser des études avec des résolutions proche du meV et $\Delta E/E$ de l'ordre de 10^{-8}. La résolution du moment de diffusion est beaucoup mieux définie dans des expériences utilisant des rayons X où elle est découplée de la résolution en énergie. La diffusion inélastique de neutrons (INS) implique une résolution complexe. Celle-ci dépend à la fois du transfert d'énergie et du vecteur de diffusion. Les difficultés à focaliser les neutrons nécessitent de grands échantillons. Dans ce travail, la combinaison de IXS, TDS et des calculs *ab initio* est proposée afin d'accéder à la dynamique de réseau de monocristaux. La mesure de la TDS est une expérience simple où les régions étendues de l'espace réciproque peuvent être explorées. Les caractéristiques de la dynamique de réseau peuvent être localisées et sélectionnées pour la mesure IXS. Les intensités de diffusion, qui contiennent des informations sur les vecteurs propres de phonons, sont calculés *ab initio* et comparées à l'expérience. Avec le calcul validé, il est ensuite possible d'accéder à des nouvelles connaissances sur la dynamique de réseau. Des études de référence ont été effectuées pour des systèmes à liaisons covalentes (polymorphes de silice et glace) et des systèmes métalliques (polymorphes d'étain).

Le travail est structuré comme suit : Le Chapitre 1 présente un aperçu général et ce qui motive l'étude des systèmes choisis (en anglais). La description théorique et les formules clés pour calculer les intensités de diffusion sont présentées au Chapitre 2. Le Chapitre 3 propose une introduction aux calculs *ab initio* de la dynamique de réseau. Le dispositif expérimental et la mise en œuvre d'un instrument pour l'étude combinée de TDS et IXS est élaboré au Chapitre 4. Les détails de l'analyse des données peuvent être trouvées dans le Chapitre 5. Les résultats obtenus sur les systèmes de référence sont présentés et discutés dans le Chapitre 6. Enfin, le Chapitre 7 est dédié aux conclusions, à l'impact de ce travail et aux perspectives pour des futures applications.

Chapter 2

Theoretical basis

The following review provides the key formulae for computing the scattering intensities and analysing experimental results. The standard formalism of lattice dynamics is briefly introduced in Section 2.1, followed by the formalism of TDS and IXS (Section 2.2). Higher order contributions to the scattering intensities are discussed in Section 2.3. Some background on the quantitative analysis of experimental results is given in Section 2.4 and 2.5.

2.1 Equation of motion and dynamical matrix

The key information of lattice dynamics is contained in the dynamical matrix (see for example Maradudin et al. (1971), Willis and Pryor (1975), Xu et al. (2009) for a detailed description). We shall see that it contains both the frequencies and displacements associated with all possible lattice vibrations in a crystal. Here we follow the formalism of Xu et al. (2009).

Consider a crystal with N unit cells containing n atoms, labelled s. The crystal is initially in mechanical equilibrium, and the positions of the s-th atom in the l-th unit cell are given by $\boldsymbol{r}_{l,s} = \boldsymbol{R}_l + \boldsymbol{\tau}_s$, where $\boldsymbol{R}_l$ is the lattice vector and $\boldsymbol{\tau}_s$ the atomic basis vector within a unit cell. Allowing the atoms to move around their equilibrium positions with a displacement $\boldsymbol{u}_{l,s}$ the position vector becomes $\boldsymbol{r}_{l,s} = \boldsymbol{R}_l + \boldsymbol{\tau}_s + \boldsymbol{u}_{l,s}$. In order to derive the equation of motion for the vibrations we write the total energy as a Taylor expansion about structural equilibrium coordinates, which is the basis of harmonic lattice dynamics,

$$E = E_0 + \sum_{l,s} \frac{\partial E}{\partial \boldsymbol{u}_{l,s}} \boldsymbol{u}_{l,s} + \frac{1}{2} \sum_{l,s,l',s'} \boldsymbol{u}_{l,s} \Phi^{\alpha,\alpha'}_{l,s,l',s''} \boldsymbol{u}_{l',s'} + ... \tag{2.1}$$

The sum runs over all atoms and unit cells, including thus all atoms in the crystal.

$\Phi^{\alpha,\alpha'}_{l,s,l',s''}$ is the matrix of the force constants

$$\Phi^{\alpha,\alpha'}_{l,s,l',s'} = \frac{\partial^2 E}{\partial \boldsymbol{u}^{\alpha}_{l,s} \partial \boldsymbol{u}^{\alpha'}_{l's'}}, \tag{2.2}$$

and $\alpha = 1, 2, 3$ denotes the Cartesian x,y,z.

At equilibrium the forces $F_{l,s,\alpha} = -\frac{\partial E}{\partial \boldsymbol{u}_{l,s}}$ are all zero and the first-order term vanishes. The invariance of the potential energy against rigid body translations requires

$$\sum_{l',s'} \Phi^{\alpha,\alpha'}_{l,s,l',s'} = 0. \tag{2.3}$$

In the Harmonic Approximation the 3^{rd} and higher order terms are neglected. One can now write down the equation of motion for each atom

$$m_s \ddot{\boldsymbol{u}}_{l,s} = \sum_{l',s'} \Phi_{l,s,l',s'} \boldsymbol{u}_{l's'}, \tag{2.4}$$

where m_s denotes the atomic mass. Assuming Born-von-Kármán periodic boundary conditions (Willis and Pryor, 1975) the solution for $\boldsymbol{u}_{l,s}$ will be a linear superposition of traveling harmonic waves with wave vector $\boldsymbol{k}$ and mode $j = 1, 2, ..., 3n$. Substituting a plane-wave guess for the solution, one obtains

$$\boldsymbol{u}_{l,s} = \sum_{\boldsymbol{k},j} Re\left(\frac{1}{\sqrt{m_s}} a_{\boldsymbol{k},j} \boldsymbol{e}_{\boldsymbol{k},j} e^{(i\boldsymbol{k}(\boldsymbol{R}_l) + i\omega_{\boldsymbol{k},j} t)} \right), \tag{2.5}$$

with phonon wavevector $\boldsymbol{k}$, defined in the first Brillouin zone, vibration amplitude $a_{\boldsymbol{k},j}$, polarisation vector $\boldsymbol{e}_{\boldsymbol{k},j,s}$ and vibrational frequency $\omega_{\boldsymbol{k},j}$. This yields an eigenvalue equation

$$C(\boldsymbol{k}) \varepsilon_{\boldsymbol{k},j} = \omega^2_{\boldsymbol{k},j} \varepsilon_{\boldsymbol{k},j}. \tag{2.6}$$

The dynamical matrix is the mass-reduced Fourier transform of the force constant matrix

$$C^{\alpha,\alpha'}_{s,s'}(\boldsymbol{k}) = -\frac{1}{\sqrt{m_s m_{s'}}} \sum_{l'} \Phi^{\alpha,\alpha'}_{l,s,l',s'} e^{(i\boldsymbol{k}\boldsymbol{R}_{l,l'})}, \tag{2.7}$$

which is Hermitian by construction. Because of translational invariance one can set $\boldsymbol{R}_l = 0$ for simplicity. The eigenvectors

$$\boldsymbol{\varepsilon}_{\boldsymbol{k},j} = \begin{pmatrix} \boldsymbol{e}_{\boldsymbol{k},j,s_1} \\ \boldsymbol{e}_{\boldsymbol{k},j,s_2} \\ \vdots \\ \boldsymbol{e}_{\boldsymbol{k},j,s_n} \end{pmatrix}$$

are periodic in reciprocal space and satisfy the orthonormal relationship

$$\boldsymbol{\varepsilon}_{\boldsymbol{k},j} \cdot \boldsymbol{\varepsilon}^*_{\boldsymbol{k'},j'} = \sum_s \boldsymbol{\varepsilon}_{\boldsymbol{k},j,s} \cdot \boldsymbol{\varepsilon}^*_{\boldsymbol{k'},j',s} = \delta_{\boldsymbol{k},\boldsymbol{k'}}\delta_{\boldsymbol{j},\boldsymbol{j'}}. \tag{2.8}$$

The vibrational frequencies of each vibrational mode are obtained as the square roots of the eigenvalues, and the eigenvectors give the pattern of atomic displacements belonging to each vibrational mode. The dynamical matrix contains thus the complete information of the lattice dynamics. The above expressions are derived in C-matrix notation but there exists also a common non-periodic D-matrix notation. The distinction is important as different codes for lattice dynamics calculation output the results in different notations. Consider the following alternative definition for the solution of Equation 2.4:

$$\boldsymbol{u}_{l,s} = \sum_{\boldsymbol{k},j} Re(\frac{1}{\sqrt{m_s}} a_{\boldsymbol{k},j} \boldsymbol{e}_{\boldsymbol{k},j} e^{(i\boldsymbol{k}(\boldsymbol{R}_l+\boldsymbol{\tau}_s)+i\omega_{\boldsymbol{k},j}t)}), \tag{2.9}$$

which explicitly includes the atomic basis vector $\boldsymbol{\tau}_s$ in the lattice Fourier transformation. The resulting dynamical matrix is given by

$$D^{\alpha,\alpha'}_{s,s'}(\boldsymbol{k}) = -\frac{1}{\sqrt{m_s m_{s'}}} \Phi^{\alpha,\alpha'}_{l,s,l',s'} e^{(i\boldsymbol{k}\boldsymbol{R}_{l,l'}+\boldsymbol{\tau}_s)}, \tag{2.10}$$

which has the same eigenvalue Equation 2.6 as the dynamical matrix (Expression 2.7) in C-matrix notation. The resulting eigenvectors $\boldsymbol{e}^D_{\boldsymbol{k},j,s}$ differ from the ones based on the C-matrix notation by a phase factor

$$\boldsymbol{e}^D_{\boldsymbol{k},j,s} = \boldsymbol{e}_{\boldsymbol{k},j,s} e^{-i\boldsymbol{k}\boldsymbol{\tau}_s}. \tag{2.11}$$

The scattering intensities for IXS and TDS will be developed using the periodic C-matrix notation. For a description using the D-matrix notation please refer to Xu and Chiang (2005).

2.2 Scattering intensities from phonons

In the following the formulae for IXS and TDS intensities are derived in the adiabatic approximation. The considerations are limited to the case in which the electronic part of the total wave function is not changed by the scattering process. A detailed discussion on the applied approximation can be found elsewhere (Schülke, 2005). The intensity distribution of a linearly polarised x-ray beam scattered by a single electron, I_e, is given by the Thomson scattering formula (Warren, 1966),

$$I_e = I_i \frac{e^4}{m_e^2 c^4 d^2} (sin^2\phi + cos^2\phi cos^2(2\theta)), \tag{2.12}$$

where I_i is the incident intensity, 2θ the scattering angle, ϕ the angle between the scattering plane and the plane defined by the polarisation and the direction of the incident beam, and d is the distance between the scattering center and the detector. The intensity of X-rays scattered by a crystal at scattering vector $\boldsymbol{Q}$ and energy transfer $\Delta\hbar\omega$ arises from the sum of the scattering from all electrons in the system,

$$I(\boldsymbol{Q}, \Delta\hbar\omega) = I_e\langle| \sum_{l,s} f_s e^{i\boldsymbol{Q}(\boldsymbol{R}_l+\boldsymbol{\tau}_s+\boldsymbol{u}_{l,s})}|\rangle\delta(\hbar\omega - \Delta\hbar\omega), \tag{2.13}$$

where f_s is the atomic scattering factor and $\langle \ldots \rangle$ denotes averaging over time. The formula can be simplified using an identity for harmonic lattices (Ott, 1935)

$$\langle e^{i\boldsymbol{Q}\boldsymbol{u}} \rangle = e^{-\frac{1}{2}\langle(\boldsymbol{Q}\boldsymbol{u})^2\rangle}, \tag{2.14}$$

yielding

$$I(\boldsymbol{Q}, \Delta\hbar\omega) = I_e \sum_{l,l',s,s'} f_s f_{s'} e^{-i\boldsymbol{Q}(\boldsymbol{R}_l,l'+\boldsymbol{\tau}_{s,s'})} e^{-\frac{1}{2}\langle(\boldsymbol{Q}(\boldsymbol{u}_{l,s}-\boldsymbol{u}_{l',s'}))^2\rangle}\delta(\hbar\omega - \Delta\hbar\omega). \tag{2.15}$$

Assuming an independent random phase for each mode and exploiting translational symmetry ($\sum_{l,l'} = N\sum_l$), the time average in Equation 2.15 can be evaluated to

$$\frac{1}{2}\langle(\boldsymbol{Q}(\boldsymbol{u}_{l,s} - \boldsymbol{u}_{l',s'}))^2\rangle = M_s + M_{s'} - \sum_{\boldsymbol{k},j} \frac{|a_{\boldsymbol{k},j}|^2}{2\sqrt{m_s m_{s'}}}(\boldsymbol{Q}\boldsymbol{e}_{\boldsymbol{k},j,s})^*(\boldsymbol{Q}\boldsymbol{e}_{\boldsymbol{k},j,s'})e^{i\boldsymbol{k}\boldsymbol{R}_l}, \tag{2.16}$$

where M_s denotes the Debye-Waller factor

$$M_s = \frac{1}{4m_s}\sum_{\boldsymbol{k},j} |a_{\boldsymbol{k},j}|^2 |\boldsymbol{Q}\boldsymbol{e}_{\boldsymbol{k},j,s}|^2. \tag{2.17}$$

The amplitude of each vibrational mode satisfies the Bose-Einstein relation of the corresponding phonons,

$$|a_{\boldsymbol{k},j}|^2 = \frac{2\hbar}{N\omega_{\boldsymbol{k},j}}\left(\frac{1}{e^{\hbar\omega_{\boldsymbol{k},j}/k_BT}-1} + \frac{1}{2}\right) = \frac{\hbar}{N\omega_{\boldsymbol{k},j}} coth\left(\frac{\hbar\omega_{\boldsymbol{k},j}}{2k_BT}\right), \tag{2.18}$$

with Boltzmann constant k_B and temperature T.

The general formula for scattering from phonons thus reads

$$I(\boldsymbol{Q},\Delta\hbar\omega) = NI_e \sum_{l,s,s'} f_s f_{s'} e^{-M_s - M_{s'}} e^{-i\boldsymbol{Q}(\boldsymbol{R}_l+\boldsymbol{\tau}_{s,s'})} e^{G^{s,s'}_{l,\boldsymbol{Q}}} \delta(\hbar\omega - \Delta\hbar\omega) \tag{2.19}$$

with

$$G^{s,s'}_{l,\boldsymbol{Q}} = \frac{\hbar}{2N\sqrt{m_s m_{s'}}} \sum_{\boldsymbol{k},j} \frac{1}{\omega_{\boldsymbol{k},j}} coth(\frac{\hbar\omega_{\boldsymbol{k},j}}{2k_BT})(\boldsymbol{Q}\boldsymbol{e}_{\boldsymbol{k},j,s})^*(\boldsymbol{Q}\boldsymbol{e}_{\boldsymbol{k},j,s'})e^{i\boldsymbol{k}\boldsymbol{R}_l}, \tag{2.20}$$

where the double summation $\sum_{l,l'}$ has been replaced by $N\sum_l$ exploiting translational invariance. The intensity of scattered X-rays is determined by the eigenfrequencies $\omega_{\boldsymbol{k},j}$ and eigenvectors $\boldsymbol{e}_{\boldsymbol{k},j}$ of the dynamical matrix (Equation 2.7). The evaluation of the general formula 2.19 and 2.20 is numerically demanding because of the two nested three dimensional sums (one in real and one in reciprocal space). A standard approach for simplifying the expressions is a Taylor expansion

$$I = I_0 + I_1 + I_2 + \dots. \tag{2.21}$$

For a large crystal we can assume $N \to \infty$, and

$$\sum_l e^{i\boldsymbol{k}\boldsymbol{R}_l} = N\sum_l \delta(\boldsymbol{k} - \boldsymbol{K}_p), \tag{2.22}$$

where $\boldsymbol{K}_p$ is a reciprocal vector. The assumptions are not applicable for clusters or nanocrystals but valid for standard single crystal studies. The series expands to

$$I_0(\boldsymbol{Q}) = N^2 I_e \sum_{s,s'} f_s f_{s'} e^{-M_s - M_{s'}} e^{-i\boldsymbol{Q}\boldsymbol{\tau}_{s,s'}} \sum_l \delta(\boldsymbol{Q} - \boldsymbol{K}_p), \tag{2.23}$$

$$\begin{aligned} I_1(\boldsymbol{Q},\hbar\omega) &= \frac{\hbar N I_e}{2}\sum_j \frac{1}{\omega_{\boldsymbol{Q},j}} coth\Big(\frac{\hbar\omega_{\boldsymbol{Q},j}}{2k_BT}\Big) \times \\ &\quad |\sum_s \frac{f_s}{\sqrt{m_s}} e^{-M_s}(\boldsymbol{Q}\boldsymbol{e}_{\boldsymbol{Q},j,s}) e^{-i\boldsymbol{Q}\boldsymbol{\tau}_s}|^2 \delta(\hbar\omega - \Delta\hbar\omega), \end{aligned} \tag{2.24}$$

and

$$\begin{aligned} I_2(\boldsymbol{Q},\hbar\omega) &= \frac{\hbar^2 N v I_e}{8}\int \frac{d^3\boldsymbol{k}}{(2\pi)^3}\sum_{j,j'} W_{\boldsymbol{k},j} W_{\boldsymbol{Q}-\boldsymbol{k},j'} \times \\ &\quad \Big|\sum_s \frac{f_s}{m_s} e^{-M_s} e^{-i\boldsymbol{Q}\boldsymbol{\tau}_s} (\boldsymbol{Q}\boldsymbol{e}_{\boldsymbol{k},j,s})(\boldsymbol{Q}\boldsymbol{e}_{\boldsymbol{Q}-\boldsymbol{k},j,s})\Big|^2 \delta(\hbar\omega - \Delta\hbar\omega), \end{aligned} \tag{2.25}$$

where v is the volume of the real space unit cell and $W_{\boldsymbol{k},j}$ is given by

$$W_{\boldsymbol{k},j} = \frac{1}{\omega_{\boldsymbol{k},j}} coth\Big(\frac{\hbar\omega_{\boldsymbol{k},j}}{2k_BT}\Big). \tag{2.26}$$

The integral in Equation 2.25 is over the first Brillouin zone. The zeroth-order term (Equation 2.23) corresponds to Bragg diffraction at $\boldsymbol{Q} = \boldsymbol{K}_l$. The intensity of the Bragg peaks is reduced by the temperature dependent Debye-Waller factor (Equation 2.17) and diffusively distributed in reciprocal space. The first order term

(Equation 2.24) corresponds to single phonon scattering and gives the scattering intensity of IXS. Each first order scattering event at a given scattering vector $\boldsymbol{Q}$ involves one phonon of any of the $3n$ branches at the same wave vector because of momentum conservation. The phonon involved in the scattering process can be either emitted or absorbed and the involved energy transfer $\Delta\hbar\omega$ corresponds to the phonon energy. TDS is the sum of the scattering of all branches. It reduces the energy and momentum transfer resolved intensity $I(\boldsymbol{Q}, \hbar\omega)$ to a momentum transfer resolved intensity $I(\boldsymbol{Q})$ which is generally non-zero for any scattering vector. In first order it is given by

$$I_1(\boldsymbol{Q}) = \frac{\hbar N I_e}{2} \sum_j \frac{1}{\omega_{\boldsymbol{Q},j}} coth\Big(\frac{\hbar\omega_{\boldsymbol{Q},j}}{2k_B T}\Big) | \sum_s \frac{f_s}{\sqrt{m_s}} e^{-M_s} (\boldsymbol{Q}\boldsymbol{e}_{\boldsymbol{Q},j,s}) e^{-i\boldsymbol{Q}\boldsymbol{\tau}_s}|^2. \quad (2.27)$$

I_1 is strongly influenced by the thermal population factor contained in the *coth* function. The low energy phonons - in particular the acoustic phonons close to Bragg reflections - contribute most.

2.3 Higher order contribution

The second and higher order terms correspond to multiphonon scattering processes and involve all phonons; the momentum transfer can be shared in an infinite number of ways. The second order contribution involves the integration over the first Brillouin zone (see Equation 2.25). It scales with q^2 and increases linearly with T for $\gg T_{Db}$, where T_{Db} denotes the Debye temperature. Xu et al. (2009) computed the total and higher order (zeroth and first order contribution subtracted) intensities for Cu and Si at different temperatures for an arbitrarily chosen direction, see Fig. 2.1. Aiming for a 3% accuracy the example shows that one should limit Q to $\approx 4\pi/a$ at room temperature or $\approx 6\pi/a$ at 100 K; here a is the lattice parameter. The temperature enters through $\hbar\omega/k_B T$, the higher order processes are thus less pronounced for systems with a high Debye temperature. Characteristic features of TDS are contained in the first order contribution, the higher order contributions are smoother with increasing order. In the following we limit our considerations to the first order contribution.

2.4 Reconstruction of lattice dynamics from thermal diffuse scattering

Experimental information on the phonon dispersion relations is traditionally obtained from INS (Brockhouse et al., 1961) and IXS (Burkel, 2000). The information on the phonon eigenvectors can be extracted from inelastic intensities (Strauch

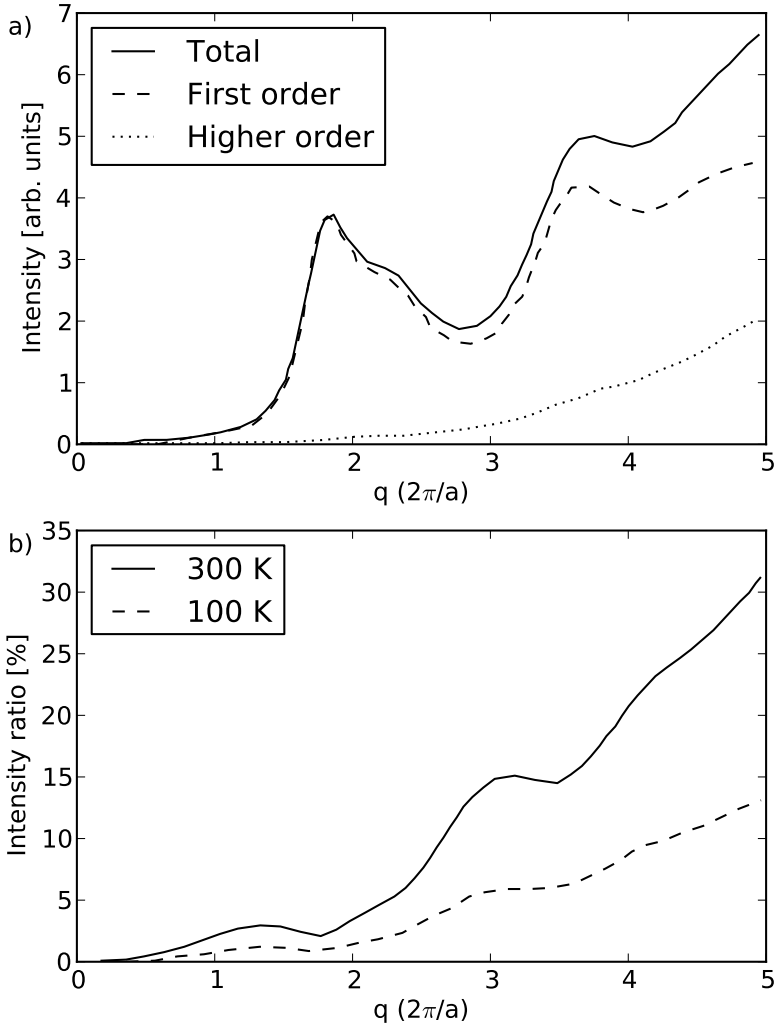

Figure 2.1: a) Calculated total, first order and higher order TDS intensities of Cu at 300 K for Q along [1.00 0.20 0.02]. b) Ratio of high-order TDS to total TDS intensities at the indicated temperatures for Cu along the same direction.

and Dorner, 1986), but such experiments are rarely undertaken. For a quantitative analysis of the dynamical matrix from inelastic scattering one usually introduces a model of interatomic interactions which reproduces the missing eigenvectors. The extraction of phonon dispersion relations from first order TDS intensities is typically performed assuming a model of interatomic potentials; see for instance (Holt et al., 2002, Xu et al., 2008, Xu and Chiang, 2005). The accuracy of the extracted phonon dispersion relations is thus model dependent. Alternatively, one may compute the scattering intensities from an *ab initio* calculated dynamical matrix and compare them with experiment. In this way one may get the description of the full lattice dynamics from single crystal (Bosak et al., 2012) or powder studies (Bosak et al., 2009a). A model-free reconstruction of the dynamical matrix from first order TDS intensities is possible for mono-atomic crystals (Bosak and Chernyshov, 2008). For more complex structures part of the information is irreversibly lost in the kinematic regime. The missing information may in principle be recovered from dynamic scattering (Bosak and Chernyshov, 2008) but the approach is neither easy nor very practical.

In the frame of this thesis I will concentrate on comparing TDS and IXS intensities to values calculated from *ab initio* determined dynamical matrices.

2.5 Derivation of elastic constants

Some quantities can be directly reconstructed from TDS intensities. At reciprocal space positions close to Bragg peaks the long wave length limit is reached involving two assumptions: (i) The TDS intensity is dominated by acoustic modes. The thermal factor (Equation 2.18) becomes most important in the TDS intensity (Equation 2.27) as $\omega \to 0$. Expression 2.18 reduces for $k_B T \gg \hbar\omega$ to $1/N\hbar\omega^2$. For $q \to 0$ the acoustic modes will contribute most as their frequencies approach zero. (ii) The displacements of all atoms in the unit cell are the same due to the acoustic-like vibrations. This assumption holds for a negligible influence of the optic modes on the eigenvectors. The acoustic modes become elastic waves whose wavelength compares to the size of many unit cells. The absolute displacement becomes the same for all atoms in one cell and this displacement is either parallel (longitudinal mode) or perpendicular (transverse mode) to the reduced momentum transfer for high symmetry directions. Under condition (i) and (ii) one finds

$$\boldsymbol{e}_{\boldsymbol{q},j,s} = \boldsymbol{e}_{\boldsymbol{q},j}, j = 1 \ldots 3 \tag{2.28}$$

and Equation 2.27 can be reformulated as follows,

$$I(\boldsymbol{Q}) = \frac{\hbar N I_e}{2} \sum_{j=1}^{3} \frac{1}{\omega_{\boldsymbol{Q},j}} coth\Big(\frac{\hbar\omega_{\boldsymbol{Q},j}}{2k_B T}\Big) |\boldsymbol{Q}\boldsymbol{e}_{\boldsymbol{Q},j}|^2 | \sum_s \frac{f_s}{\sqrt{m_s}} e^{-M_s}|^2. \tag{2.29}$$

Assuming a linear dispersion relation $\omega = qv_a$, where $q = |\boldsymbol{q}|$ and v_a is the sound velocity, one finds

$$I(\boldsymbol{Q}) = \frac{\hbar N I_e}{2} \sum_{j=1}^{3} \frac{1}{q v_{a,j}} coth\Big(\frac{\hbar q v_{a,j}}{2k_B T}\Big) |\boldsymbol{Q}\boldsymbol{e}_{\boldsymbol{Q},j}|^2 | \sum_s \frac{f_s}{\sqrt{m_s}} e^{-M_s}|^2, \tag{2.30}$$

which can be further simplified for $k_B T \gg \hbar\omega$ to $1/N\hbar\omega^2$ to,

$$I(\boldsymbol{Q}) = \frac{\hbar N I_e}{2} \sum_{j=1}^{3} \frac{1}{q^2 v_{a,j}^2} |\boldsymbol{Q}\boldsymbol{e}_{\boldsymbol{Q},j}|^2 | \sum_s \frac{f_s}{\sqrt{m_s}} e^{-M_s}|^2. \tag{2.31}$$

For a general position in reciprocal space assumptions (i) and (ii) break down and the 3n-3 optic modes contribute to the intensity. Important to note is the breakdown of assumption (ii) near the zone boundary where the displacement of the acoustic modes becomes more optic like. A polarisation selective excitation of a specific mode at arbitrary position is thus impossible.

The TDS intensity can now be interpreted in the frame of elastic theory (see for example Fedorov (1968)). Starting from the differential equations of the displacement vector $\boldsymbol{u}$

$$\rho \ddot{u}_i = c_{ijlm} \frac{\partial^2 u_m}{\partial x_j \partial x_i}, \tag{2.32}$$

where c_{ijlm} is the tensor of elastic constants, and taking a monochromatic plane wave Ansatz for the solutions one obtains

$$\rho\omega^2 u_i = c_{ijlm} k_j k_l u_m. \tag{2.33}$$

$\boldsymbol{k} = k\boldsymbol{n}$ and ω are the wave vector and the frequency of the elastic wave, respectively. Introducing the reduced elastic-modulus tensor

$$\lambda_{ijlm} = \frac{1}{\rho} c_{ijlm}, \tag{2.34}$$

one can reformulate Equation 2.33 in the form of

$$(\lambda_{ijlm} n_j n_l - v^2 \delta_{im}) u_m = 0. \tag{2.35}$$

Considering the second-rank tensor

$$\Lambda_{jm} = (\lambda_{ijlm} n_i n_l), \tag{2.36}$$

one can write 2.35 in the form of

$$(\Lambda - v^2 I)\boldsymbol{u} = 0, \tag{2.37}$$

which is known as Christoffel's equation, where I is the identity matrix. Reformulating Λ in terms of q yields

$$\Lambda_{jm}(\boldsymbol{q}) = \frac{1}{q^2}(\lambda_{ijlm} q_i q_l) = \frac{1}{\rho q^2}(c_{ijlm} q_i q_l). \tag{2.38}$$

The TDS intensities can be rewritten as follows,

$$I = \frac{\hbar N I_e}{2} \boldsymbol{Q}^t \frac{1}{q\sqrt{\Lambda(\boldsymbol{q})}} coth\Big(\frac{\hbar q \sqrt{\Lambda(\boldsymbol{q})}}{2k_B T}\Big) \boldsymbol{Q}| \sum_s \frac{f_s}{\sqrt{m_s}} e^{-M_s}|^2, \tag{2.39}$$

which further reduces for $k_B T \gg \hbar q \sqrt{\Lambda(q)}$ to

$$I = N I_e \boldsymbol{Q}^t \frac{k_B T}{q^2 \Lambda(\boldsymbol{q})} \boldsymbol{Q}| \sum_s \frac{f_s}{\sqrt{m_s}} e^{-M_s}|^2, \tag{2.40}$$

in agreement with the previously established result from elasticity theory (Wooster, 1962). Collecting TDS intensities along all directions around many Bragg reflections allows thus the determination of the full set of elastic constants (independent from q) from a simple diffraction experiment. This was a subject of investigation for several systems (Wooster, 1962). Measuring TDS with modern area detectors will allow an over determination of the eigenvalue equation and may provide an alternative tool for a precise measurement of elastic constants.

Chapter 3

Ab-initio lattice dynamics calculation

Lattice dynamics calculations are required to obtain the full description of the dynamical matrix. Experimental methods usually provide only part of the information. For a given dynamical matrix both IXS and TDS scattering intensities can be calculated following the formalism laid out in Chapter 2. Modern density functional theory, introduced in Section 3.1, provides two powerful methods for calculating the dynamical matrix *ab initio*, either by perturbation theory (Section 3.2) or by finite displacement (Section 3.3). The advantages and limitations of the two methods are discussed together with a guideline for well converged calculations (Section 3.5 and 3.6). The calculation of large numbers of $\boldsymbol{q}$-points required for the computation of TDS intensity distributions and the density of vibrational states is discussed in Section 3.4.

3.1 General strategy

The goal of a lattice dynamics calculation is to compute the second derivatives of the total energy for a given system to construct the dynamical matrix as defined in Equation 2.7. The total energy of a system can be obtained by an electronic structure calculation in the frame of density functional theory. Such calculations have become an important tool in solid state physics and quantum chemistry and allow the determination of electronic properties from first principle. A complete and comprehensive description can be found for example in Kohanoff (2006). Here, some of the key ingredients are introduced.

We make use of the adiabatic approximation (Born and Oppenheimer, 1927) which allows a decoupling of the vibrational from the electronic degrees of freedom. It assumes that the electrons instantaneously follow the motion of the nuclei,

while remaining always in the same stationary state of the electronic Hamiltonian. This approach allows the separation of nuclear and electronic wave functions. Within the frame of density functional theory these wave functions, and thus also the energy of the electronic system is exclusively determined by the electronic ground state charge density distribution. Density functional theory is based on the Hohenberg-Kohn theorem (Hohenberg and Kohn, 1964) and a practical scheme for determining the ground state was devised by Kohn and Sham (1965). The energy functional consists of different contributions which can be addressed separately. These are the non-interacting kinetic energy, the classical electron-electron interaction, the interaction of the electrons with external fields, the exchange energy and a correlation term. The most widely used approaches to the exchange and correlation terms within density functional theory are the local density and generalised gradient approximations (Kohanoff, 2006).

The wave functions for free electrons in a periodic crystal can be expanded in plane waves and they are the exact solution of the electronic problem if the potential due to the atoms is neglected. In a real crystal the potential due to the atomic nuclei can not be neglected. It exhibits singularities at the nucleus positions and results in steep wave functions. A plane wave expansion of the real wave function would therefore require an enormous number of plane wave components. Based on the two observations that: (i) the core states are highly localised and not fundamental for the chemical bonding and (ii) a good description of the valence wave functions inside the core is not strictly necessary, there is no lack of crucial information if the core wave function is replaced with a smooth and nodeless pseudo-wave function, which can be easily expanded in plane waves. The pseudo-wave function is not a solution of the atomic problem, it corresponds to the lowest energy state of an effective, pseudo-atomic problem, where the true potential is replaced by a pseudo-potential. According to Bloch's theorem the electron wave function can be expanded in a plane-wave basis set (Bloch, 1929). The Fourier components of the wave function decrease with increasing reciprocal lattice vector and the expansion can be limited to all waves with a kinetic energy below some energy cut-off.

Solving the electronic structure in practice involves the convergence towards a self-consistent solution, where the input charge density distribution equals the output one within a certain numerical tolerance. The charge density is thereby sampled on a uniform grid and the problem solved iteratively, starting with a guess for the charge density.

We can now write the total energy of the system as

$$E = \langle \Psi | \hat{\boldsymbol{H}} | \Psi \rangle, \hat{\boldsymbol{H}} = -\frac{\hbar^2}{2m_e}\nabla^2 + V_{SCF}, \tag{3.1}$$

with wave function Ψ, Hamiltonian $\hat{\boldsymbol{H}}$ and self consistent field potential V_{SCF}, in

Dirac notation. Introducing an atomic displacement perturbation λ, the force can be calculated,

$$F = -\frac{dE}{d\lambda} = -\langle\frac{d\Psi}{d\lambda}|\hat{\boldsymbol{H}}|\Psi\rangle - \langle\Psi|\hat{\boldsymbol{H}}|\frac{d\Psi}{d\lambda}\rangle - \langle\Psi|\frac{dV}{d\lambda}|\Psi\rangle. \tag{3.2}$$

In the case of $\langle\Psi|$ representing the ground state of $\hat{\boldsymbol{H}}$, the first two terms vanish. This is known as the *Hellmann-Feynman* theorem,

$$\langle\Psi|\hat{\boldsymbol{H}}|\frac{d\Psi}{d\lambda}\rangle = \epsilon_n\langle\Psi|\frac{d\Psi}{d\lambda}\rangle = 0, \tag{3.3}$$

where ϵ_n are the Kohn-Sham eigenvalues. The solution of the stationary problem corresponds to an energy minimisation which is referred to as geometry optimisation. Such a geometry optimisation can be performed for a given structure and is well defined also in the presence of external stress (Pfrommer et al., 1997). A variation of internal and cell parameters is referred to as full geometry optimisation. The force constants are the second derivatives of the total energy

$$k = \frac{d^2E}{d\lambda^2} = \langle\frac{d\Psi}{d\lambda}|\frac{dV}{d\lambda}|\Psi\rangle + \langle\Psi|\frac{dV}{d\lambda}|\frac{d\Psi}{d\lambda}\rangle - \langle\Psi|\frac{d^2V}{d\lambda^2}|\Psi|\rangle \tag{3.4}$$

and none of the terms vanishes. The second derivatives of the energy require the linear response of the wavefunctions with respect to the perturbation $\left(\langle\frac{d\Psi}{d\lambda}|\right)$. This may be accomplished either by a finite-displacement method, calculating the total energy for small displacements of each atom in all directions (finite displacement, Section 3.3) or by computing first order response orbitals by density functional perturbation theory (DFPT, Section 3.2). A more detailed description can be found elsewhere (Baroni et al., 2001).

3.2 Density functional perturbation theory

The linear response to λ, which may be a displacement of atoms with wavevector $\boldsymbol{q}$ or an electric field, requires the first order Kohn-Sham orbitals $\Phi^{(1)}$. These orbitals have a Bloch-like representation

$$\Phi^{(1)}_{\boldsymbol{k},\boldsymbol{q}}(\boldsymbol{r}) = e^{-i(\boldsymbol{k}+\boldsymbol{q})\boldsymbol{r}}u^{(1)}, \tag{3.5}$$

where $u^{(1)}$ has the periodicity of the unit cell. The perturbation can thus be performed at arbitrary $\boldsymbol{q}$ in the primitive cell description. The first order response orbitals are the solutions of the Sternheimer equation

$$\left(H^{(0)} - \epsilon^{(0)}_l\right)|\Phi^{(1)}_l\rangle = -P_c v^{(1)}|\Phi^{(0)}_l\rangle, \tag{3.6}$$

where P_c is the projection operator onto unoccupied states and $v^{(1)}$ the first order potential which includes response terms of Hartree and exchange correlation potentials. $v^{(1)}$ depends on the first order density which in turn depends on the first order Kohn-Sham orbitals. Finding $\Phi^{(1)}$ is thus a self consistent problem, just like solving the Kohn-Sham equations for the ground state. The self consistent field can be solved using a formalism based on Green's function (Baroni et al., 2001) or a variational principle (Gonze, 1997). The developments introduced in Baroni et al. (2001) and Gonze (1997) showed that these quantities can be calculated as accurately as the square roots of the ground state properties derived from density functional theory. The variational formulation is particularly elegant. It is based upon the $2n+1$ theorem, stating that the $(2n+1)th$-order response of the energy may be calculated using only the n-th order response of the Kohn-Sham orbitals. The method can be formulated as a minimisation problem with respect to the basis-set coefficients. The full description of the formalism can be found in Gonze (1997) and Gonze and Lee (1997). The calculation of Raman and infrared intensities requires the third derivatives in energy, which may be computed for a very well converged structure (Giannozzi and Baroni, 1994).

Polar systems

The total energy in the case of polar systems consists of a contribution from the electron system and a contribution from the electrostatic energy between the ions. Similarly, the dynamical matrix split in two parts,

$$C^{\alpha,\alpha'}_{s,s'}(\boldsymbol{q}) = C^{\alpha,\alpha'}_{el,s,s'}(\boldsymbol{q}) + C^{\alpha,\alpha'}_{Ew,s,s'}(\boldsymbol{q}). \tag{3.7}$$

The electronic contribution $C^{\alpha,\alpha'}_{el,s,s'}(\boldsymbol{q})$ is obtained from the knowledge of the first-order wave functions with respect to one perturbation. The ion-ion contribution $C^{\alpha,\alpha'}_{Ew,s,s'}(\boldsymbol{q})$ requires the mixed second-order derivative of the energy with respect to atomic displacements and a macroscopic electric field. The long-range Coulombic tail of the dynamical matrix of a polar system can be modelled using a generalised electrostatic dipole- dipole interaction of pseudo ions with charges given by the Born effective charges in an effective dielectric medium (Dal Corso and Mauri, 1994). By subtracting the tail computed using this model the remainder of the dynamical matrix is short-ranged decaying as $1/r^5$. Fourier interpolation of this charge subtracted set may be converged using a much coarser grid of $\boldsymbol{q}$-points than the original dynamical matrix. As a final step the dipole-dipole model contribution to the dynamical matrix is added back at the interpolated $\boldsymbol{q}$-points. $C^{\alpha,\alpha'}_{Ew,s,s'}(\boldsymbol{q})$ is direction dependent and has a non-analytic behaviour at $\boldsymbol{q} = 0$ resulting in the spitting of longitudinal optical and transverse optical modes. The formula at arbitrary momentum transfer and its limit for $\boldsymbol{q} = 0$ can be found in Gonze and Lee (1997).

Metals

DFPT is directly applicable to metals at zero temperature where a clear separation between occupied and unoccupied states is possible. The number of k-points required to correctly represent the Fermi surface is, however, very large and perturbation calculations may become prohibitively expensive in computer time and memory. A practical implementation has been proposed by de Gironcoli (1995) in the pseudo-potential formalism, based on a smearing technique for dealing with Fermi effects. In this approach the Kohn-Sham energy levels are broadened by a smearing function,

$$\delta_\sigma(\epsilon) = \frac{1}{\sigma}\tilde{\delta}(\epsilon/\sigma), \tag{3.8}$$

which is an approximation to Dirac's δ function that becomes exact for vanishing linewidth σ. $\tilde{\delta}$ can be any function that integrates to unity, for example a Gaussian or Lorentzian or the derivative of the Fermi-Dirac function. The latter somewhat mimics the electronic temperature (Baroni et al., 2001). The approximated local density of electronic states is the original density of electronic states convoluted with the smearing function

$$n(\boldsymbol{r},\epsilon) = \sum_i \frac{1}{\sigma}\tilde{\delta}\big(\frac{\epsilon-\epsilon_i}{\sigma}\big)|\Psi_i(\boldsymbol{r})|^2, \tag{3.9}$$

where the sum refers to the discrete k-vector index and to band and spin indices for all bands. The electron density is given by

$$n(\boldsymbol{r}) = \int_{-\infty}^{\infty} n(\boldsymbol{r},\epsilon)d\epsilon. \tag{3.10}$$

Advantages and Limitations

The main advantage of DFPT amongst all other methods is the feasibility to perform perturbations on the primitive cell at arbitrary momentum transfer. The splitting of longitudinal optical and transverse optical modes is included via the ion-ion interaction which allows for the treatment of polar systems. Metallic systems can be treated with an adequate smearing scheme for Fermi surface effects. The price to pay is a complex formalism which requires a lot of programming. Anharmonic terms in the lattice dynamics can be computed by evaluating higher order response (Debernardi et al., 1995).

3.3 Finite displacement method

An alternative method of computing the dynamical matrix consists in numerical differentiation of forces while atoms are displaced by a small amount from their

equilibrium positions. The total energy of the system can be calculated for the situation where the ion s' is displaced in direction α' by a small distance $\pm u$. The forces are then obtained by the central-difference formula,

$$\frac{dF_{s,\alpha}}{du_{s,\alpha}} \approx \frac{F^{+}_{s,\alpha} - F^{-}_{s,\alpha}}{2u_{s,\alpha}} = \frac{d^2E_0}{du_{s,\alpha}du_{s',\alpha'}}, \tag{3.11}$$

where $F^{+}_{s,\alpha}$ and $F^{-}_{s,\alpha}$ denote positive and negative displacements, respectively. By iterative evaluation of the numerical derivative for displacements on every ion in each direction one obtains the dynamical matrix at zero momentum transfer. In order to obtain the dynamical matrix at arbitrary momentum transfer, one may take advantage of the short range nature of the real-space force constant matrix $\Phi^{\alpha,\alpha'}_{l,s,l',s'}$. The elements of the force constant matrix in Equation 2.2 decrease in fact as $1/r^5$ with interatomic distance for most non-polar insulators and metals, $\Phi^{\alpha,\alpha'}_{l,s,l's'} \to 0$ as $\boldsymbol{R}_m \to \infty$. Introducing a supercell (Frank et al., 1995) which consists of $p \times q \times r$ primitve cells one finds that the dynamical matrix at $\boldsymbol{q} = 0$ of a supercell is the real-space force constant matrix in the m-th unit cell,

$$C^{\alpha,\alpha'}_{s,s'}(\boldsymbol{q}_{\text{supercell}} = 0) = \Phi^{\alpha,\alpha'}_{l,s,l's'}, \tag{3.12}$$

if the supercell sizes L_i are larger than twice the distance beyond which the force constants are treated as zero. The dynamical matrix of the primitive cell at arbitrary $\boldsymbol{q}$ is obtained by Fourier transformation,

$$C^{\alpha,\alpha'}_{s,s'}(\boldsymbol{q}) = \frac{1}{\sqrt{m_s, m'_s}} \sum_m \Phi^{\alpha,\alpha'}_{l,s,l's'} e^{i\boldsymbol{q}\boldsymbol{R}_l}. \tag{3.13}$$

The method can be adapted for polar systems with long range forces (Yin and Cohen, 1980).

Advantages and Limitations

The main advantage of the finite displacement method is its general character, it can be applied to any system. A further advantage is the choice of the displacement amplitude. Large displacement amplitudes allow to include anharmonic effects to some limited extent and dynamical stabilisation may be obtained (Antolin et al., 2012). The formalism is less complex and can be programmed as extension to many total energy codes. One has, however, to deal with supercells whose size depend on the range of the internal forces. Calculations for systems containing many electrons and long ranging forces can get prohibitively expensive in computation time and memory.

3.4 Fourier interpolation of dynamical matrices

The DFPT formalism requires a self-consistent perturbation calculation for every single $\boldsymbol{q}$-point. The calculation of precise phonon dispersion curves requires hundreds and 3D TDS intensity distributions or VDOSs thousands of $\boldsymbol{q}$-points. The calculation of a large number of $\boldsymbol{q}$-points within very reasonable computational expense is possible taking advantage of the short-range nature of the real-space force constant matrix $\Phi^{\alpha,\alpha'}_{l,s,l's'}$, as in the finite displacement method. The approximation of $\Phi^{\alpha,\alpha'}_{l,s,l's'}$ in a $p \times q \times r$ supercell is given by the Fourier transform of the dynamical matrices on a $p \times q \times r$ grid,

$$\Phi^{\alpha,\alpha'}_{l,s,l',s'} = \sum_{\boldsymbol{q}} C^{\alpha,\alpha'}_{s,s'}(\boldsymbol{q}) e^{i\boldsymbol{q}\boldsymbol{r}_s}, \tag{3.14}$$

see Section 2.1 for the notation. The dynamical matrix at any desired $\boldsymbol{q}$-point in the primitive cell description is obtained by Fourier transformation, as in the finite displacement method using a supercell. The method can be refined by including all image forces, referred to as cumulant method (Parlinski et al., 1997). In the case of polar systems the Fourier interpolation can be performed on the electronic part of the force constants. The ion-ion contribution with longer ranged Coulomb forces (they vary with $1/r^3$) can be handled analytically via the Born effective charges and added after the Fourier interpolation. In the case of metals a larger set of $\boldsymbol{q}$-points is required in order to accurately describe the electron-phonon interaction. Taking advantage of this method reduces the number of expensive DFPT calculation to a reasonable number of $\boldsymbol{q}$-points for the calculation of the dynamical matrix $C^{\alpha,\alpha'}_{s,s'}$ on a dense grid or fine path.

3.5 Convergence criteria

Ab-initio lattice dynamics calculation are very sensitive to several convergence issues, discussed in the following.

Electronic structure

A very well converged geometry is the pre-requisite for any lattice dynamics calculation. The energy expansion Equation 2.1 makes the explicit assumption that the system is in mechanical equilibrium and that all internal atomic forces are zero. External stress can be present; the lattice dynamics is in fact well defined at any stress or pressure. A high level of plane-wave cutoff, self consistent field and electronic k-point sampling is required to achieve well converged dynamical

matrices. The requested convergence tolerance is system dependent and can require internal forces to be converged within $< 10^{-3}$ eV/Å. Each parameter must be independently tested for convergence. The force constant matrix $\Phi_{l,s,l',s'}$ is positive definite for a lattice dynamics calculation performed in the geometrical configuration which minimises the total energy of the system. If the system is not in a minimum energy equilibrium configuration, $\Phi_{l,s,l',s'}$ is not necessarily positive definite resulting thus eventually in negative eigenvalues.

Convergence of the DFPT solver

The convergence of the perturbation calculations depends strongly on the convergence of the ground state electron density and wave functions. The DFPT equations include the ground-state wave functions, both, directly and as a consequence of the orthogonality condition between ground-state and first-order response orbitals (Gonze and Lee, 1997, Refson et al., 2006). The error in the second derivatives of the energy is variational and depends thus quadratically on the error in the first order response orbitals. In order to achieve phonon energies converged to 0.1 meV the total energy per atom must be converged within $\approx 10^{-10}$ eV/Å^2.

Convergence of the finite displacement method

The evaluation of the numerical derivatives of forces requires the knowledge of the total energy with the same accuracy as in the case of DFPT. The size of the supercell for computing the dynamical matrix at arbitrary wave vector must be chosen carefully. It must be large enough to exceed the spatial range of the forces in order to cope with the variation of the dynamical matrix. Force constants outside the supercell must be negligible small.

Convergence of the Fourier interpolation

The accuracy of the Fourier interpolation depends on the number of primitive cells taken to construct the supercell. The real force constants outside the supercell are treated as zero. The number of primitive cells must be large enough to exceed the spatial range of the forces. A too large supercell on the other hand can lead to high-frequency artefacts in the dynamical matrix calculated by the performed perturbations. In this case perturbation calculations on a finer $\boldsymbol{q}$-grid are required. The shape of the supercell should be as close to cubic as possible, irrespective of the shape of the primitive cell, in order to optimise the ratio of the supercell size to the distance at which the force constants may be neglected. The symmetry of the supercell should, however, be compatible with the primitive cell. Best convergence is obtained for a grid containing the Γ-point.

Sum rules

The convergence of phonon calculations close to and at Γ can be monitored by the help of two sum rules.

(i) Acoustic sum rule (Born and Huang, 1954). The total energy and thus also the vibrational Hamiltonian is invariant to a uniform translation of the system in space. This symmetry argument requires the eigenfrequencies of the three acoustic modes at Γ to be zero and can be formulated in real and reciprocal space with expressions for the force constants and dynamical matrices,

$$\sum_{s,m} \Phi^{\alpha,\alpha'}_{l,s,l's'} = 0, \sum_{s} C^{\alpha,\alpha'}_{s,s'}(\boldsymbol{q}=0) = 0. \tag{3.15}$$

The translational invariance is not exactly satisfied in plane wave calculations as the exchange-correlation potential and energies are evaluated on a fixed grid in real space. The translation of all atoms by an arbitrary vector results in small energy changes. Consequently the acoustic sum rule is violated. The dynamical matrices (or the force constant matrix) can be corrected by a transformation so that the sum rule is satisfied (Gonze and Lee, 1997):

$$\tilde{C}^{\alpha,\alpha'}_{s,s'}(\boldsymbol{q}=0) = C^{\alpha,\alpha'}_{s,s'}(\boldsymbol{q}=0) - \delta_{s,s'} \sum_{s''} C^{\alpha,\alpha'}_{s,s''}(\boldsymbol{q}=0). \tag{3.16}$$

By this operation the eigenfrequencies at $\boldsymbol{q} = \boldsymbol{0}$ will change. A generalisation for $\boldsymbol{q} \neq \boldsymbol{0}$ can be obtained using the Ewald summation technique (Pick et al., 1970),

$$\tilde{C}^{\alpha,\alpha'}_{s,s'}(\boldsymbol{q}) = C^{\alpha,\alpha'}_{s,s'}(\boldsymbol{q}) - \delta_{s,s'} \sum_{s''} C^{\alpha,\alpha'}_{s,s''}(\boldsymbol{q}=0), \tag{3.17}$$

which results in a wavevector-independent correction on the site-diagonals of the dynamical matrices. In addition to translational invariance one may also make use of the index symmetries of the force constants,

$$\Phi^{\alpha,\alpha'}_{l,s,l',s'} = \Phi^{\alpha,\alpha'}_{-l,s,-l's'} \tag{3.18}$$

and rotational invariance

$$\sum_{l,s} \left(\Phi^{\alpha,\alpha'}_{l,s,l',s'} R^{\alpha''}_{s'} - \Phi^{\alpha,\alpha''}_{l,s,l',s'} R^{\alpha'}_{s'} \right) \tag{3.19}$$

about the axis R^{α}_{s}. This has the advantage of not violating the Hermitian or point group symmetry invariance of the dynamical matrix. A sophisticated version of the acoustic sum rule correction based on a projection method (Mounet, 2005) is implemented in modern codes such as QUANTUM EXPRESSO (Giannozzi et al., 2009) and CASTEP (Clark et al., 2005).

(ii) Sum rule for Born effective charges (Pick et al., 1970). The charge neutrality must be fulfilled at the level of the Born effective charges, $Z_s^{\alpha,\alpha'}$. The sum of these charges of all atoms in one unit cell must vanish,

$$\sum_s Z_s^{\alpha,\alpha'} = 0. \tag{3.20}$$

The finite number of plane waves or the evaluation of exchange-correlation potentials and energies on a discrete grid breaks this rule. A correction scheme based on the mean effective charge excess can be found elsewhere (Gonze and Lee, 1997).

3.6 Lattice dynamics calculations in practice

The different steps for a typical *ab initio* lattice dynamics calculation within the plane wave formalism employing pseudo-potentials is illustrated in Figure 3.1. The total energy is calculated for a given electronic structure in the primitive cell description. Convergence tests are performed by evaluating internal forces for different sampling of the electron density and levels of the plane wave cut-off as well as for the self-consistent field. Accurate pseudo-potentials are required in order to achieve the high level precision in the total energy. A rigorous geometry optimisation follows for all systems for which the forces are not necessary zero by symmetry. A high level structure optimisation to the requested precision is mandatory for a good lattice dynamics calculation (see Section 3.5).

Phonon calculations can now be performed by DFPT or by the finite displacement method. If DFPT is chosen the dynamical matrix can be calculated for arbitrary $\boldsymbol{q}$-points. Convergence criteria need to be evaluated on the level of the DFPT solver and can be performed at an arbitrary $\boldsymbol{q}$-point. Γ-point calculations are in particular useful for monitoring the convergence with the sum rules. If dispersion relations or the dynamical matrices on a fine $\boldsymbol{q}$-sampling are desired, perturbation calculations are performed on a uniform $\boldsymbol{q}$-grid which allows for Fourier interpolation. The number of grid points can be efficiently reduced by symmetry following the ideas of Monkhorst and Pack (1976), referred to as Monkhorst Pack grid. The required sampling is again system dependent and needs to be checked for convergence. Dispersion relations and a fine $\boldsymbol{q}$-sampling are finally obtained by Fourier interpolation.

The procedure for a phonon calculation employing the finite displacement method follows a similar line. Γ-point calculations are performed and the convergence criteria for the numerical derivatives and the displacement amplitude is evaluated. For the calculation of $\boldsymbol{q}$-points other then Γ a supercell must be constructed and a Γ-point phonon calculation of this supercell is performed. The size

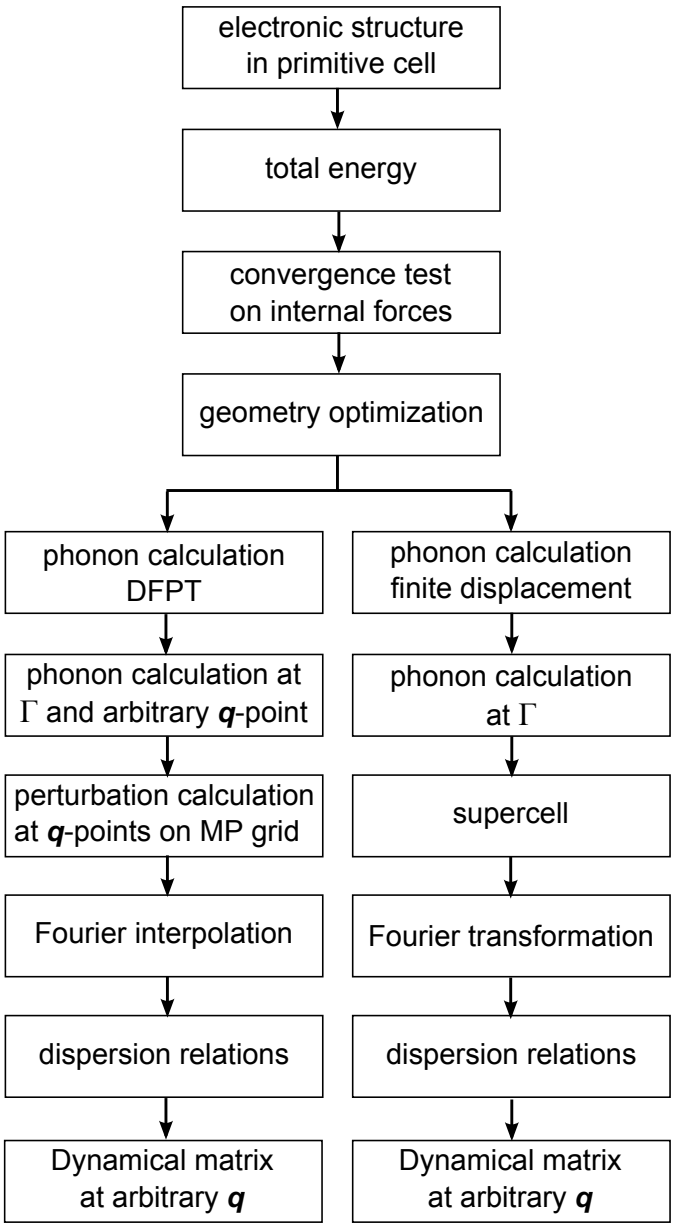

Figure 3.1: Schematic overview of a typical lattice dynamics calculation using either DFPT (left branch) or the finite displacement method (right branch). See text for further details.

of the supercell must be tested. Dynamical matrices along a dispersion curve or on a dense grid may finally be obtained by Fourier transformation.

Chapter 4

Experimental techniques

4.1 Diffuse scattering setup

The experimental geometry of a diffuse scattering experiment is identical to x-ray diffraction. Monochromatic X-rays are scattered from the sample, preferable in transmission geometry, and the scattered intensity distribution is recorded by an area detector. Care needs to be taken in the reduction of background scattering and read-out noise of the detector due to the weak signal. Air scattering can be minimised by using a collimator in front of the sample and a beamstop behind it. The conceptual design of a suitable beamline (ID29 at the ESRF) is sketched in Figure 4.1. Synchrotron radiation is monochromatised by a pair of channel-cut silicon crystals (Si (1 1 1) and Si (3 1 1) reflection) providing an energy resolution $\Delta E/E = 10^{-5}$. The X-rays are focused by a toroidal mirror; a second mirror takes care of the rejection of higher harmonics. The background is massively reduced by the slits. The incoming x-ray energy is chosen by the scattering angle of the monochromators. The sample is mounted on a goniometer (see Figure 5.4) and the direct beam is blocked by a beamstop behind the sample. The intensity is collected by a pixel detector with practically no dark noise. Technical details of ID29 can be found elsewhere (de Sanctis et al., 2012).

The choice of a suitable detector is essential for the quantitative analysis of 3D TDS intensity distributions. Silicon hybrid pixel detector systems are currently the best option available for TDS studies with x-ray energies of below 20 keV. Area detectors made of such devices are for example the PILATUS detector (Kraft et al., 2009). Such detectors can be operated in single photon counting mode. Each pixel is read out individually. These detectors possess no dark current and no read-out noise, provide a good point spread function, high quantum efficiency, and a high dynamic range. The read-out time is in the ms range, thus shutterless data collection becomes possible. Fluorescence can be largely suppressed by setting an

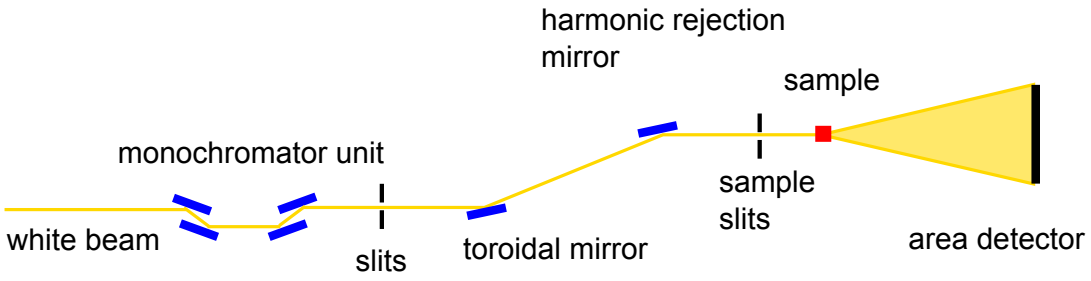

Figure 4.1: Schematic lay-out of ID29, a beamline suitable for diffuse scattering studies. See text for details.

energy threshold. The energy resolution of the PILATUS detector is, for example, 500 eV. The mar345 detector (Marresearch GmbH), based on the image plate technique, is a suitable alternative. The readout time is much higher (> 60 s) and an energy threshold is not implemented. Most of the presented TDS results were measured at beamline ID29 and the Swiss-Norwegian Beamline BM01A. The latter provides a more flexible sample environment and got recently equipped with the PILATUS 2M detector, but the total flux is lower and the x-ray beam size is larger. The diffraction geometry and experimental strategy for collecting 3D TDS intensity distributions are discussed in Chapter 5.

4.2 Inelastic x-ray spectrometer

The instrumental concept of the IXS beamline ID28 is based on a triple axis spectrometer (Burkel, 2000, Krisch and Sette, 2007). X-rays are monochromatised using the very high energy resolution monochromator selecting the energy of the incoming beam. The sample position and orientation are controlled by the goniometer and translational stage. The chosen scattering angle determines the momentum transfer. The crystal analyser specifies the scattered photon energy. The schematic layout of a triple axis IXS spectrometer is illustrated in Figure 4.2.

The synchrotron radiation with a bandwidth of $\Delta E/E \approx 10^{-2}$ and an integrated power of ≈ 200 W is monochromatised by a series of three optical devices (see Figure 4.3). Pre- and post-monochromator improve the energy resolution to $\Delta E/E \approx 10^{-4}$ and then to $\Delta E/E \approx 10^{-5}$. Their main task is to reduce the heat load on the main monochromator. They consist of Si (1 1 1) and Si (4 0 0) channel-cut single crystals kept in high vacuum. The pre-monochromator crystal is cooled by liquid nitrogen. A collimator unit made of beryllium lenses ensures the angular acceptance of the post-monochromator, which is water cooled. The main monochromator operates in backscattering geometry at a Bragg angle of

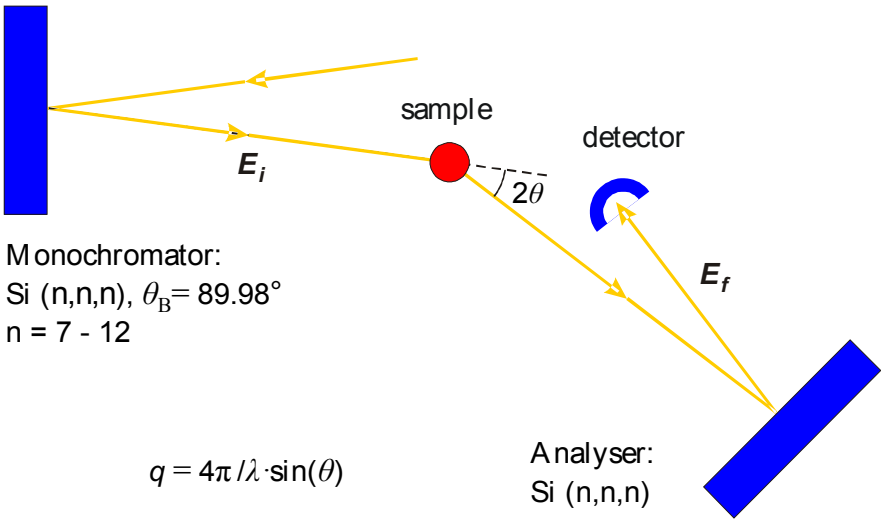

Figure 4.2: Schematic layout of a triple axis IXS spectometer. The precise value of the energy of the X-rays is determined by the monochromator and analyser. The momentum transfer $\boldsymbol{Q}$ of the measured photon is defined by the scattering angle 2θ.

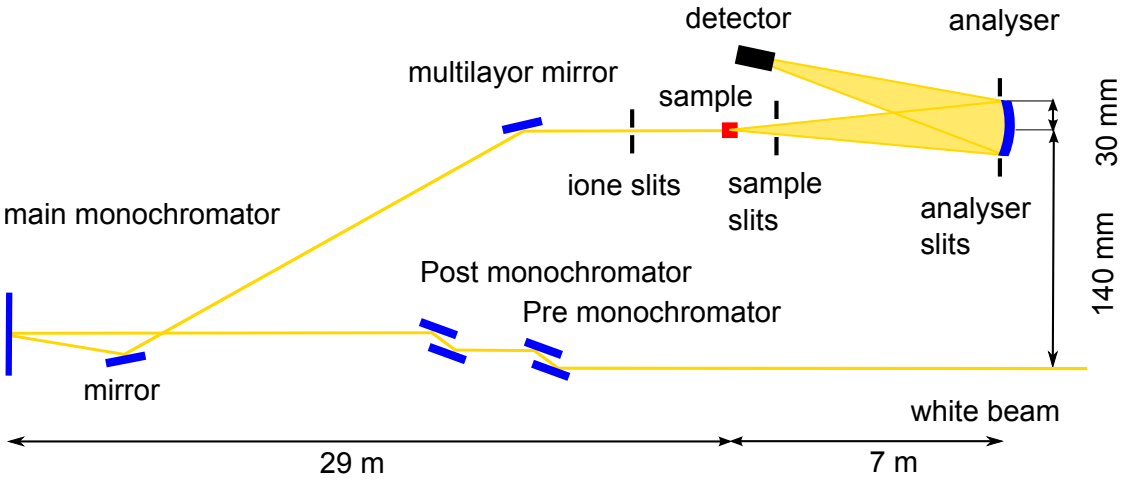

Figure 4.3: Sketch of the IXS beamline ID28 at the ESRF. See text for a detailed explanation.

89.98°. This ensures minimal geometrical contribution to the energy resolution. A high-order Bragg reflection and a perfect crystal are mandatory to obtain an energy resolution of $\Delta E/E \approx 10^{-7} - 10^{-8}$. The chosen reflection of the main monochromator determines the incident energy E, resolution ΔE, and the flux of the x-ray beam. The best energy resolution can be achieved using the Si(13 13 13) reflection providing $E = 25.704$ keV, $\Delta E = 1.0$ meV, and a flux of 1.5×10^9 photons per seconds. A good compromise between resolution and flux is the Si (9 9 9) reflection with $E = 17.794$ keV, $\Delta E = 3.0$ meV, and a flux of 2.7×10^{10} photons per second. The spot size of the x-ray beam at the sample position can be chosen by applying on of the following focusing schemes. (i) Horizontal and vertical focusing is achieved by a platinum-coated toroidal mirror, located 25 m from the sample position, resulting in a spot size of 270 × 70 μm (horizontal × vertical). (ii) The cylindrical part of the mirror is used for vertical focusing and a multilayer mirror is used for horizontal focusing. This scheme results in a spot size of 14 × 60 μm. (iii) The x-ray beam from the main monochromator deflects the beam slightly upwards (thus not utilising the toroidal mirror) and is focused in the vertical direction by a platinum-coated mirror located 2.5 m away from the sample and the same multilayer mirror for horizontal focusing as in configuration (ii) is used. This scheme results in a spot size of 14 × 7 μm.

Parasitic scattering contribution is blocked by the sample slits. The momentum transfer resolution is set by the analyser slits and typically in the order of 0.3 × 0.9 nm^{-1} (horizontal × vertical). The energy of the scattered photons is analysed by silicon crystals which Bragg-diffract the photons into detectors. The big challenge of building an analyser is to ensure that the Bragg angles are identical for all photons entering this device. The analyser must therefore have a spherical surface whose radius equals the sample-analyser distance (*Rowland condition*). It can be realised by a stress free arrangement of approximately 12 000 flat single silicon crystals (surface size 0.6×0.6 mm^2) on a spherical substrate (Masciovecchio et al., 1996). X-rays are detected without angular contribution to the energy resolution and the intrinsic resolution is preserved due to unstressed single crystals. The analysed photons are detected by a silicon diode detector with an active area of 3×8 mm^2. It is inclined at 20° with respect to the backscattered x-ray beam from the analysers. The photoelectric absorption is maximised within its active thickness of 1.5 mm. The detector has a very low dark noise level of about 1 count in 30 min. The inelastic scattering beamline ID28 is equipped with nine analysers arranged in the horizontal plane with a fixed angular offset. They are mounted on a 7 m arm which can be rotated between 0 and 55° around a vertical axis passing through the sample position. The set-up allows spectra to be recorded at nine momentum transfers simultaneously. When performing experiments one chooses a set of momentum transfers via the scattering angle 2θ and the orientation

of the sample. The energy is scanned by changing the temperature T of the main backscattering monochromator corresponding to the precise change of the lattice parameter of the crystal. The temperature of the analyser is kept constant. According to Bragg's law

$$\frac{nhc}{E} = 2d\sin\theta, \tag{4.1}$$

a relative variation of the lattice parameter Δd corresponds to a variation of the diffracted energy $\Delta E/E = -\Delta d/d$. The expansion of the lattice parameter with the temperature is given by

$$\frac{\Delta d}{d} = \alpha(T)\Delta T. \tag{4.2}$$

The temperature dependent expansion coefficient $\alpha(T)$ has been precisely measured by x-ray interferometry (Bergamin et al., 1997)

$$\alpha(T) = \alpha_0 + \beta\Delta T, \tag{4.3}$$

with $\alpha_0 = 2.581\pm0.002\times10^{-6}$ K^{-1}, $\beta = 0.016\pm0.004\times10^{-6}$ K^{-2}, $\Delta T = T - T_0$, and $T_0 = 22.5$ ℃. Inserting this relation into Equation 4.2 one obtains an expression for the conversion of temperature to energy shift

$$\frac{\Delta E}{E} = -\int_{T_0}^{T} \alpha_0 + \beta(T' - T_0)dT' = -(\alpha_0 - \beta T_0)\Delta T + \frac{1}{2}\beta(T^2 - T_0^2). \tag{4.4}$$

The required energy resolution of $\Delta E/E = 10^{-7}$ implies a very accurate temperature control of the main monochromator in the mK-range. It is realised by a carefully designed temperature bath controlled by an active feedback system. The instrumental resolution function is determined by scattering from a plexiglass sample at $q = 10$ nm^{-1} and $T = 10$ K, where the inelastic contributions to the signal are minimised. The recorded resolution function for the Si (9 9 9) reflection has a full-width half-maximum of 3.0 meV and is best fitted with a pseudo-Voigt function. The resolution function for this configuration is shown in Figure 4.4 for one analyser on linear and logarithmic scales together with the corresponding fit. The intensity is normalised to the incoming flux and then scaled such that the total area under the curve equals unity.

The count rate of an inelastic scattering experiment is determined by the incoming flux, the scattering cross section, the illuminated volume and the efficiency of the analysers. The minimal time per energy point is determined by the time required for temperature stabilisation. The collecting times vary thus between 10 s up to a few min per energy point.

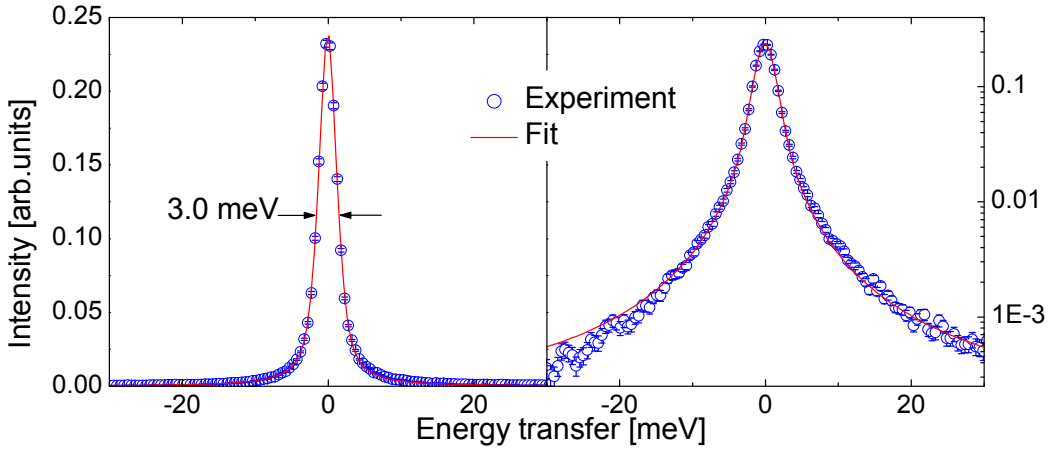

Figure 4.4: Instrumental resolution function in the Si(9 9 9) configuration determined from the elastic scattering of plexiglass at $q = 10$ nm^{-1} and $T = 10$ K.

4.3 Integration of a diffuse scattering setup on the IXS spectrometer

TDS and IXS are traditionally performed in two independent experiments due to the conceptional difference in the experimental geometry. Combining the two studies in a single experiment offers unique possibilities in the study of lattice dynamics. Interesting features in the TDS intensity distribution can be analysed using the area detector and studied under the same experimental conditions with the IXS spectrometer. This is in particular of interest for delicate sample environments under extreme conditions involving high pressure cells, cryostats, laser heating, etc.

The integration of a PILATUS detector on the IXS spectrometer ID28 is possible and was tested in the frame of this work. The conceptional realisation is depicted in Figure 4.5. Moving the IXS spectrometer to a scattering angle of 40° frees enough space to bring in the PILATUS detector for diffuse scattering measurements in a comfortable position. In order to provide a flexible sample environment, the incoming X-rays leave the vacuum tube about 400 mm before the sample position. The background scattering from the slit unit and the air are prevented to contribute to the IXS spectra by the small aperture and focal depth of the spectrometer. In the case of diffuse measurements using an area detector the background contribution could be significantly reduced by the installation of an absorption plate and a thin collimator tube inserted in the beam path in front

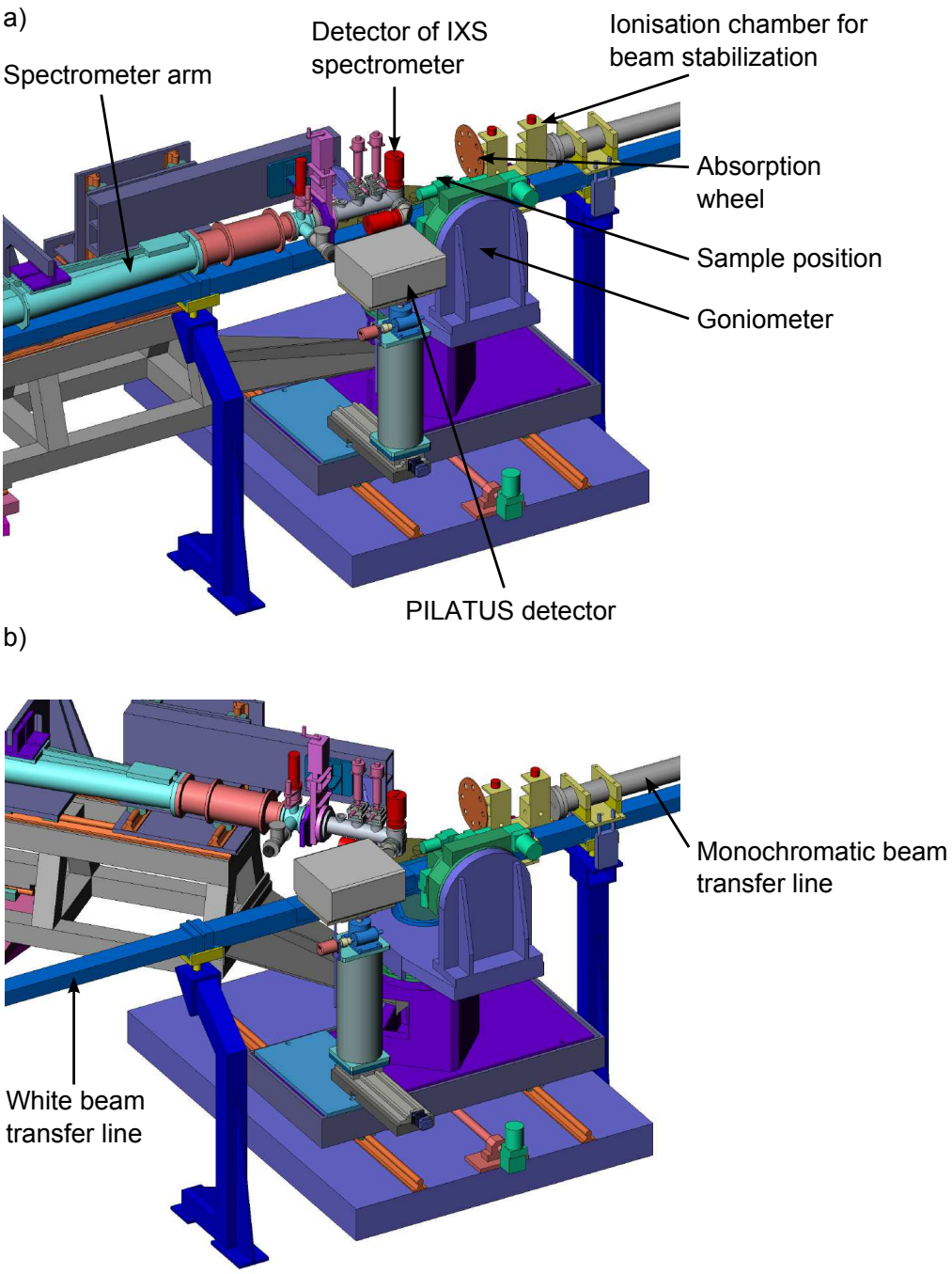

Figure 4.5: Integration of the PILATUS 300K detector on the IXS spectrometer ID28. a) Working position of IXS spectrometer at small angles, the PILATUS detector is moved out. b) Working position of PILATUS detector with IXS spectrometer at 40°. The set-up for diffuse scattering requires further equipment for background reduction, see Figure 4.6

of the sample. The experimental realisation is shown in Figure 4.6

The concept was tested on a β-tin single crystal. The diffuse scattering around the (2 2 0) reflection measured at 100°C with the PILATUS 300K detector is shown in Figure 4.7 in standard configuration (a) and with the additional equipment for background reduction (b). Diffuse features are resolved with good statistics in the latter case. The count rate is low due to the limited flux of the highly monochromatic X-rays ($\approx \Delta E/E = 10^{-8}$) provided by the backscattering geometry. Such extreme energy resolution is required for IXS measurements, but not for diffuse scattering. In order to increase the energy band width, a scheme based on a temperature gradient on the backscattering monochromator is currently under investigation. A suitable monochromator crystal requires an maximised ratio of absorption to extinction length, i. e. diamond. An alternative scheme based on a multi crystal monochromator unit was found to be unpractical.

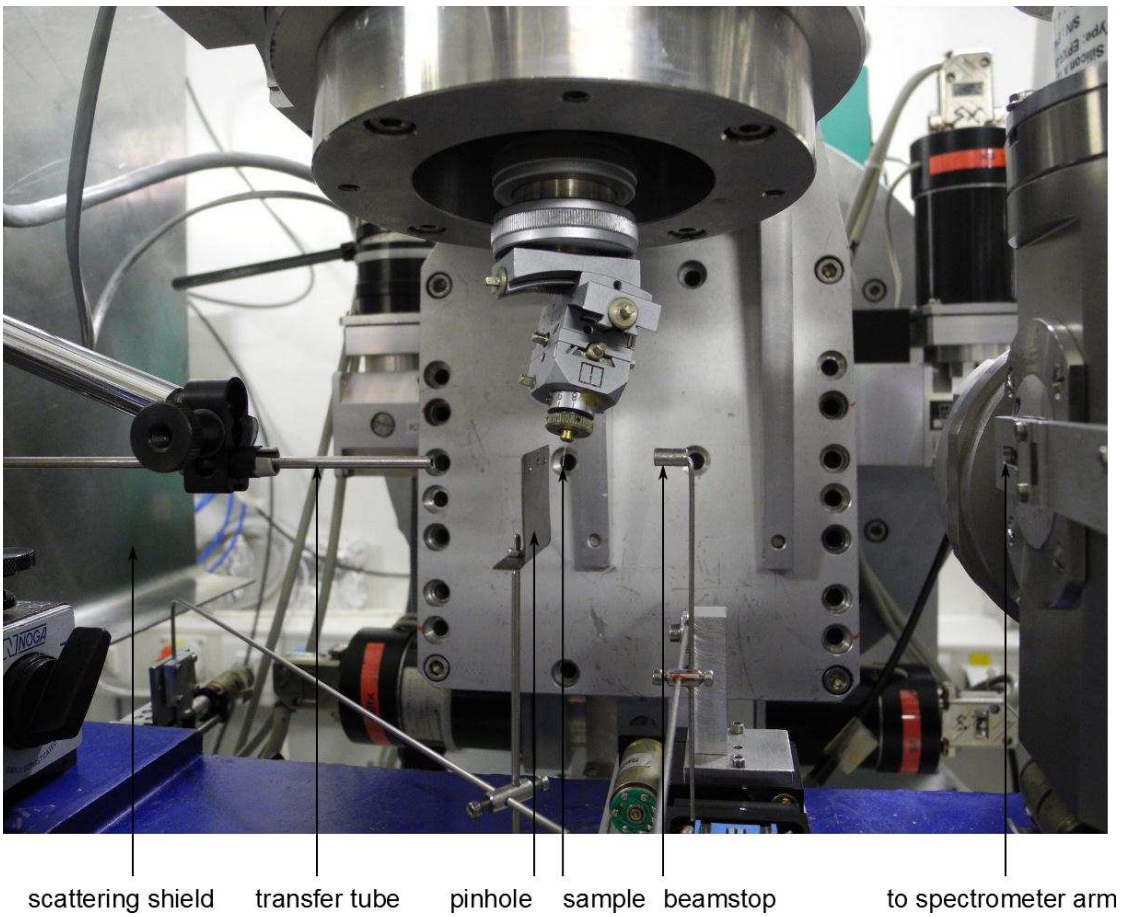

Figure 4.6: Diffuse scattering setup with background reduction on ID28. Background scattering from the slit unit and air scattering is effectively reduced by inserting a scattering shield and a collimator tube of 2 mm diameter. The sample (β-tin single crystal needle of 100 μm diameter) is mounted on a goniometer head which in turn is mounted on the four circle goniometer. The PILATUS detector, installed behind the spectrometer arm, is not visible.

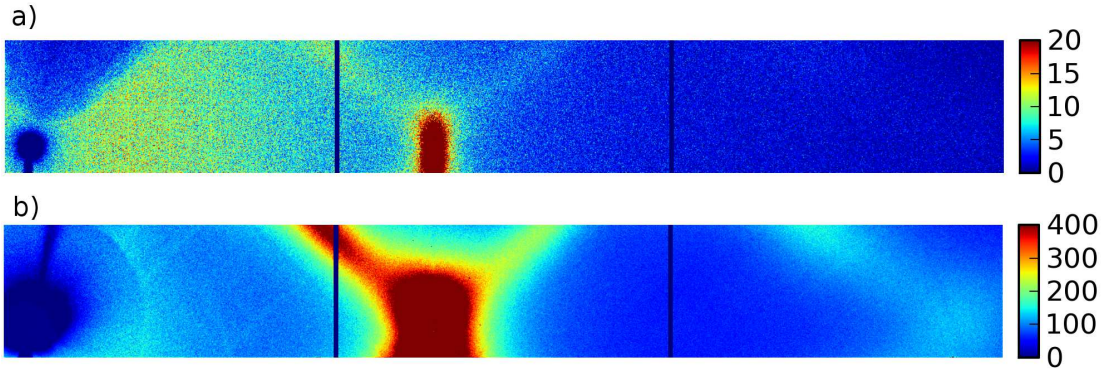

Figure 4.7: Diffuse scattering of β-tin around the (220) reflection at 100°C measured with the PILATUS 300K detector at the IXS spectrometer ID28. a) Standard configuration without background reduction (counting time 1s). b) With background reduction equipment (counting time 100s). The intensity displayed in colours is given in counts per s (a) and counts per 100 s (b). The image is the projection of part of the Ewald sphere onto the detector (see Chapter 5). Strong diffuse features are visible around the Bragg reflection and weak features further out in reciprocal space (right side). The shadow of the beam stop and its holder is visible on the left of the image. The origin of reciprocal space is in the center of the beam stop shadow. The vertical lines separate the three active detector moduli, total size 1475 $\times$ 195 pixels.

Chapter 5

Data analysis

Different aspects of the data analysis are discussed in the following. Section 5.1 - 5.5 describe the analysis of the TDS intensity distribution. In order to collect diffuse scattering in 3D reciprocal space the crystal is rotated around an axis perpendicular to the incoming X-rays and diffuse scattering patterns are collected with a 2D detector. This leads to some geometrical effects which need to be taken into account. These are discussed in Section 5.1 and 5.3. Various types of diffuse scattering apart from TDS are discussed in Section 5.6. Section 5.7 describes the analysis of IXS spectra. IXS directly probes the phonon energy at a selected point in reciprocal space and the data treatment is more simple. The derivation of the X-VDOS from powder IXS spectra is discussed in Section 5.8.

5.1 Diffraction geometry

The geometry of a diffuse x-ray scattering experiment is sketched in Fig. 5.1. The primary beam is absorbed by a beam stop and the scattering intensity is detected in transmission geometry. The accessible section of reciprocal space for a given crystal orientation lies on the Ewald sphere. The wave vector $\boldsymbol{k}_i$ of the incoming monochromatic X-rays with modulus $|\boldsymbol{k}_i| = 2\pi/\lambda$ hits the origin (0 0 0) of the reciprocal lattice. In an elastic scattering process all Bragg reflections with positions on the Ewald sphere with radius $2\pi/\lambda$ become visible. The energy uncertainty ΔE of the incoming X-rays results in a thickness of the Ewald sphere $\Delta\boldsymbol{k}$. A geometrical consideration yields $\Delta E/E = \Delta\boldsymbol{k}/\boldsymbol{k}$. The flat area detector records the projection of the Ewald sphere. Fig. 5.2 shows the projection for β-tin for the experimental configuration typically used in this work ($\lambda = 0.7$ Å and sample-detector distance $D = 200$ mm) as well as a configuration at much shorter wavelength ($\lambda = 0.1$ Å). The distortion needs to be taken into account during the reconstruction. For short wavelengths the radius of the Ewald sphere becomes

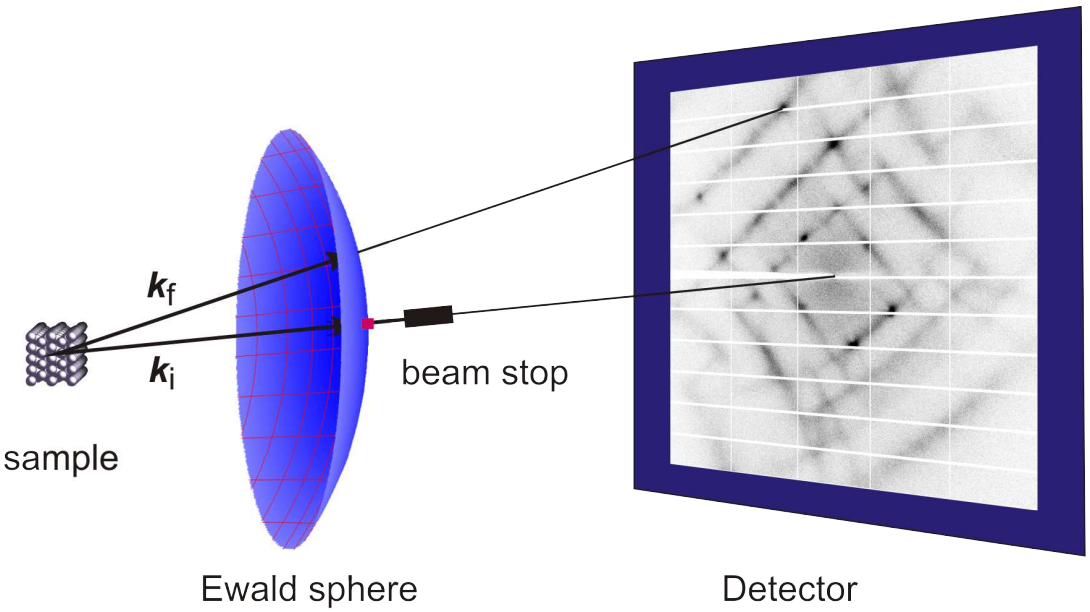

Figure 5.1: Diffraction geometry for a diffuse scattering experiment in transmission. The incoming X-rays with wave vector $\boldsymbol{k}_i$ are scattered by the sample and diffracted onto the Ewald sphere. The red point indicates the origin (0 0 0) of the reciprocal lattice. The direct beam is blocked by a beam stop behind the sample. The flat area detector records the projection of the Ewald sphere. See text for further details.

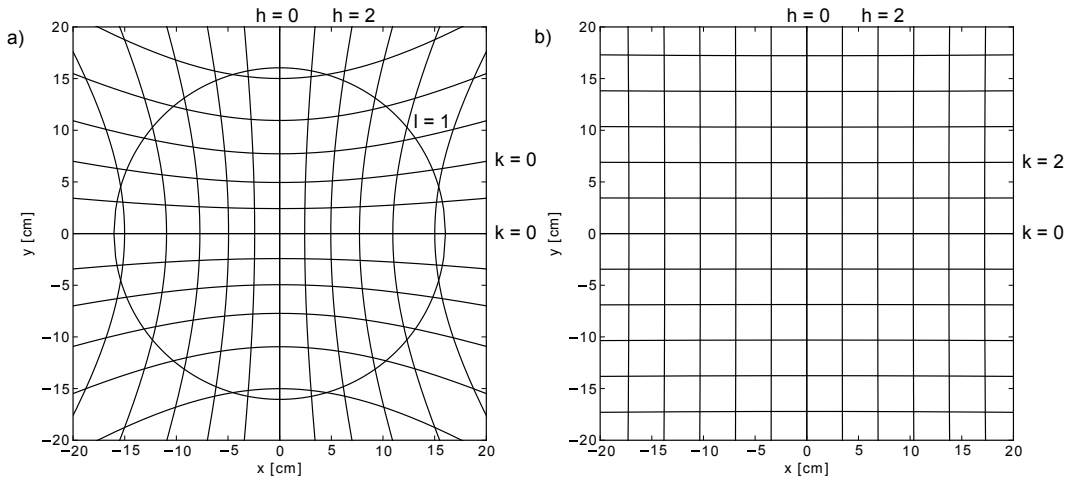

Figure 5.2: Projection of the Ewald sphere for β-tin crystal with the c-axis parallel to the incoming X-rays and the a-axis in the horizontal plane for two different experimental configurations: a) $\lambda = 0.700$ Å) and sample-detector distance $D = 200$ mm b) $\lambda = 0.1$ Å and $D = 2000$ mm. The lines represent constant Miller indices.

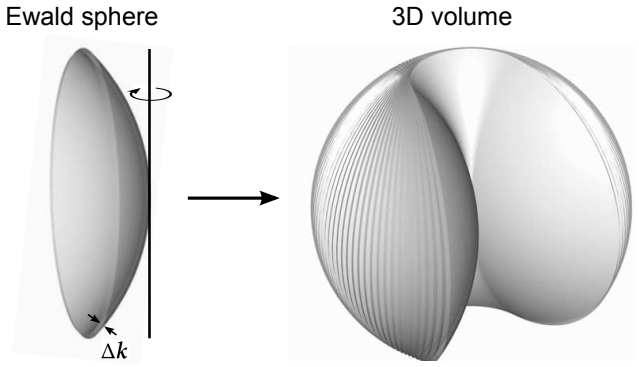

Figure 5.3: Left panel: Part of the Ewald sphere with momentum transfer uncertainty $\Delta \boldsymbol{k}$ collected for a given crystal orientation. Right panel: Rotation of the crystal around an axis perpendicular to the incoming X-rays and collecting diffraction patterns with small angular steps gradually fills up a large volume in reciprocal space.

so large that the diffraction pattern appears to be almost undistorted over a few Brillouin zones (see Gibaud et al. (1997) for further discussion). The projection equations are discussed in Section 5.5. A large volume in reciprocal space can be filled up by rotating the crystal around an axis perpendicular to the incoming X-rays and collecting diffraction patterns in small angular steps (see Fig. 5.3). The projection formula for a standard kappa diffractometer were subject of a separate PhD thesis (Meyer, 1998) and are summarised in Section 5.5.

5.2 Planar projection and parallax

Planar projection of the scattered X-rays to a 2D detector requires a geometrical correction factor D for the solid angle conversion,

$$D = \frac{1}{cos^3(2\theta)}. \tag{5.1}$$

This correction factor can be applied on each pixel or directly on the reconstructed volume.

The parallax effect leads to a smooth distortion of an image caused by the absorption properties of the sensor array. Pixel detectors are usually made of thick Silicon sensors and suffer thus from parallax. The geometry and x-ray absorption properties of the sensor as well as the energy and the spatial distribution of the X-ray beam need to be considered. The correction is generally detector specific; an algorithm for the PILATUS detector is described elsewhere (Hülsen et al., 2005).

5.3 Lorentz and Polarisation correction

The rotation of a crystal exposed to a monochromatic x-ray beam results in a geometrical influence on the exposure time for an arbitrary point in reciprocal space. Reciprocal space points with large absolute momentum transfer move out of the scattering geometry faster than points with small momentum transfer. The so called Lorentz correction (Buerger and Klein, 1945) accounts for this effect. The measured intensity has to be divided pixel-wise by the Lorentz factor (He, 2008)

$$L = \frac{1}{4sin^2\theta cos\theta}, \tag{5.2}$$

where θ denotes the scattering angle. Equation 5.2 holds for point like objects (Bragg peaks). The Lorentz correction is required for sharp features like Bragg reflection. The TDS intensity distributions is much smoother, except for the very proximity of Bragg nodes. The formula for diffuse scattering intensity distribution

of different shape can be found elsewhere (Boysen and Adlhart, 1987). Ideally such corrections should be implemented iteratively. In the following work we did not perform such corrections, as we concentrate on relatively large $\boldsymbol{q}$ values.

The polarisation of the incident beam results in an angular dependence of the scattered intensity. For totally polarised synchrotron radiation the polarisation factor is given by (Holt et al., 2002)

$$P = sin^2(\Phi) + cos^2(\Phi)cos^2(2\theta), \tag{5.3}$$

were Φ is the azimuthal angle between the plane of polarisation of the incident beam and the scattering plane.

5.4 Absorption correction

The absorption is given by the transmission coefficient

$$A = \frac{1}{V}\int_V e^{-\mu p} dV, \tag{5.4}$$

where V the illuminated sample volume, μ is the linear absorption coefficient and p is the total beam path in sample, including the incident and scattered beam path. Different approaches are used to calculate and correct the absorption effect for various sample shapes and geometries (Malsen, 1992). A pixel-wise correction adapted for diffuse scattering experiments with area detector systems is discussed, for example, in Scheidegger et al. (2000); an absorption correction based on a three-dimensional model reconstruction from visual images in Leal et al. (2008).

5.5 3D reconstruction

The reconstruction of 3D intensity distribution from area detector data as illustrated in Figure 5.3 requires the projection of the flat image onto the Ewald sphere and the correction for the above discussed effects. The strategy presented here follows the convention of a standard 4-circle kappa goniometer (Meyer, 1998) with the laboratory reference system illustrated in Figure 5.4. With all diffractometer angles set to zero, the Cartesian reference system is chosen as follows: The ω-axis is parallel to e_3, e_1 is pointing in the direction of the x-ray source and e_2 completes a right-handed orthonormal system. The κ-axis and the ϕ-axis lie in the e_1-e_3 plane, the κ-axis having an angle α to e_3, the ϕ-axis an angle β to e_3. The area detector is mounted on the θ arm of the goniometer. The θ-axis is parallel to the ω-axis, and to e_3. Changing θ rotates the detector about the ω-axis.

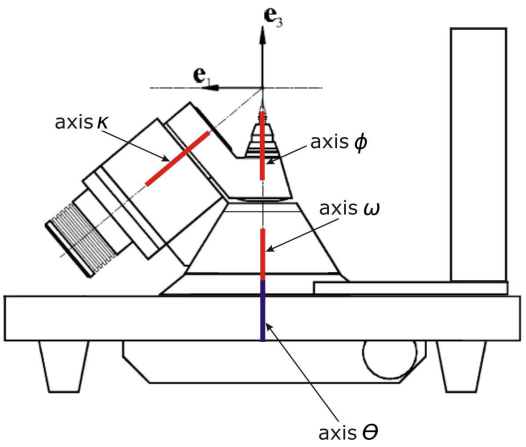

Figure 5.4: Laboratory reference system (bold vectors) of a standard 4-circle kappa diffractometer, adapted from Meyer (1998). The basis vector $\boldsymbol{e}_2$ points towards the reader.

Positive rotations about the e_i axes are defined as follows,

$$\boldsymbol{R(1,\eta)} = \begin{pmatrix} 1 & 0 & 0 \\ 0 & cos(\eta) & sin(\eta) \\ 0 & -sin(\eta) & cos(\eta) \end{pmatrix}, \tag{5.5}$$

$$\boldsymbol{R(2,\eta)} = \begin{pmatrix} cos(\eta) & 0 & -sin(\eta) \\ 0 & 1 & 0 \\ sin(\eta) & 0 & cos(\eta) \end{pmatrix}, \tag{5.6}$$

$$\boldsymbol{R(3,\eta)} = \begin{pmatrix} cos(\eta) & sin(\eta) & 0 \\ -sin(\eta) & cos(\eta) & 0 \\ 0 & 0 & 1 \end{pmatrix}. \tag{5.7}$$

Using the above rotation matrices the position of the primary beam is characterised by two rotations b_2 and b_3,

$$\boldsymbol{s}_0 = \boldsymbol{R}(3, b_3)\boldsymbol{R}(2, b_3) \begin{pmatrix} -1 \\ 0 \\ 0 \end{pmatrix}. \tag{5.8}$$

The diffraction condition is fulfilled for

$$|\boldsymbol{s}| = |\boldsymbol{s}_0| + \boldsymbol{r}, |\boldsymbol{s}| = |\boldsymbol{s}_0|, \tag{5.9}$$

where $\boldsymbol{s}$ is the diffracted beam and $\boldsymbol{r}$ the reciprocal vector in diffraction condition. The reciprocal lattice vector of a crystal mounted on the standard 4-circle kappa

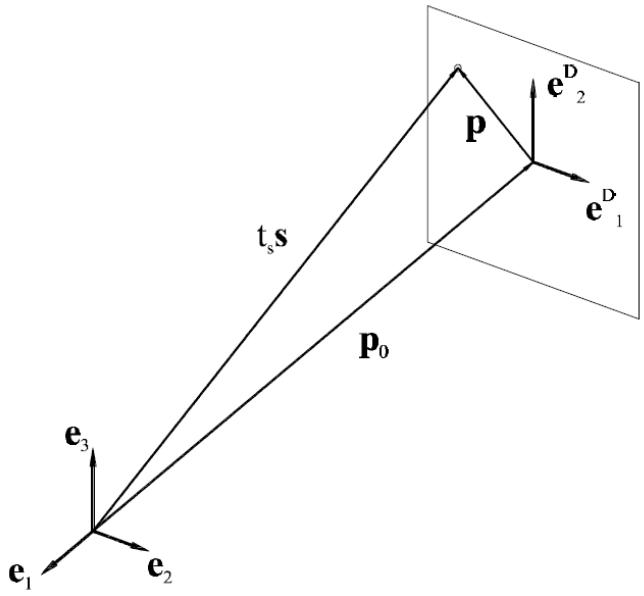

Figure 5.5: Projection of a diffraction vector $\boldsymbol{s}$ onto the flat area detector plane, from Meyer (1998).

diffractometer may be transformed by the goniometer angles ω, κ and ϕ. The transformation is expressed as (Meyer, 1998),

$$\boldsymbol{r} = \boldsymbol{R}\boldsymbol{r}_0 \tag{5.10}$$

with

$$\boldsymbol{R} = \boldsymbol{R}(3,\omega)\boldsymbol{R}(2,\alpha)\boldsymbol{R}(3,\kappa)\boldsymbol{R}(2,-\alpha)\boldsymbol{R}(2,\beta)\boldsymbol{R}(3,\phi)\boldsymbol{R}(2,-\beta). \tag{5.11}$$

The projection used to relate the laboratory reference system to a detector coordinate system $\boldsymbol{e}_1^D$, $\boldsymbol{e}_2^D$ is illustrated in Figure 5.5. Vector $\boldsymbol{p}_0$ connect the origins of the two coordinate systems. The detector coordinate system is given by

$$\boldsymbol{e}_1^D = \boldsymbol{R}(3,\theta)\boldsymbol{R}(3,d_3)\boldsymbol{R}(2,d_2)\boldsymbol{R}(2,d_2)\begin{pmatrix}0\\1\\0\end{pmatrix}, \tag{5.12}$$

$$\boldsymbol{e}_2^D = \boldsymbol{R}(3,\theta)\boldsymbol{R}(3,d_3)\boldsymbol{R}(2,d_2)\boldsymbol{R}(2,d_2)\begin{pmatrix}0\\0\\1\end{pmatrix}, \tag{5.13}$$

where $\boldsymbol{R}(i,d_i)$ are the tilts of the detector around $\boldsymbol{e}_i$ of the laboratory reference system and $\boldsymbol{R}(3,\theta)$ the θ-rotation of the detector. A vector $\boldsymbol{p}$ in the detector plane

is defined as

$$\boldsymbol{p} = x\boldsymbol{e}_1^D + y\boldsymbol{e}_2^D = t_s\boldsymbol{s} - \boldsymbol{p}_0, \tag{5.14}$$

with

$$t_s = -\frac{d}{\boldsymbol{s} \cdot \boldsymbol{e}_1^D \times \boldsymbol{e}_2^D} \tag{5.15}$$

where d denotes the sample detector distance and $\times$ the cross product. For a crystal with reciprocal lattice vectors $\boldsymbol{a}^\star$, $\boldsymbol{b}^\star$ and $\boldsymbol{c}^\star$ and reciprocal lattice angle $\alpha^\star$, $\beta^\star$ and $\gamma^\star$, one may define a orthonormalised crystal based description containing both direct and reciprocal lattice parameters (Busing and Levy, 1967),

$$\boldsymbol{A}_0 = \begin{pmatrix} a^\star & b^\star cos(\gamma^\star) & c^\star cos(\beta^\star) \\ 0 & b^\star sin(\gamma^\star) & -c^\star sin(\beta^\star)cos(\alpha) \\ 0 & 0 & c^{-1} \end{pmatrix}. \tag{5.16}$$

The rotation of the crystal-based reference system with respect to the Cartesian laboratory system is given by

$$\boldsymbol{U} = \boldsymbol{R}(3, c_3)\boldsymbol{R}(2, c_3)\boldsymbol{R}(1, c_1). \tag{5.17}$$

The product $\boldsymbol{U}\boldsymbol{A}_0$ is called orientation matrix. The expression

$$\boldsymbol{r}_0 = \boldsymbol{U}\boldsymbol{A}\boldsymbol{h} \tag{5.18}$$

is finally used to relate the crystal based diffraction vector $\boldsymbol{h}$ to the laboratory system based diffraction vector $\boldsymbol{r}_0$.

Large angular steps of acquired diffraction patterns or large magnification of 3D objects will create gaps between the projections of flat images to the reciprocal space. In order to overcome the problem several interpolation algorithms have been suggested (Campbell et al., 1995, Stanton et al., 1992). For diffuse scattering features any kind of interpolation is a delicate topic due to the large difference in absolute intensities compared to Bragg reflections. For the reconstructions undertaken within this thesis a step-like extrapolation was used to avoid interpolation artefacts. The reconstruction can further be improved by applying the Laue symmetry of the system. Missing volume in reciprocal space can be recovered and the statistics is significantly enhanced (up to 48 times for cubic symmetry).

5.6 Various types of diffuse scattering

Thermal vibrations substantially reduce the intensities of Bragg reflections and distribute the intensity diffusively in reciprocal space as thermal diffuse scattering. There are a number of other effects which contribute to the diffuse scattering in the

study of crystals. These effects can be classified in elastic and inelastic scattering processes, depending whether the photon undergoes a change in energy or not. Different contributions to elastic and inelastic scattering processes are discussed in the following. Apart from TDS there are two other relevant inelastic scattering processes, namely Compton scattering and fluorescence. Other fundamental excitations which can be probed by X-rays are plasmons, excitons and magnons. Their contribution to the total diffuse scattering intensity is, however, negligible in most scattering experiments.

Compton scattering

The scattering process of a photon from a free electron involves energy and momentum transfer. The energy and momentum conservation formulated in the quantum mechanical picture results in a difference between the incident wavelength λ_i and scattered wavelength λ_f

$$\lambda_i - \lambda_f = \frac{h}{m_e c}(1 - cos(2\theta)) = \lambda_C(1 - cos(2\theta)), \tag{5.19}$$

where h is the Planck constant, m_e the electron rest mass and c the speed of light in vacuum. The constant $\frac{h}{m_e c}$ is known as the Compton wavelength of the electron. The difference in wavelength is independent from the incoming energy. The relative change in energy becomes more important for high energy X-rays. In contrast to scattering from a free electron the momentum transfer can be absorbed by the crystal which contains bound electrons. In a typical x-ray scattering experiment the scattering from core electrons will mostly result in elastic processes whereas the scattering from the weakly bound valence electrons contributes most to the Compton scattering.

Fluorescence

The photoelectric effect involves the complete absorption of the incident photon and an emission of an electron. The interaction of X-rays with sufficient high energy can involve the emittance of core electrons. The so created vacancy will be filled by an electron of a higher energy shell emitting a photon of a element specific characteristic wavelength. This fluorescence radiation will contribute to the diffuse scattering. The energy difference between incident and emitted photons can be large enough to be separated by modern pixel detectors (Kraft et al., 2009). The adjustment of the incident X-ray energy away from the characteristic absorption edges further helps to reduce the fluorescence contribution. X-ray absorption spectroscopy on the other hand is a widely used technique in the study of the local electronic structure and correlation, see for example Hippert et al. (2006).

Elastic and quasi-elastic diffuse scattering

Besides the discussed inelastic diffuse scattering processes there are numerous sources for elastic diffuse scattering. In an elastic scattering process there is a well defined phase relation between incident and scattered beam. The elastic scattering processes are coherent, in contrast to the inelastic contribution. Any kind of violation of the crystal symmetry, including static displacements, vacancies, dislocations, fluctuations, incommensurate phases or low-dimensional structures will create diffuse scattering. The study of elastic diffuse scattering is an important tool in the study of local structure and defects and gives access to the pair correlation of atoms on separate sites. An overview of recent advances can be found in Barabash et al. (2009). The contribution of multiple scattering effects to the diffuse scattering is, for example, discussed in Ramsteiner et al. (2009).

Slow dynamical processes give rise to quasi-elastic scattering with energy transfers in the μeV range. It contains both coherent and incoherent components. The coherent component contains information about interference phenomena between atoms, such as lattice distortions or short-range order. Incoherent scattering relates to scattering by individual atoms: if the atoms or molecules undergo stochastic motions (translational or rotational diffusion) during the scattering event, this single-particle scattering is accompanied by an energy transfer. As the motions are not quantised, this results in a broadening of the sharp line arising from elastically scattered X-rays. Quasi-elastic scattering can be resolved by neutron scattering and be used to study diffusion in solids, where an individual particle displaces randomly over the crystal lattice. The line width of the central component can be used to validate diffusion models. See Willis and Carlile (2009) for further details.

5.7 IXS spectra

The intensity of the energy resolved IXS spectra in first order approximation is Equation 2.24 convoluted with the resolution function of the spectrometer,

$$I(\boldsymbol{Q}, E) = A(\boldsymbol{Q})[I_1(\boldsymbol{Q}, E) \otimes R(E)] + B(Q, E), \tag{5.20}$$

where E is the phonon energy, $A(\boldsymbol{Q})$ is an intensity factor taking into account the scattering geometry and the experimental set-up, $\otimes$ denotes the convolution operator, $R(E)$ is the experimental resolution function and $B(Q, E)$ takes into account the background of the electronics and the environment. The background due to the electronics of the IXS spectrometer ID28 at the ESRF is in the order of one count per 30 min and can thus usually be neglected. The phonon excitations can be fitted with Lorentzian functions weighted by the detailed balance factor and convoluted by the experimental resolution function.

5.8 X-VDOS from IXS

The generalised x-ray weighted VDOS (X-VDOS),

$$G(E) = \frac{1}{N} \int d^3\boldsymbol{Q} \sum_j |\sum_n \frac{f_n(\boldsymbol{Q})}{\sqrt{m_n}} e^{i\boldsymbol{Q}\boldsymbol{r}_n - W_n} (\boldsymbol{Q} \cdot \hat{\boldsymbol{e}}_{\boldsymbol{Q},j,n})|^2 \delta[E - E_{\boldsymbol{Q},j)}], \quad (5.21)$$

with momentum transfer $\boldsymbol{Q}$, phonon energy E and eigenvector component $\hat{\boldsymbol{e}}$ of branch j, atomic form factor f, mass m, position vector $\boldsymbol{r}$, Debye Waller factor W of atom n and normalisation factor $N = \sum_n f_n(\boldsymbol{Q})/\sqrt{m_n}$ can be determined from IXS spectra of polycrystalline samples (Bosak and Krisch, 2005). The X-VDOS can be obtained following the standard double-Fourier transformation procedure, described elsewhere (Kohn and Chumakov, 2000). In order to cover scattering contributions from all vibrational states a wide range in momentum transfer space up to large scattering angles must be covered and IXS spectra must be measured up to large energy transfers. The momentum transfer range corresponding to the first Brillouin zone needs to be excluded, since in this case the total momentum transfer Q is equal to the phonon wave vector q , and mainly phonon modes with an eigenvector component parallel to q yield in finite intensity. The thickness of the integration shell needs to be considered as well. The atomic form factor $f(Q)$ has a pronounced Q dependence with an approximately exponential decay. This can be cast into the following form (Cromer and Mann, 1968),

$$f(Q) = \sum_{i=0}^{3} a_i e^{-b_i Q^2} + c. \quad (5.22)$$

This decay is element dependent, and the half-value of f(Q) corresponds roughly to the inverse of the spatial extent of the atom. Measured IXS spectra can be extended to the Anti-Stokes side using the detailed balance law. The elastic contribution must be subtracted using the measured resolution function of the spectrometer. The measured spectra are actually composed of many partial subspectra characterised by different recoil energies. These recoil energies are related to the different scattering angles and the different masses of the atomic species. The data can be processed using a single variable parameter of the mean recoil energy. It can be estimated from the mean scattering angle and the mean atomic mass, and finally adjusted such that a zero X-VDOS is obtained in a chosen energy range. This energy range must correspond to a gap between optical modes or above the highest ones. This choice guarantees a proper elimination of multiphonon contributions from the measured spectra.

Chapter 6

Results

In the following the combination of IXS, TDS and *ab initio* lattice dynamics calculations is presented for several benchmark systems. Characteristic features in the lattice dynamics are localised by the inspection of TDS intensity distributions in 3D reciprocal space. Selected regions in reciprocal space are then selected for an energy resolved measurement employing IXS and compared to scattering intensities calculated *ab initio*. The validated calculation permitts new insights into the lattice dynamics. The approach is illustrated for the silica polymorphs, α-quartz, coesite and α-cristobalite, germanium dioxide in α-quartz structure, the metallic tin polymorphs β- and γ- tin, and for water in its most common crystalline form, ice Ih.

6.1 α-quartz and germanium dioxide in α-quartz structure

The lattice dynamics of α-quartz (α-SiO_2) is revised with the focus on the origin of the first peak in the VDOS and compared to the quartz-like polymorph of germanium dioxide (α-GeO_2). An extensive study combining IXS from single- and polycrystalline samples, 3D mapping of TDS and *ab initio* calculations has been conducted previous to this work for α-quartz (Bosak et al., 2012). An improved calculation reveals that a local saddle point at the L point contribute most to the first peak in the VDOS of α-SiO_2 and α-GeO_2. We show that the critical point found in Bosak et al. (2012) actually contributes to a peak located at slightly higher energy. Our finding is justified by comparing the calculated X-DOS with the one obtained from powder IXS spectra. The comparison of the TDS intensity distribution of the two systems nicely illustrates the similarity of the interaction potential.

Introduction

α-quartz has been the subjects of many studies. Its structure-related properties are of fundamental interest for many technological applications, such as pressure gauges, oscillators, resonators, and wave stabilisers making use of the piezoelectric properties. α-quartz can be described as spirals made up of corner-connected SiO_4-tetrahedra with intrinsic degrees of freedom. The lattice dynamics of quartz has been extensively studied and the phonon dispersion in high-symmetry directions based on inelastic neutron (Dorner et al., 1980, Strauch and Dorner, 1993) and x-ray scattering (Halcoussis, 1997) are documented.

Experimental Details

TDS studies were performed on beamline X06SA at the Swiss Light Source. Monochromatic X-rays with wavelength 0.7 Å were scattered from rod-like 1 mm thick crystals at room temperature in transmission geometry. The sample was rotated with an increment of 0.1° orthogonal to the beam direction over an angular range of 360° while diffuse scattering patterns were recorded in shutterless mode with a PILATUS 6M detector (Kraft et al., 2009). The orientation matrix and geometry of the experiment were refined using the CrysAlis (Oxford diffraction Ltd.) software package. For the final reciprocal space reconstructions corrections for polarisation and for solid angle conversion associated with the planar projection were applied using in-house developed software.

The generalised x-ray weighted VDOS (X-VDOS) was obtained from IXS spectra of a polycrystalline α-quartz sample measured at ID28 in transmission geometry. The scattered radiation was collected by eight crystal analysers. The momentum transfer resolution of each analyser was ≈ 0.3 nm^{-1}. The values of the momentum transfers for each analyser were chosen away from the Debye-Scherrer rings and covered the $[10 : 70]$ nm^{-1} range. The data combine the results of measurements with 1.4 meV resolution at 23.725 keV incident energy within [-25 : +25] meV energy range and 0.2 meV energy steps and results from the measurement with 3.0 meV resolution within [-25 : +180] meV energy range and 0.7 meV steps. The elastic peak in the IXS spectra was subtracted using the instrumental function of each analyser determined by x-ray scattering from a polymethylmethacrylate (PMMA) sample close to the maximum of its structure factor. The X-VDOS was obtained from the summed IXS spectra within the incoherent approximation following the data treatment procedure established by Bosak and Krisch (2005), see Chapter 5 for details.

Single crystal IXS measurements on α-GeO_2 were conducted at ID28 at the ESRF. The spectrometer was operated at 17.794 keV incident energy, providing an energy resolution of 3.0 meV full-width-half-maximum. The momentum resolution

was set to $\approx 0.3\ \mathrm{nm}^{-1} \times 0.8\ \mathrm{nm}^{-1}$ in the horizontal and vertical plane, respectively. IXS scans were performed in transmission geometry along selected directions in reciprocal space.

Calculation

The lattice dynamics calculation was performed using the DFPT approach (Gonze and Lee, 1997) as implemented in the CASTEP code (Clark et al., 2005, Refson et al., 2006). Local density approximation within the plane-wave formalism was employed using the norm conserving pseudopotentials from (Refson et al., 2006) for silicon and oxygen. The pseudopotential for Germanium was created within the same approximations and algorithm used for silicon. The plane wave cut-off and the sampling of the electronic grid were carefully tested by evaluating the convergence of internal forces. The electronic structure was computed on a $5 \times 5 \times 4$ Monkhorst-Pack grid and the plane wave cut-off was set to 780 eV for both systems. A full geometry optimisation was performed employing the Broyden-Fletcher-Goldfarb-Shannon method (Pfrommer et al., 1997), varying lattice and internal parameters. Phonon frequencies and eigenvectors were computed on a $5 \times 5 \times 4$ Monkhorst-Pack grid of the irreducible part of the Brillouin zone by perturbation calculations. The acoustic sum rule as well as the charge neutrality at the level of Born effective charges were imposed. A Fourier interpolation with a grid spacing of 0.005 $\mathrm{Å}^{-1}$ in the cumulant scheme including all image force constants was applied for the VDOS. The calculation was tested to be well converged with a maximum error in phonon energies of < 0.05 meV. TDS and IXS intensities were calculated from the phonon eigenvectors and frequencies within the validity of both the harmonic and adiabatic approximation using in house developed software (Mirone and Wehinger, 2012). The scattering intensities were calculated in first order approximation.

Results

The X-VDOS for α-quartz is shown in Figure 6.1 a) and compared to the calculation. The calculated real VDOS of α-quartz and α-GeO_2 are depicted in Figure 6.1 b) and c). The X-VDOS was used for the determination of an overall energy scaling factor. It turns out that an overall stretching of 4 % leads to a good agreement of experimental and theoretical X-VDOS with exception of the high energy optical modes. Discrepancies between experiment and theory are mostly due to the limited accuracy of sampling the reciprocal space with powder IXS spectra. The underestimation of the calculated energies can be attributed to the limited accuracy of the exchange correlation function within the local density approximation; see Refson et al. (2006) for a detailed discussion.

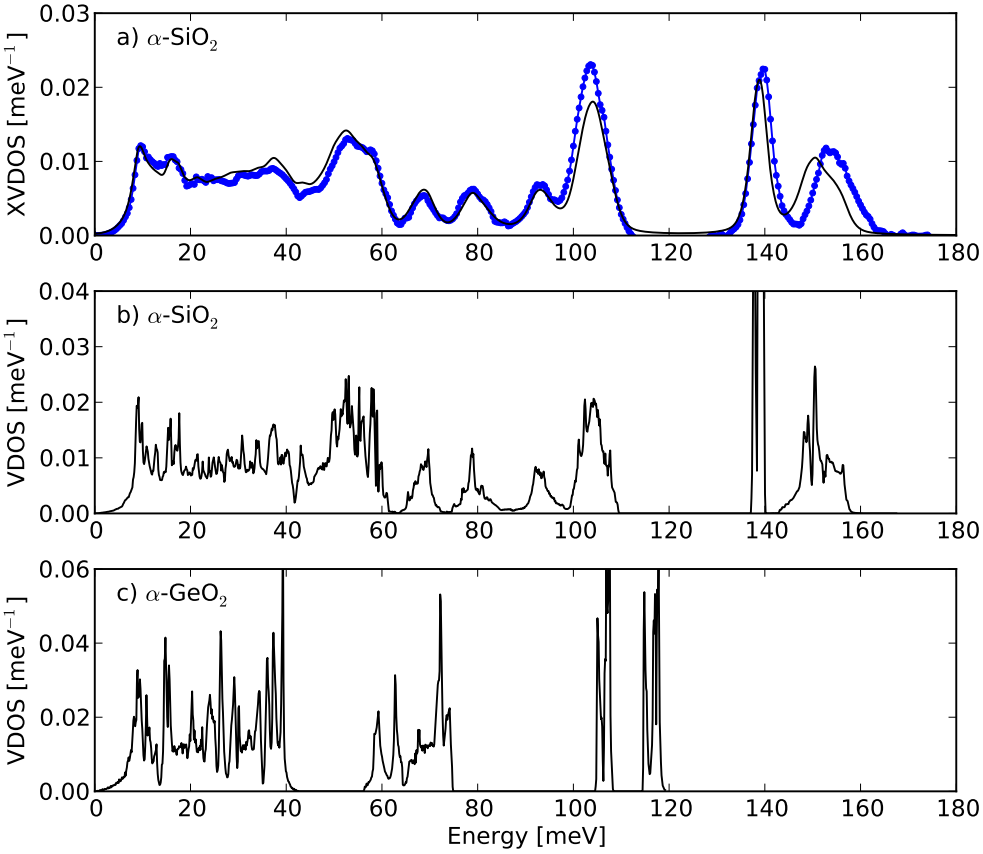

Figure 6.1: a) Experimental (blue points) and theoretical (black line) X-VDOS of α-quartz. The energies of the theoretical data were scaled by 1.04 and convoluted by the experimental resolution. b) Calculated VDOS of α-quartz with applied energy scaling. c) Calculated VDOS of α-GeO_2.

Peaks in the VDOS require critical points in the phonon dispersion relations for which the gradient in all crystallographic directions becomes zero (Van Hove, 1953). In fact the VDOS $g(E)$ can be written in an alternative description (Landau and Lifshitz, 1980, Van Hove, 1953),

$$g(E) = \frac{v_0}{Zl} \sum \int \frac{df_{\boldsymbol{q}}}{|\nabla_{\boldsymbol{q}} E(\boldsymbol{q})|}, \tag{6.1}$$

where v_0 is the unit cell volume with Z atoms in l dimensions, $\nabla_{\boldsymbol{q}} E(\boldsymbol{q})$ is along the normal to the constant-energy surface through a point in $\mathbf{q}$ space, $df_{\boldsymbol{q}}$ is the constant-energy surface element and the sum runs over all vibrational modes. In a three dimensional crystal the VDOS shows a logarithmic singularity for $|\nabla_{\boldsymbol{q}} E(\boldsymbol{q})|$ at $E = E_0$ at some $\boldsymbol{q}$ which lies on a constant-energy surface. Such a singularity leading to divergence in the VDOS may actually exist under certain conditions in monoatomic body-centred cubic crystals (Gilat, 1967). If $|\nabla_{\mathbf{q}} E(\boldsymbol{q})|$ occurs at some point which does not lie on a constant energy surface (ordinary singular critical point) it results at most in finite singularities for $|\frac{\partial^2 E(\boldsymbol{q})}{\partial q_\alpha \partial q_\beta}| \neq 0$, where α and β denote the directions of q. The vanishing of the second order determinant is not required by symmetry and occurs only for special relations of the forces between the atoms. The accidental occurrence, however, would lead to higher singularities by a continuous family of critical points. For an ordinary singular critical point the frequency surface can be expanded to second order to

$$E - E_0 = \sum_{\alpha=1}^{l} a_\alpha \xi^2, \boldsymbol{\xi} = \boldsymbol{q} - \boldsymbol{q_0}, a \in \Re. \tag{6.2}$$

In the case of a three dimensional crystal four types of critical points (minimum, maximum, two different saddle points) can occur, leading to square root singularities with analytic expressions (Van Hove, 1953). Only the saddle points can produce a peak in the VDOS. For a slightly extended neighbourhood the series can be expanded,

$$E - E_0 = \sum_{\alpha=1}^{l} a_\alpha \xi^2 + b_\alpha \xi^4 + ... \tag{6.3}$$

Numerical integration of Eq. 6.1 including the second terms in the expansion shows that also local minima and maxima can lead to a peak like singularity, if at least one $|b_\alpha| >> |a_\alpha|$. In the case of coesite (see Section 6.2) the extended expansion is of relevance.

In order to localise the critical points contributing most to the first peak in the low energy part of the VDOS, two filters were applied simultaneously. An energy filter of ΔE= 0.3 meV was applied to the *ab initio* calculated phonon energies of

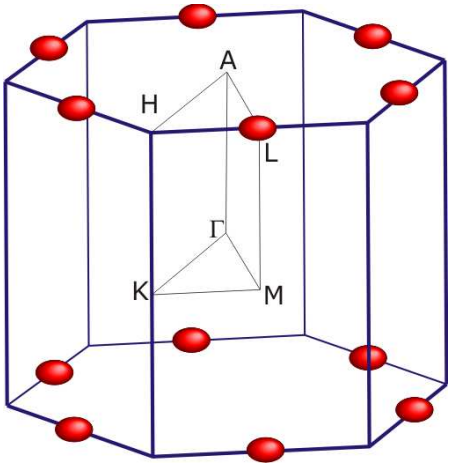

Figure 6.2: Brillouin zone of the quartz structure and localisation of the critical point contributing most to the first peak in the VDOS of α-SiO_2 and α-GeO_2.

the first Brillouin zone and $1/|\nabla_{\boldsymbol{q}} E(\boldsymbol{q})|$ was computed within this energy window. A saddle point at L point (see Figure 6.2) was found to contribute most to the first peak in the VDOS at 9.1 meV in the case of α-SiO_2 and 8.9 meV in the case of α-GeO_2. The saddle point at (1/4 0 1/2) found in (Bosak et al., 2012) creates the second peak in the VDOS of α-quartz located at 9.8 meV. The accuracy of the pseudo-potentials used in the current calculation is improved in respect to the standard potentials used in Bosak et al. (2012). Furthermore we used the cell geometry as predicted by the calculation whereas the lattice parameters previously where fixed to the experimental ones.

Reconstructed high symmetry reciprocal space sections of TDS intensity distributions from experiment are shown in Figure 6.3a) - c). We note a complex distribution of diffuse features. A quite uniform background is visible which arises mainly from air scattering. Decisive conclusions for the origin of the features in the rather complex α-quartz structure can be obtained by the lattice dynamics calculation. *Ab initio* calculated TDS intensity distributions for the same reciprocal space sections are shown in Figure 6.3d) - e). We note that all features of TDS are well described by the calculation. The strong features in the TDS intensity distribution are dominated by the low energy part of the lattice dynamics, as the intensity is proportional to ω^2 in the long wavelength limit. This includes that this part of the lattice dynamics must be well described by the calculation. The diffuse scattering along Γ - A was further investigated by IXS in the proximity of the (0 0 3) reflection. An IXS intensity map composed of 6 measured spectra is shown in Figure 6.4 together with the intensity map calculated *ab initio*. The comparison show that the diffuse scattering is almost exclusively of inelastic nature. Both

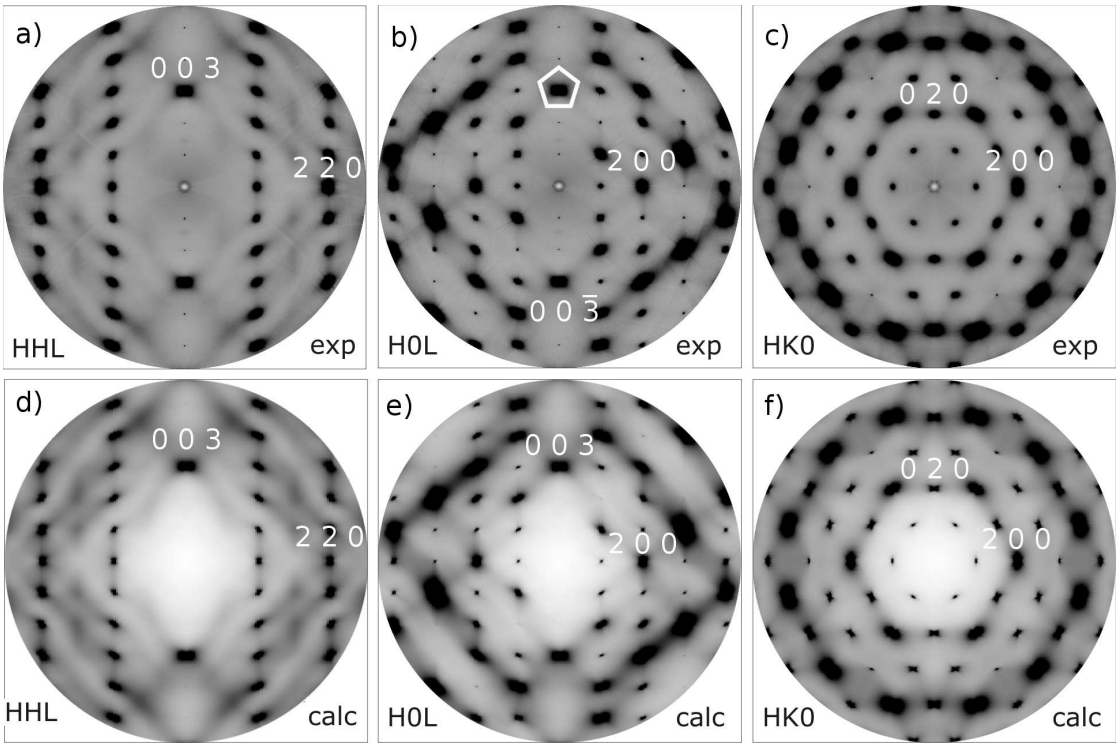

Figure 6.3: Experimental (a) - (c) and calculated (d) - (f) TDS intensity distribution of α-GeO_2 in the indicated reciprocal space sections. The diffuse scattering along Γ - A near the (0 0 3) reflection (marked by a polygon in b) is investigated by IXS.

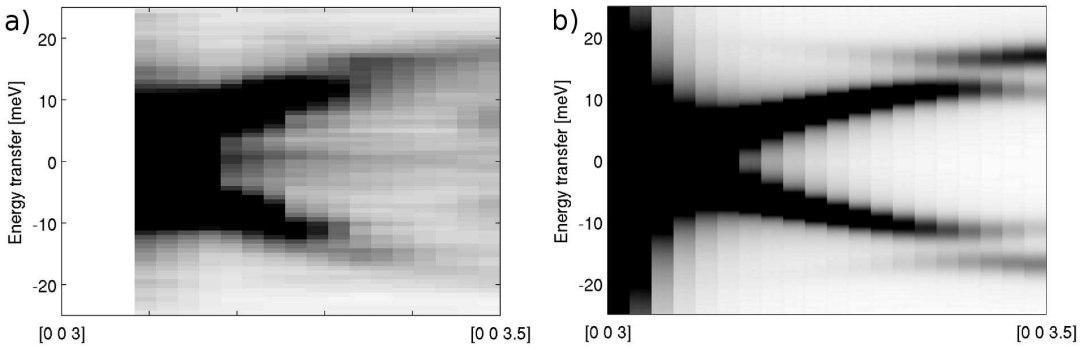

Figure 6.4: Experimental (a) and *ab initio* calculated (b) IXS intensity map of α-GeO_2 along Γ - A. The experimental map consists of six spectra with a q-spacing of 0.083 nm^{-1} measured with an energy spacing of 0.7 meV. These spectra are linearly interpolated to 18 q-points and 72 energy steps. The calculated IXS map was computed on 20 q-points and the intensity convoluted with the experimental resolution function.

energies and intensities are in good agreement with the calculation.

Diffuse scattering intensity distributions of α-GeO_2 and α-SiO_2 are compared in Figure 6.5. Both systems show very similar strong diffuse features, mirroring the similarity of the electronic structure and the interaction potential. Despite the similarity there are also distinct differences in the lattice dynamics. Remarkably, the isolated diffuse line propagating along [001] observed in α-SiO_2 is not visible in α-GeO_2. This feature was shown to originate from the transverse acoustic phonon in purely longitudinal geometry (Bosak et al., 2012).

Conclusions

In summery we have shown that the improved *ab initio* calculation of α-quartz describes the VDOS remarkably well after a small linear scaling of the calculated phonon energies, except for the highest energy optical phonons. The *ab initio* lattice dynamics calculation of α-GeO_2 was validated for the low energy part by comparing IXS spectra and TDS intensity distributions with the calculation. While distinct lattice dynamics features in terms of a simultaneous retrieval of phonon energy and momentum are not directly extractable from experiment, it was possible to get access to these features with help of the calculation. A saddle point at L was found to contribute most to the first peak in the VDOS of α-quartz and germanium dioxide in α-quartz structure. The strong resemblance of TDS intensity distributions for the two systems nicely illustrates the similarity of the interaction potential.

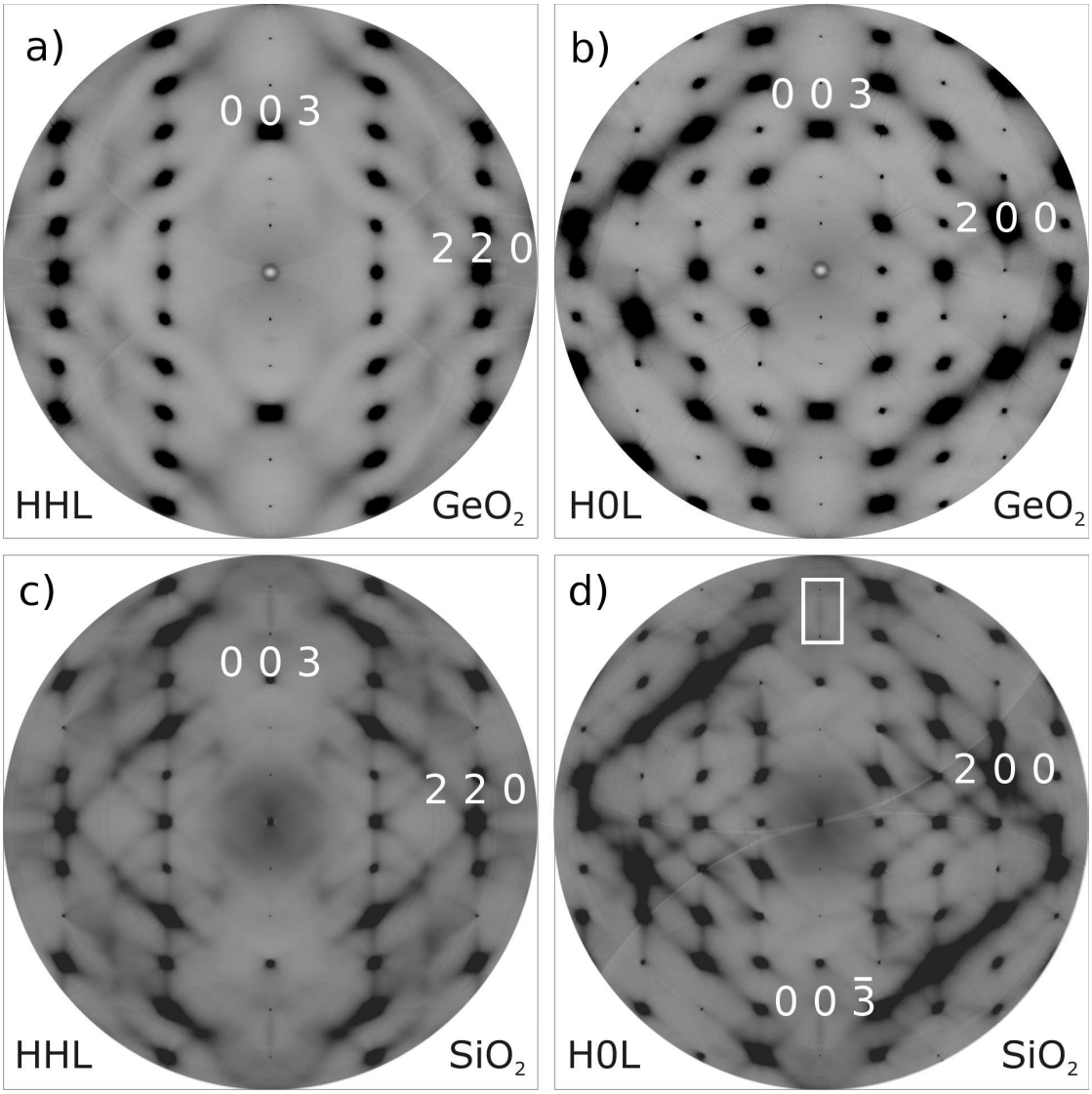

Figure 6.5: Diffuse scattering intensity distribution in the indicated reciprocal space section of α-GeO_2 (a) and (b) and α-SiO_2 (c) and (d). An isolated diffuse line propagating along [001] is highlighted by a square in (d).

6.2 Coesite

The lattice dynamics of coesite has been studied by a combination of diffuse x-ray scattering, inelastic x-ray scattering and an *ab initio* lattice dynamics calculation. The combined technique gives access to the full lattice dynamics and thus eventually provides detailed information on the elastic properties, the stability and metastability of crystalline systems. The experimentally validated calculation was used for the investigation of eigenvectors, mode character and their influence on the density of vibrational states. The low-energy vibrational properties are investigated for similarities and distinct differences and compared to the most abundant silica polymorph α-quartz. The synthesis of the high quality crystal and the details of the measurement are given in Experimental methods. The lattice dynamics calculation is described in section Calculation. Experimental and theoretical results are presented and discussed in Results and Discussion.

Introduction

Coesite, SiO_2, is the highest density tetrahedrally coordinated crystalline polymorph of silica with space group C 1 2/c 1 (Gibbs et al., 2003). It was first synthesised in 1953 at 3.5 GPa and 750 °C (Coes, 1953) and later found in sandstone of the Arizona Barringer crater (Chao et al., 1960) and led to the general acceptance of the impact cratering theory and to important implications for the recognition of meteorite impact craters in quartz-bearing geologic formations (Mark, 1995). The discovery of coesite revolutionised the whole meteorite study and the analysis of impact products. It was also shown that being encapsulated in diamond formed in deep Earth's interior, coesite allows the unambiguous identification of 'fossilised' high pressure states in individual inclusions of mantle samples delivered to the Earth's surface in the course of various geological processes (Sobolev et al., 2000). The fossilised pressure phases of the inclusion and the thermoelasticity of the host-inclusion (diamond-coesite) ensemble may provide a highly accurate geobarometer (Sobolev et al., 2000). Elastic and dynamical properties of coesite have been intensively studied in the past. Elastic constants for instance were examined using Brillouin light scattering (Weidner and Carleton, 1977) and *ab initio* calculations (Kimizuka et al., 2008); vibrational properties at zero momentum transfer were measured by Raman (Liu et al., 1997, Sharma et al., 1981) and infrared spectroscopy (Lippincott et al., 1958, Williams et al., 2000). The compression mechanism was studied by single crystal x-ray diffraction (Angel et al., 2003, Levien and Prewitt, 1981) and *ab initio* calculations (Kimizuka et al., 2008). The investigation of silica under pressures lead to the discovery of unexpected phenomena, such as, for example, the formation of mesoporous coesite at a pressure of 12 GPa and a temperature of 300 °C (Mohanty et al., 2009, 2010). Currently, the

study of the phonon dispersion relations is limited to numerical calculations using potential based methods (Dean et al., 2000). Experimental studies of dispersion relations have not been presented yet. The knowledge of the full lattice dynamics is, however, fundamental for the understanding of the compression mechanism and phase transitions. In particular the origin of the first peak of the density of vibrational states (VDOS) is of interest regarding the origin of the Boson peak in silica glass. As suggested in Chumakov et al. (2011) the Boson peak in glasses originates from the acoustic phonon branches near the boundary of the pseudo-Brillouin-zone and has its counterpart in the VDOS of the corresponding crystal.

In the following we report the results of the powerful combination of diffuse scattering and inelastic x-ray scattering (IXS) for the study of distinct lattice dynamical features in a twinned crystal and the validation of the DFPT calculation. The combined approach allows understanding the lattice dynamics at arbitrary momentum transfers over the entire energy range and thus delivers a complete picture of the vibrational properties. The validated calculation is used for the study of particularities in the dispersion relations and contributions of different modes to the VDOS.

Experimental details

A polycrystalline sample of coesite was synthesised by Leonid Dubrovinsky (Bayerisches Geoinstitut, Universität Bayreuth, Universitätsstraße 30, D-95440 Bayreuth, Germany) and Natalia Dubrovinskaia (Material Physics and Technology at Extreme Conditions, Laboratory of Crystallography, University of Bayreuth, D-95440 Bayreuth, Germany) using the high pressure high temperature technique at P = 5.5 GPa and T = 1000 °C. A 1000-ton hydraulic press (Voggenreiter GmbH) with a toroidal-type high-pressure cell (Khvostantsev et al., 1977) was employed. The size of the synthesised sample was of about 50-70 mm^3 of pure coesite. As a starting material compacted amorphous silica (Sigma Aldrich, 99.9 % purity) was used. The cross-section of the sample container just after the synthesis is shown in Figure 6.6.

The single crystals were grown by Vadim Brazhkin and Tatiana Dyuzheva (Institute for High Pressure Physics RAS, 142190 Troitsk Moscow region, Russia) employing the hydrothermal method described elsewhere (Dyuzheva et al., 1998). X-ray diffuse scattering experiment was conducted on beamline ID29 (de Sanctis et al., 2012) at the European Synchrotron Radiation Facility (ESRF). Monochromatic X-rays with wavelength 0.7 Å were scattered from an elongated ($\approx 0.1 \times 0.3$ mm^2) coesite crystal at room temperature in transmission geometry. The sample was rotated with an increment of 0.1° orthogonal to the beam direction over an angular range of 360° while diffuse scattering patterns were recorded in shutterless mode with a PILATUS 6M detector (Kraft et al., 2009). The orientation matrix

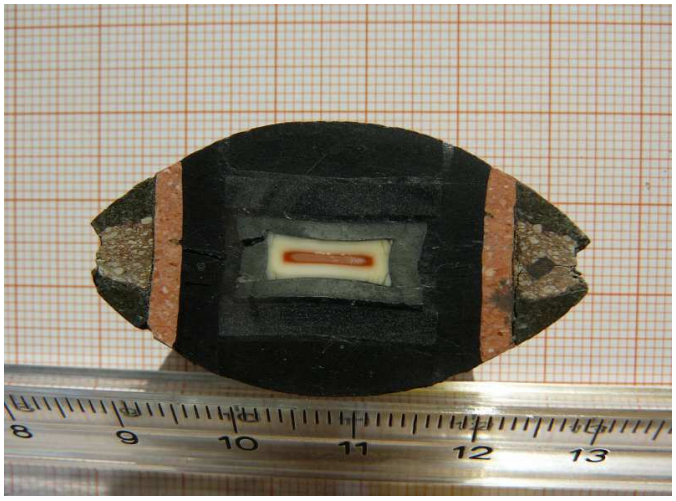

Figure 6.6: Cross-section of the pressure pellet containing a polycrystalline sample of coesite synthesised at P= 5.5 GPa and T=1000 °C.

and geometry of the experiment were refined using the CrysAlis (Oxford diffraction Ltd.) software package. The sample was found to be twinned in the *ac* plane. The single crystal IXS study was carried out on beamline ID28 at the ESRF. The spectrometer was operated at 17.794 keV incident energy, providing an energy resolution of 3.0 meV full-width-half-maximum with a beam focus of 30 × 60 μm full-width-half-maximum. IXS scans were performed in transmission geometry along selected directions in reciprocal space. Further details of the experimental set-up and the data treatment can be found in Chapter 4 and 5.

The generalised x-ray weighted VDOS (X-VDOS) was obtained from IXS spectra of a polycrystalline sample measured at ID28. The scattered radiation was collected by nine crystal analysers. The momentum transfer resolution of each analyser was ≈ 0.3 nm^{-1}. The values of the momentum transfers for each analyser were chosen away from the Debye-Scherrer rings and covered the [10 : 70] nm^{-1} range. The data combine the results of measurements with 1.4 meV resolution at 23.725 keV incident energy within [-25 : +25] meV energy range and 0.2 meV energy steps and results from the measurement with 3.0 meV resolution within [-25 : +180] meV energy range and 0.7 meV steps. The elastic peak in the IXS spectra was subtracted using the instrumental function of each analyser determined by x-ray scattering from a polymethylmethacrylate (PMMA) sample close to the maximum of its structure factor. The X-VDOS was obtained from the summed IXS spectra within the incoherent approximation.

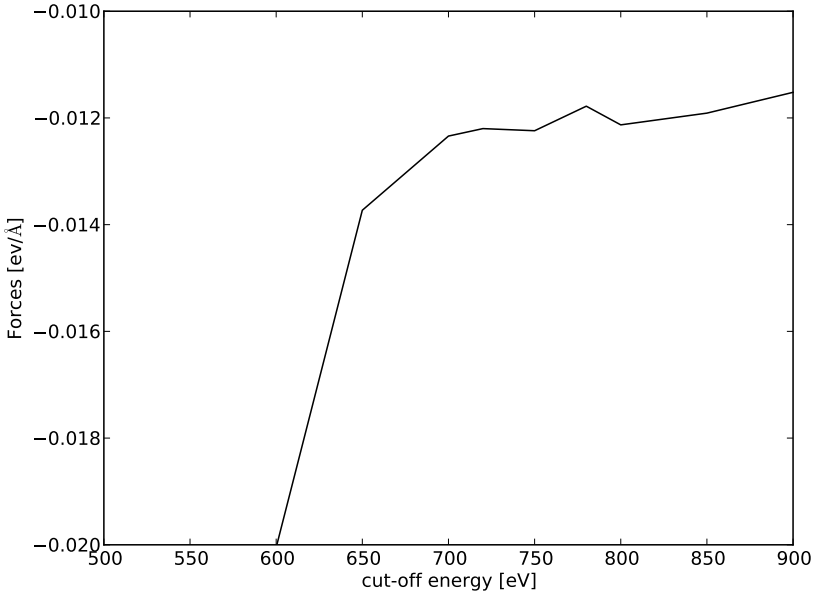

Figure 6.7: x component of the symmetrised force on an oxygen atom as function of the plane wave cut-off. The force is converged to 1.5×10^{-4}eV/Å at 800 eV.

Calculation

The lattice dynamics calculation was performed using the DFPT approach (Gonze and Lee, 1997) as implemented in the CASTEP code (Clark et al., 2005, Refson et al., 2006). See Chapter 3 for further details. The local density approximation within the plane-wave pseudopotential formalism was employed using norm conserving pseudopotentials. The pseudopotentials were taken from the DFPT calculation of α-quartz (Refson et al., 2006). The atomic configuration of oxygen and silicon atoms in coesite are the same as in α- quartz and the bond lengths are very similar. The plane wave cut-off and the sampling of the electronic grid were carefully tested by evaluating the convergence of internal forces. The convergence of the plane wave cut-off is shown in Figure 6.7.

The plane wave cut-off was set to 800 eV and the electronic structure was computed using a 3×3×2 Monkhorst-Pack grid (Monkhorst and Pack, 1976). A full geometry optimisation was performed employing the Broyden-Fletcher-Goldfarb-Shannon method (Pfrommer et al., 1997), varying lattice and internal parameters. The cell parameters of the optimised cell are compared to the experimental values (Smyth et al., 1987) from single-crystal neutron and x-ray diffraction in Table 6.1. They agree within 1.6 %.

Table 6.1: Cell parameters of SiO_2 coesite from calculation and experiment (Smyth et al., 1987).

Calculation	Experiment
a = 7.137 Å	a = 7.136 Å
b = 12.295 Å	b = 12.384 Å
c = 7.072 Å	c = 7.186 Å
$\alpha = \gamma = 90°$	$\alpha = \gamma = 90°$
$\beta = 120.374°$	$\beta = 120.375°$

Phonon frequencies and eigenvectors were computed on a $4 \times 4 \times 3$ Monkhorst-Pack grid of the irreducible part of the Brillouin zone by a perturbation calculation and further Fourier interpolated for the VDOS and dispersion relations. The calculated phonon energies were tested to be converged to < 0.05 meV. TDS and IXS intensities were calculated from the phonon eigenvectors and frequencies following the formalism discussed in Chapter 2 in assumption of the validity of both the harmonic and adiabatic approximation using in house developed software (Mirone and Wehinger, 2012). The scattering intensities were calculated in first order approximation. See Chapter 2 for a detailed discussion.

Results and discussion

High symmetry reciprocal space sections of diffuse scattering as obtained from experiment and corresponding calculated TDS intensity distributions are shown in Figure 6.8.

Corrections for polarisation and projection (He, 2008) and the Laue symmetry of the system were applied. A complex intensity distribution is noticeable. Intense features indicated in Figure 6.8 were selected for a detailed IXS measurement in order to distinguish between possible elastic and inelastic contributions and to resolve the energies of the phonons contributing most to the TDS. A remarkable consistence between the experimental and calculated patterns can be seen for instance from the shape of indicated features. The twinning is mostly visible in the third column of Figure 6.8. The number of Bragg reflections can only be described by a combination of two domains. The HK0 plane is common. The structure could be solved for a twinning of 180° around the reciprocal lattice axis a* with an intensity contribution from 25% of the smaller crystal. The corresponding calculated TDS in the second row was created by the weighted superposition of the indicated intensity distributions. Experimental artefacts due to non-uniform absorption - arising from the anisotropic shape of the sample - are visible.

Figure 6.9 shows two representative IXS spectra. One can clearly note the

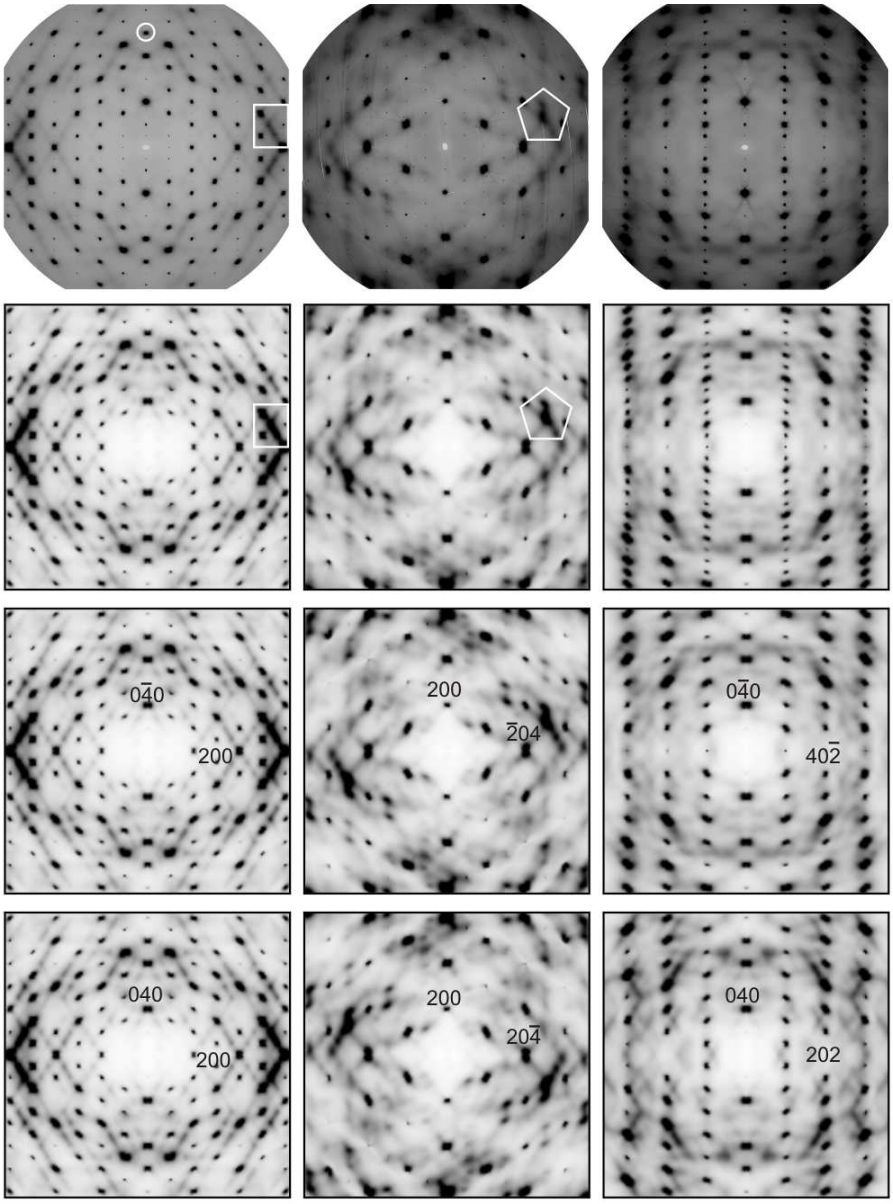

Figure 6.8: Experimental (first row) and calculated (second row) diffuse scattering intensity distributions of coesite in high-symmetry reciprocal space sections. The absolute intensity is scaled to the best visualisation of the diffuse features. The calculated intensity distributions in the second row are created by the weighted superposition of the two crystalline orientations shown in the third and fourth row. The diffuse features marked by a circle and a polygon were selected for an IXS study, the intense features highlighted by a rectangle and a polygon are guides for the comparison of experimental and calculated diffuse scattering. See text for further details.

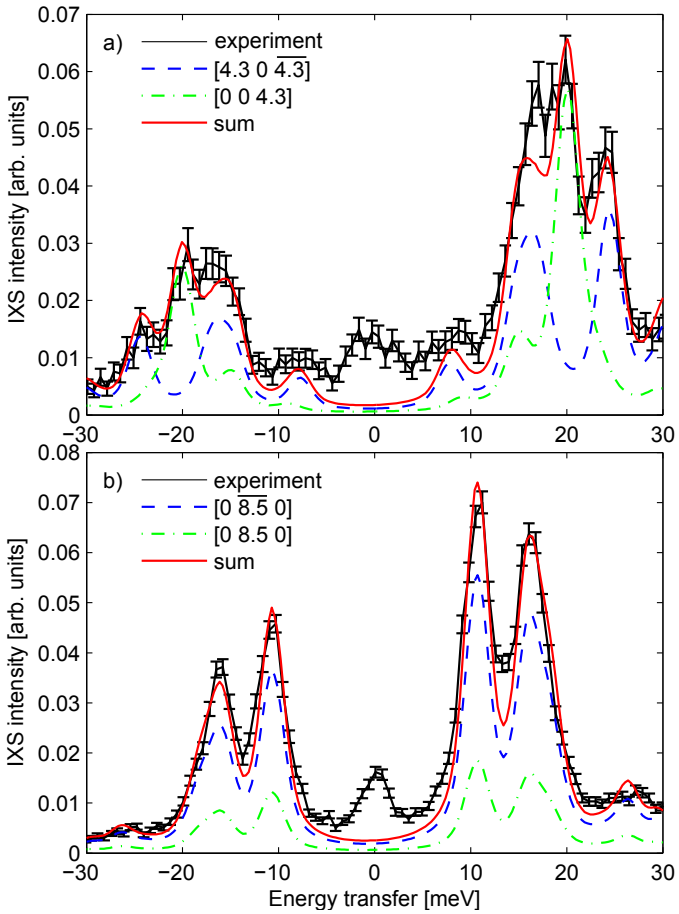

Figure 6.9: Experimental (black points with error bars) and theoretical (red line) IXS spectra from coesite crystal. The theoretical spectra are the weighted sum of the two crystalline orientations: domain 1 - 75% (blue dashed line), domain 2 - 25% (green dotted dashed line). Theoretical intensities were convoluted with the experimental resolution function and the energy transfer was scaled by 1.045.

influence of the two crystalline domains on the inelastic spectra in Figure 6.9 a). The spectra of the two domains belong to different Q-values with different phonon eigenvectors and energies and are thus different. The calculated spectra of the two domains in the common plane 6.9 b) are, except for the overall intensity, identical. The experimental spectra also show a small elastic line. After scaling the calculated energies by 1.045 the theoretical spectra describe quite well both position and intensity of the phonons. The scaling factor was determined from the VDOS, and its value is justified further below.

Figure 6.10 shows the IXS intensity maps along the indicated directions from calculation and measurement. The experimental spectra show that the diffuse scattering is of almost exclusively inelastic nature. Taking into account the intensity contribution of the two crystalline domains, both, energy transfer and inelastic intensities of the different phonon branches are well described by the calculation for arbitrary directions. This implies that the theory correctly predicts both eigenvalues and eigenvectors at arbitrary momentum transfers.

The generalised x-ray weighted VDOS (X-VDOS) (see Section 5.8 for coesite is shown in Figure 6.11 a). The X-VDOS was used for the determination of an overall energy scaling factor. In fact the VDOS probes the energy of the ensemble of states in three dimensional reciprocal space and is therefore most appropriate for the determination of the scaling factor. It turns out that an overall stretching of 1.045 leads to a good agreement of experimental and theoretical X-VDOS. Discrepancies between experiment and theory are mostly due to the limited accuracy of sampling the reciprocal space with powder IXS spectra. The underestimation of the calculated energies can be attributed to the limited accuracy of the exchange correlation function within the local density approximation; see Refson et al. (2006) for a detailed discussion. The partial density of states (Figure 6.11 b and c)) separate the contribution of silicon and oxygen atoms. Looking at the low energy part of the partial VDOS (Figure 6.11 e)) we find that the first peak located at 10.1 meV has equal contributions from silicon and oxygen atoms. The main peak of the scattering function at 14.4 meV is, however, dominated by the vibration of the oxygen atoms. The low energy VDOS of α-quartz is plotted in Figure 6.11 f) for comparison. The α-quartz calculation was performed using the same pseudopotentials and similar parameters as for coesite. For a detailed discussion on the calculation see Refson et al. (2006). Here, the first peak dominates the low energy part of the VDOS. It arises as in coesite from equal contributions from silicon and oxygen atoms.

In order to localise the critical points contributing most to the first and the main peak in the low energy part of the VDOS, two filters were applied simultaneously. An energy filter of $\Delta E = 0.3$ meV was applied to the *ab initio* calculated phonon eigenfrequencies of the first Brillouin zone and $1/|\nabla_{\boldsymbol{q}} E(\boldsymbol{q})|$ was

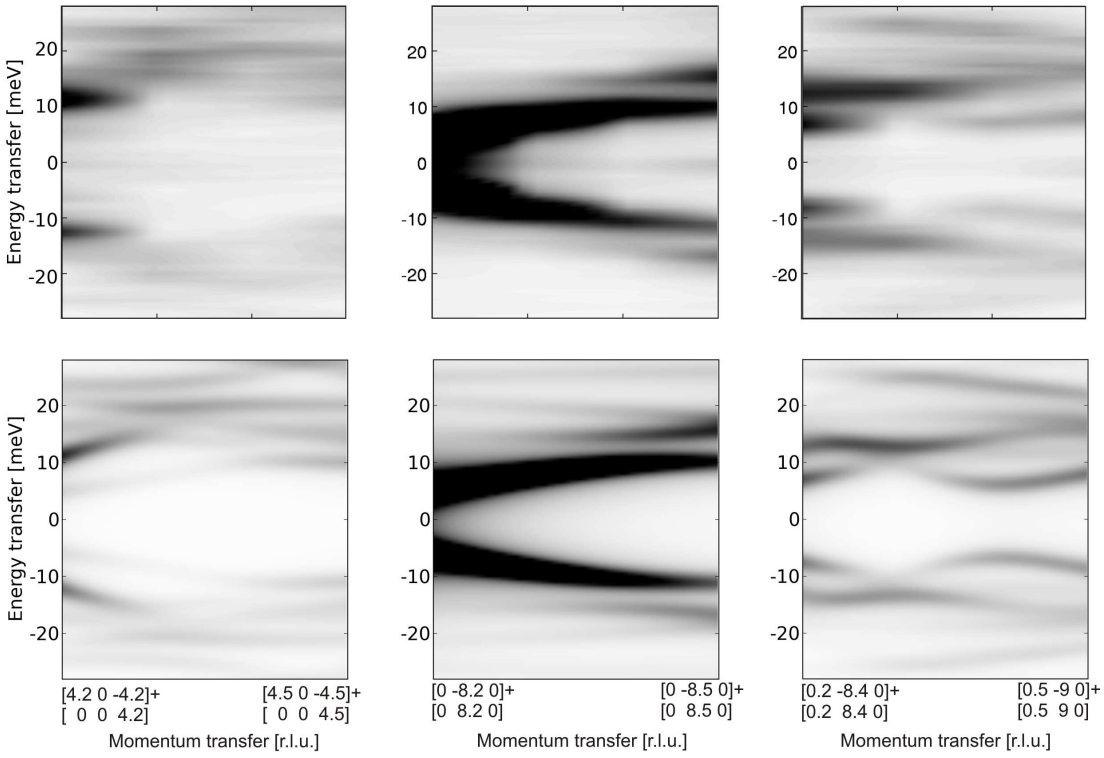

Figure 6.10: Experimental IXS intensity maps (first row) from coesite crystal together with theoretical intensity maps along the indicated directions (second row). Each experimental map consists of 4 measured spectra with linear Q-spacing and energy steps of 0.7 meV. The momentum- and energy- transfers are linearly interpolated to 20 q-points and 72 energy steps. The theoretical maps were obtained by the weighted superposition of inelastic spectra for the two domains. The inelastic intensity is calculated from the eigenvectors and eigenfrequencies for 120 points along the given direction in reciprocal space and convoluted with the experimental resolution function of the spectrometer.

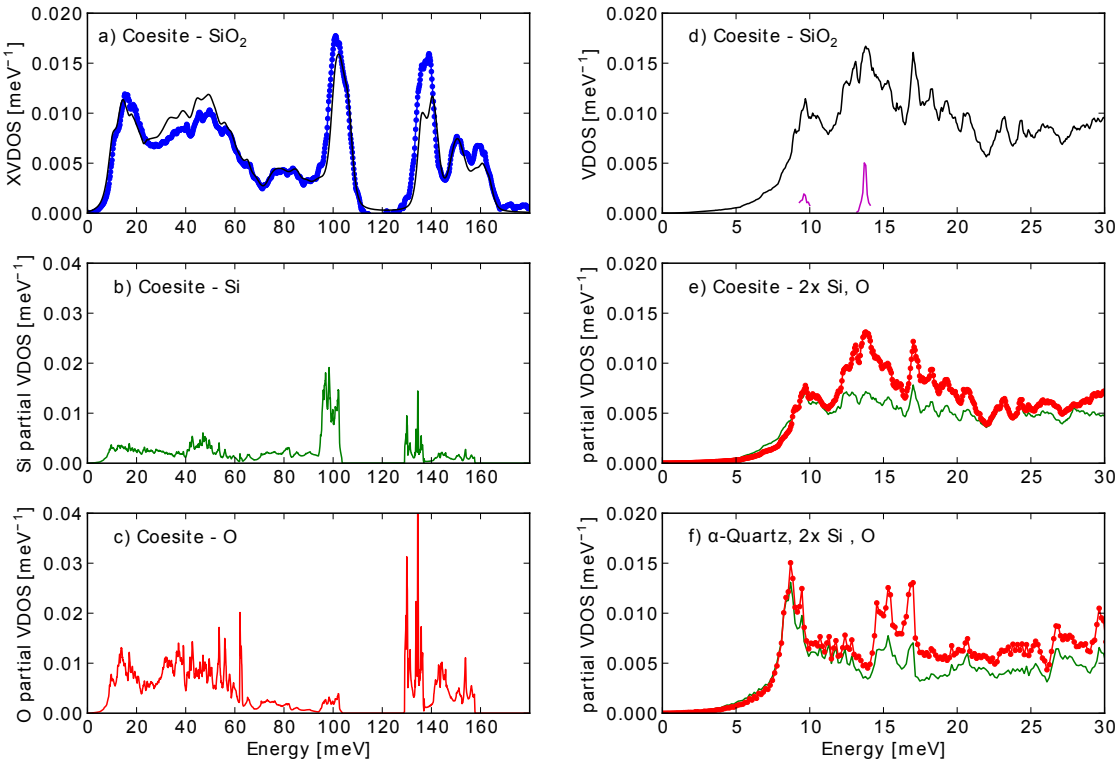

Figure 6.11: a) Experimental (blue points) and theoretical (black line) X-VDOS of coesite. The calculated X-VDOS is the x-ray weighted sum of the partial VDOS of oxygen (b) and silicon (c). The energies of the theoretical data were scaled by 1.045 and the resulting spectrum was broadened by the experimental resolution. d) Low-energy part of the VDOS (black line) and the local contribution of the critical points to the VDOS within a cube in reciprocal space with $\Delta q = 1$ nm^{-1}. The partial VDOS of oxygen (red dots) and silicon (green line) are compared in (e), where the silicon contribution is multiplied by a factor of two. f) Partial VDOS of oxygen (red dots) and silicon (green line) in the low-energy range of α-quartz. The silicon contribution is multiplied by a factor of two.

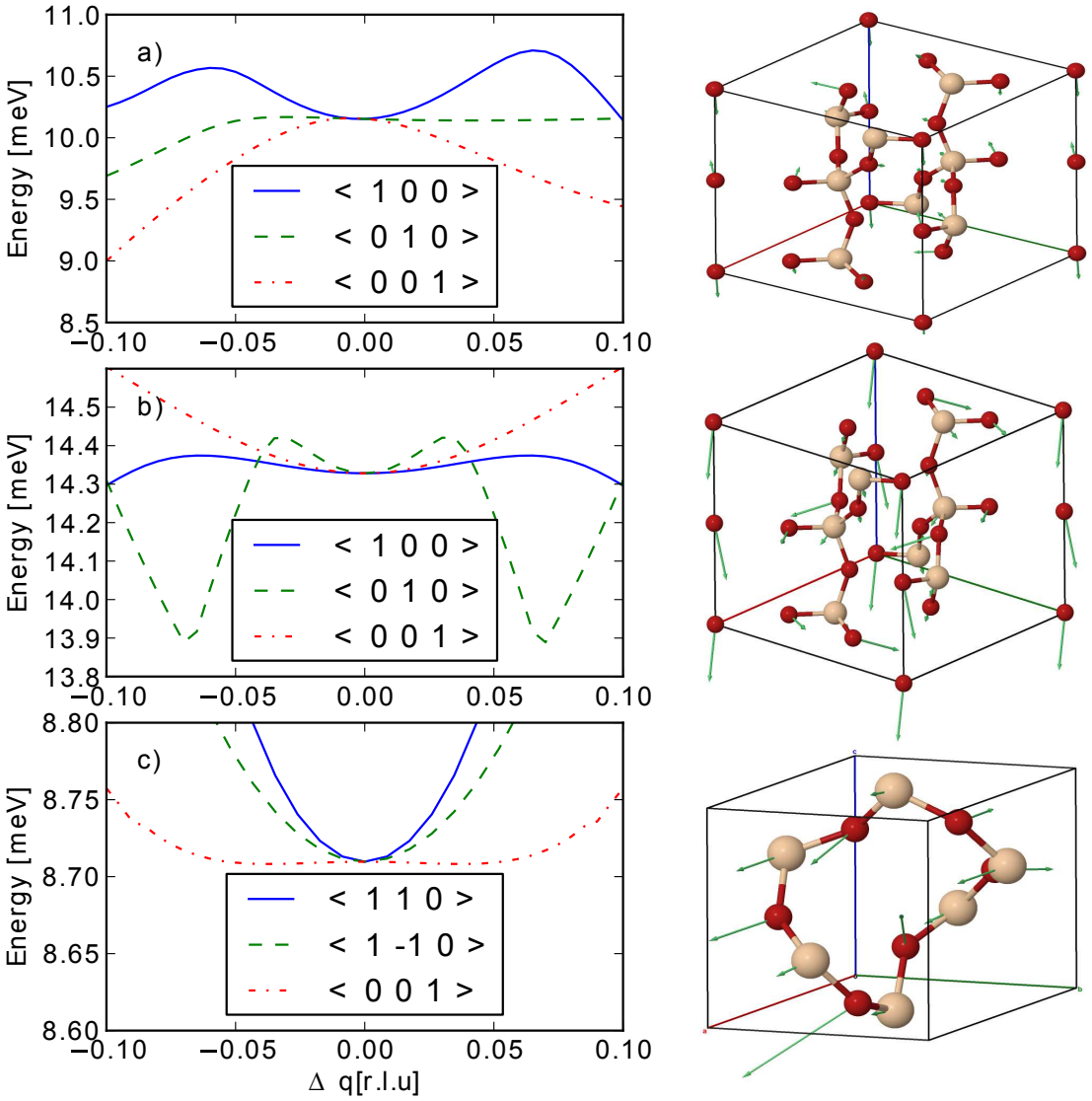

Figure 6.12: a) Dispersion relations along the main crystallographic directions through the critical point (0.87 0.69 0.42) and the displacement pattern (primitive cell) of the atoms at this saddle point contributing strongly to the first peak in the VDOS of coesite. b) Dispersion relations and displacement pattern at the Y point (1 0 0) in coesite. c) Orthogonal dispersion relations and displacement pattern at the L point (1/2 0 1/2) in α-quartz.

computed within this energy window. A saddle point close to the zone boundary at (0.87 0.69 0.42) was found to contribute strongly to the first peak in the VDOS and a local minimum at Y (1 0 0) is responsible for the main peak of the VDOS. The local contribution of the critical points to the VDOS within a cube in reciprocal space with $\Delta q = 1$ nm-1 is shown in Figure 6.11 d). The dispersion relations along the main crystallographic direction through the critical points and the displacement patterns are shown in Figure 6.12 and compared to the ones of α-quartz.

Summarizing the results shown in Figure 6.11 and 6.12 we note: (i) Critical points close to or at the zone boundary contribute most to the first and main peak of the low energy VDOS in both systems. This observation might be explained in a simplified picture with the piling up of vibrational states due to a flattening of the dispersion relations at the zone boundary (Van Hove, 1953). (ii) The first peaks in both coesite and in α-quartz are due to an almost equal contribution from silica and oxygen atoms. The main peak in coesite is, however, dominated by the vibration of oxygen atoms. The character of vibration is more libration like. (iii) In coesite both the first and the main peak are located at higher energies than in α-quartz. This observation could be expected from the higher density structure but we observe that (iv) the atomic displacements of both critical points in coesite are different from the atomic displacement pattern of α-quartz. This shows that the peaks cannot be compared directly.

Calculated dispersion relations along high symmetry directions and the result of an interatomic potential calculation (Dean et al., 2000) together with experimental values from the IXS measurements and Raman scattering (Liu et al., 1997) are shown in Figure 6.13. The two calculations are in reasonable qualitative agreement for most of the branches. However for the Y - Γ - direction our calculation agrees much better with the experimental results, particularly for the fast acoustic and the measured optic mode. The calculation of the low energy optical branches is very delicate and sensitive to small geometrical differences and require a fine electronic grid sampling. We note that both acoustic and optical phonon branches contribute to the main peak of the scattering function at 14.4 meV. The M - Y dispersion relation of the branch containing the critical point is very flat. Experimental phonon energies as determined by the IXS measurement and Raman scattering (Liu et al., 1997) are in good agreement with our calculation.

The calculation is further compared to experimental results from Raman and infrared (Lippincott et al., 1958) studies in Table 6.2. The modes were attributed by a careful comparison of experimental and calculated intensities. A good overall accordance is obtained. The calculation predicts some additional modes to be Raman or infrared active with low intensity contribution. A Raman spectrum modelled for a Laser wavelength of 514.5 nm (Ar laser) at room temperature

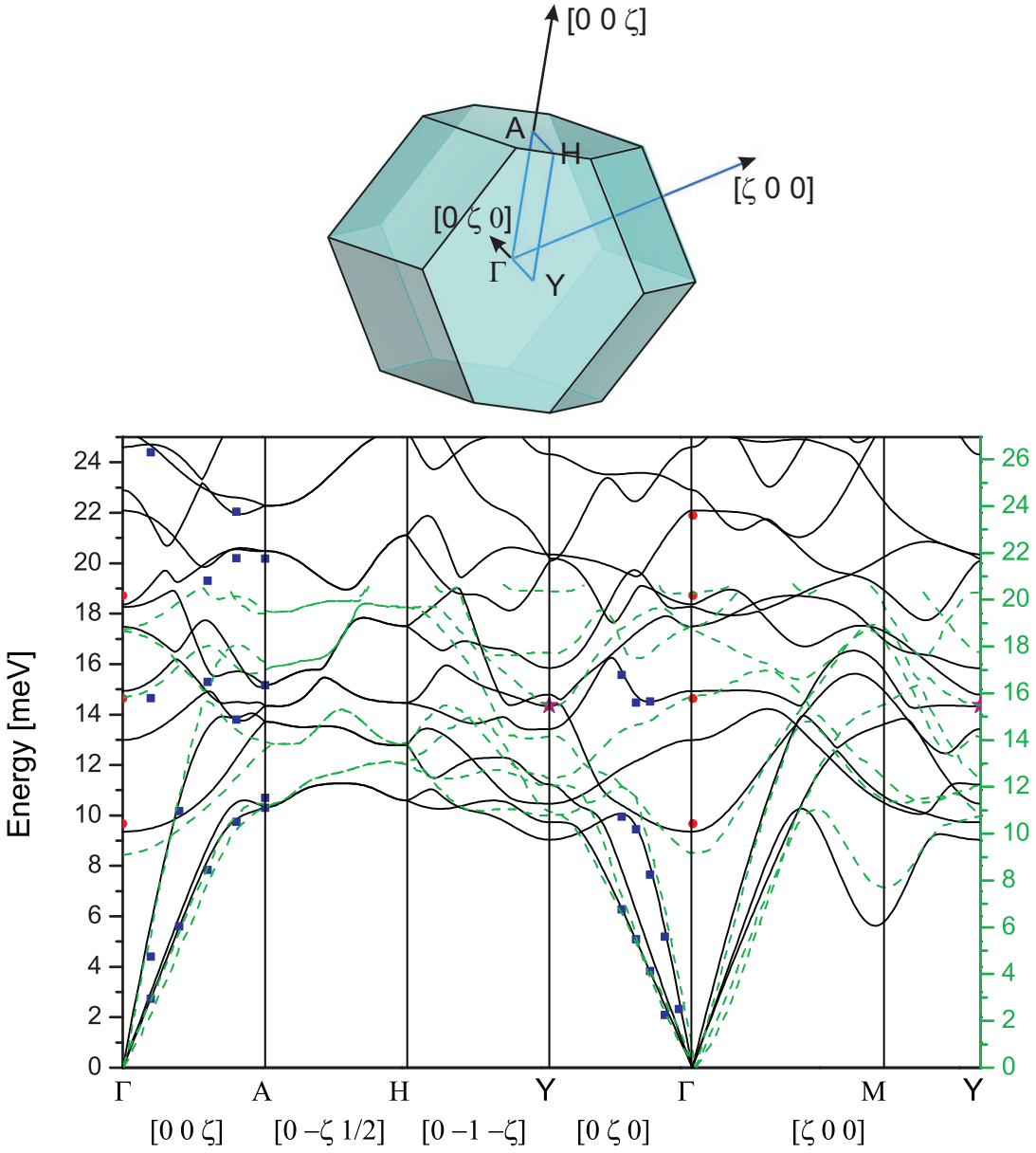

Figure 6.13: Brillouin zone of coesite crystal together with calculated dispersion relations along high symmetry directions (black lines), the results of an interatomic potential calculation (Dean et al., 2000) (dashed green lines) and experimental values from the IXS measurements (blue squares) and Raman measurements (Liu et al., 1997) (red points). The critical point at Y is marked with a magenta star. The energies of our calculation are scaled by 1.045 whereas the energies of interatomic potential calculation are scaled arbitrary for best visual fit.

Table 6.2: Raman and infrared energies [meV] of coesite at ambient conditions. The calculated values are scaled by 1.045. Intensity contributions are indicated by very weak (vw), weak (w), strong (s) and very strong (vs). Experimental values are taken from Liu et al. (1997) (Raman) and Lippincott et al. (1958) (Infrared)

Raman				infrared			
Calculation		Experiment		Calculation		Experiment	
9.4	w	9.7	s	13.0	vw	-	
14.9	s	14.6	s	17.5	vw	-	
18.3	w	18.7	w	18.4	vw	-	
22.1	s	21.9	s	22.9	vw	-	
24.6	vw	-		31.2	vw	-	
25.1	s	25.3	w	32.5	vw	-	
30.3	w	30.3	w	33.8	vw	-	
33.8	s	33.6	s	36.4	vw	-	
35.9	vw	-		36.9	vw	-	
39.3	w	-		37.4	vw	-	
40.9	w	40.4	w	40.7	vw	-	
44.2	w	44.1	w	42.2	w	42.2	w
47.2	w	47.0	w	46.2	w	-	
53.1	s	52.9	w	46.8	w	-	
55.1	w	-		48.9	w	48.3	w
57.6	vw	-		52.1	w	53.3	w
58.5	w	57.8	w	52.2	w	-	
65.7	vs	64.6	vs	55.0	w	54.8	w
68.4	w	-		56.6	w	-	
84.2	vw	-		61.4	w	-	
85.6	w	-		69.6	w	69.1	w
101.3	w	97.6	w	75.9	w	74.1	w
101.6	s	101.2	w	85.8	vw	-	
105.1	s	104.0	w	87.1	w	84.7	w
105.9	vw	105.5	w	102.5	w	98.7	w
108.1	w	110.7	w	105.0	w	100.8	w
135.6	s	132.2	w	108.1	vw	-	
136.1	w	132.8	w	135.4	vs	129.0	vs
139.7	w	139.0	w	139.5	vs	136.1	vs
140.5	w	141.8	w	140.4	w	-	
149.1	s	-		142.8	s	145.1	w
151.0	s	-		149.3	w	-	
153.2	w	-		150.4	w	151.9	w
				159.3	vw	-	
				160.6	w	-	

and an infrared spectra modelled for room temperature are shown together with experimental spectra in Figure 6.14. The calculation of Raman and infrared intensities involves the third derivation of the total energy (Giannozzi and Baroni, 1994). The convergence criteria are tighter than for calculating the dynamical matrix. The results shown here are sufficiently converged for a mode attribution but the absolut intensities were not tested for convergence.

With the knowledge of the phonon dispersion relations and the VDOS we can now go back to the intensity distribution of TDS and investigate the origin of divers features. For this purpose the same sections of TDS intensity distribution as shown in Figure 6.8 are computed taking into account exclusively phonons with energies within specified windows, see Figure 6.15. The TDS intensity distributions from phonons comprising the full energy range are compared to the intensity distribution comprising the first and main peak in the VDOS (0 - 16.5 meV). The intensity distributions were calculated from phonon eigenvectors and energies on 800 $\times$ 800 Q-points as obtained by Fourier interpolation in the first Brillouin zone and symmetry operations for the outer zones. The lower limit of the phonon energies was set to 10^{-3} meV for numerical reasons. We note that the intensity distribution comprising the first and main peak can describe all strong features. The absolute contribution to the HK0 plane (first column) is 84% and from the contribution of the full energy range in the visible Q-range. The percentage for the reciprocal space sections in the second and third column is 76%. The applied energy window does not account for a separation of the contribution of different modes. However, it illustrates, that TDS is most sensitive to the low energy part of the lattice dynamics.

Conclusions

With the validated model it is possible to access the dynamical properties at arbitrary momentum transfer. The investigation of the VDOS, probing the ensemble of vibrational states, allows the identification of distinct dynamical features. In the case of coesite a small linear energy scaling of the *ab initio* calculated phonon frequencies leads to a good agreement of experiment and theory. The investigation of the nature of the dominating features in the low energy part of the VDOS shows that critical points located close to or at the zone boundary provide the largest contribution. The contribution of oxygen atoms is found to dominate the main peak. The extension of the model for the lattice dynamics at ambient conditions to high pressure potentially builds the basis for understanding the compression mechanism and phase stability. This extension may provide an accurate model for the elastic properties at the formation of coesite inclusions in diamond implying a precise calibration of the coesite-in-diamond barometer proposed in Ref. (Sobolev et al., 2000). Comparison with the most abundant silica polymorph α-

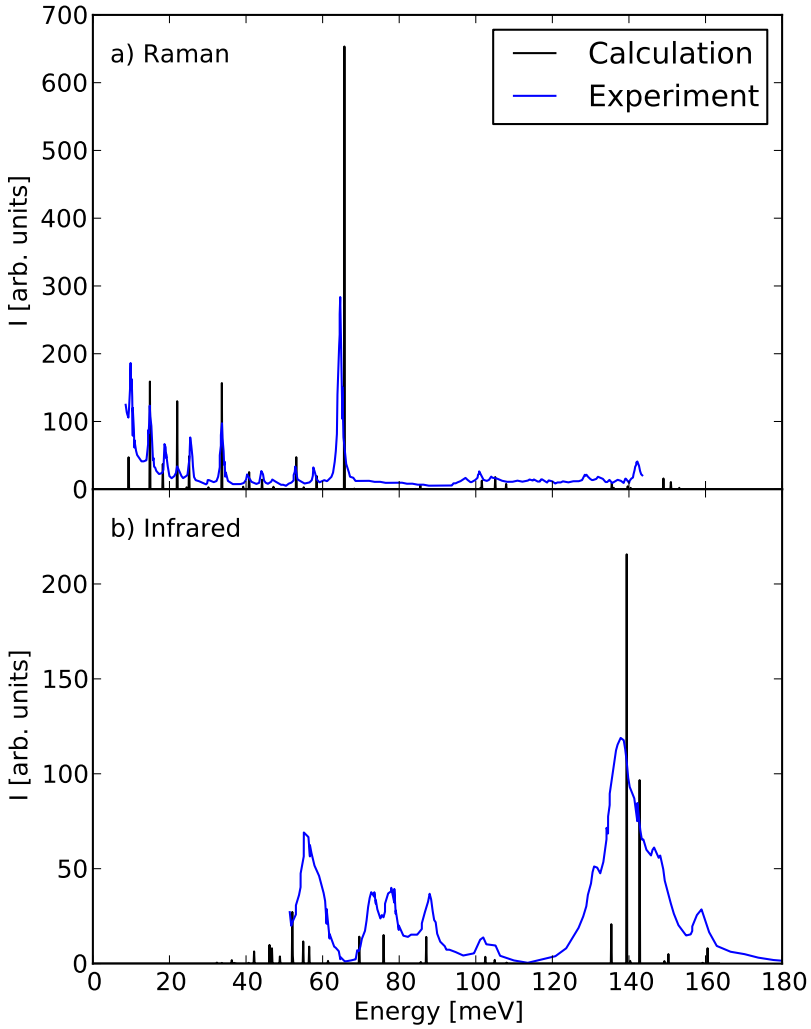

Figure 6.14: Calculated Raman and infrared spectra of coesite together with experimental results from Liu et al. (1997) (Raman) and Williams et al. (2000) (infrared). The polarisation of the incoming radiation and the resolution are not taken into account.

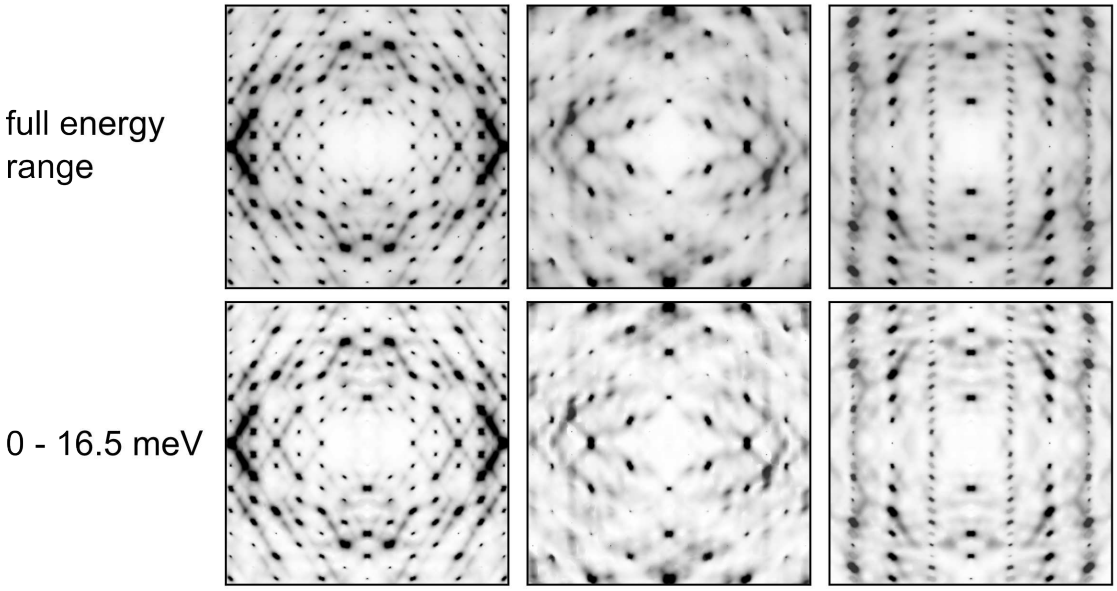

Figure 6.15: TDS intensity distribution of coesite from phonons within specified energy windows. The sections in reciprocal space are equivalent to the experimental ones in Figure 6.8. First row: TDS intensity distributions from phonons comprising the full energy range. The second row comprises TDS intensities from the specified energy window.

quartz reveals valuable new insights into the low-energy vibrational properties of this prototypical oxide.

6.3 Cristobalite

The combination of diffuse and inelastic x-ray scattering combined with *ab initio* lattice dynamics calculations is used to investigate the origin of the first peak in the density of vibrational states of α-cristobalite. The system is in particular interesting due to its structural similarity to ambient silica glass. Diffuse scattering is used to map out the intensity contribution of low energy phonon modes in reciprocal space. Selected features are investigated by IXS and compared to theory. Distinct features in the lattice dynamics are compared to the findings in α-quartz and coesite revealing similarities in the vibrational character of the modes contributing most to the first Van Hove singularities.

Introduction

Cristobalite, SiO_2, crystallises at high temperature to a cubic structure (β-phase) and undergoes a phase transition to its α-phase upon cooling. α-cristobalite has space group $P4_12_12$ (Pluth et al., 1985) and is stable at room temperature and ambient pressure. Natural crystals are usually twinned (Dollase, 1965). Recently it could be shown that ambient silica glass and α-cristobalite, which exhibit of very similar mass densities (2.20(1) g/cm^3 and 2.289(1) g/cm^3, respectively), reveal very similar thermodynamic properties and distinct similarities on the level of atomic vibrations (Chumakov et al., 2013). The boson peak of ambient silica glass (see Section 1.2) is located at the same energies as the first van Hove singularity of α-cristobalite. The VDOS in the energy range of the Boson peak is well described by the smearing out of the van Hove singularity, thus taking into account a finite width of the boundary of the pseudo-Brillouin zone in the glass. The boson peak and the van Hove singularity contain the same number of excess states above the Debye levels in both ambien silica glass and α-cristobalite. These observations strongly suggest that, similar to crystals, the excess of vibrational states in glasses originates from the piling up of the acoustic-like branches near the boundary of the pseudo-Brillouin zone. This suggests in turn that the low-energy dynamics in the meV range and the low-temperature heat capacity around 10K of silica glass are not anomalous. They are indeed similar to those of a crystal with similar mass density. They reflect more the residual order present in glasses than their structural disorder. In the following we use the combination of TDS, IXS and *ab initio* lattice dynamics calculation to clarify the reciprocal space positions of the van Hove singularity in α-cristobalite and the nature of the associated vibrations.

Experimental Details

α-cristobalite crystals from Ellora Caves, Hyderabad, India used for this study were kindly made available from the Harvard Mineralogical Museum collection (Courtesy of the Harvard Mineralogical museum, Cristobalite, HMM#97849). An octahedral single crystal with 0.2 mm along the four-fold axis was used for both TDS and IXS studies which were conducted at room temperature. One major twin and some mosaic spread was observed during the x-ray diffuse scattering. One domain could be used for experimental study with very little contribution of the the other one. A synthetic polycrystalline sample provided by M. Dove was used for the powder IXS measurements. The purity of the polycrystalline sample was verified by high-resolution x-ray diffraction at ID28. The samples revealed pure single-phase patterns. The crystalline quality was checked by x-ray diffuse scattering collected at ID29. Clear patterns of diffraction rings without noticeable effects of structural disorder were observed.

The x-ray diffuse scattering experiment was conducted on beamline ID29 (de Sanctis et al., 2012) at the ESRF. Monochromatic X-rays with wavelength 0.700 Å were scattered from the crystal in transmission geometry. The sample was rotated with an increment of 0.1° orthogonal to the beam direction over an angular range of 360° while diffuse scattering patterns were recorded in shutterless mode with a PILATUS 6M detector (Kraft et al., 2009). The orientation matrix and geometry of the experiment were refined using the CrysAlis (Oxford diffraction Ltd.) software package. 2D reconstructions were prepared using locally developed software.

The single crystal IXS study was carried out on beamline ID28 at the ESRF. The spectrometer was operated at 17.794 keV incident energy, providing an energy resolution of 3.0 meV full-width-half-maximum with a beam focus of 30 × 60 μm full-width-half-maximum. IXS scans were performed in transmission geometry along selected directions in reciprocal space.

The generalised x-ray weighted VDOS (X-VDOS) was obtained from IXS spectra measured by A. Chumakov and A. Bosak at ID28. The scattered radiation was collected by nine crystal analysers. The momentum transfer resolution of each analyser was ≈ 0.3 nm^{-1}. The values of the momentum transfers for each analyser were chosen away from the Debye-Scherrer rings and covered the [10 : 70] nm^{-1} range. The data combine the results of measurements with 1.4 meV resolution at 23.725 keV incident energy within [-25 : +25] meV energy range and 0.2 meV energy steps and results from the measurement with 3.0 meV resolution within [-25 : +180] meV energy range and 0.7 meV steps. The elastic peak in the IXS spectra was subtracted using the instrumental function of each analyser determined by x-ray scattering from a polymethylmethacrylate (PMMA) sample close to the maximum of its structure factor. The X-VDOS was obtained from the summed IXS spectra within the incoherent approximation following the data

treatment procedure established in Bosak and Krisch (2005). See Section 5.8 for details on the data analysis.

Calculation

The lattice dynamics calculations were performed using the DFPT approach (Gonze and Lee, 1997) as implemented in the CASTEP code (Clark et al., 2005, Refson et al., 2006). Local density approximation within the plane-wave formalism was employed using the same norm-conserving pseudopotentials as for the study on coesite and α-quartz. The plane wave cut-off and the sampling of the electronic grid were carefully tested by evaluating the convergence of internal forces. The electronic structure was computed on a $6 \times 6 \times 6$ Monkhorst-Pack grind and the plane wave cut-off was set to 800 eV. A full geometry optimisation was performed employing the Broyden-Fletcher-Goldfarb-Shannon method (Pfrommer et al., 1997), varying lattice and internal parameters. For the cell parameters of the optimised cell we find a = b = 4.939 Å and c = 6.870 Å. These values compare within 1.1% to those determined by x-ray diffraction (a = b = 4.97(8) Å and c = 6.94(8) Å (Dollase, 1965). Phonon frequencies and eigenvectors were computed on a $7 \times 7 \times 7$ Monkhorst-Pack grid of the irreducible part of the Brillouin zone by a perturbation calculation. Sum rules for the acoustic branches close to and at Γ as well as the charge neutrality at the level of Born effective charges were imposed. See Chapter 3 for details. A Fourier interpolation with a grid spacing of 0.005 $Å^{-1}$ in the cumulant scheme including all image force constants was applied for the VDOS. The calculation was tested to be well converged with a maximum error in phonon energies of < 0.05 meV. TDS and IXS intensities were calculated from the phonon eigenvectors and frequencies following the formalism discussed in Chapter 2 within the validity of both the harmonic and adiabatic approximation. The scattering intensities were calculated in first order approximation.

Results and Discussion

High symmetry reciprocal space sections of experimental diffuse scattering and calculated TDS intensity distributions are shown in Figure 6.16. A complex distribution of diffuse scattering is noticeable. The diffuse scattering in the H0L plane is more intense for low momentum transfers in the <1 0 1> direction in particular between ($\bar{2}$ 0 0) and (0 0 2). Its origin was proven by IXS to be of elastic nature and corresponds to the inter-twin boundary. In the HHL plane we note streak like diffuse features along <1 1 0>, in agreement with the prediction of the rigid unit modes model from Dove et al. (2007) and the observation by electron diffraction (Withers et al., 1989). Even stronger streaks are observed along <1 1 2>.

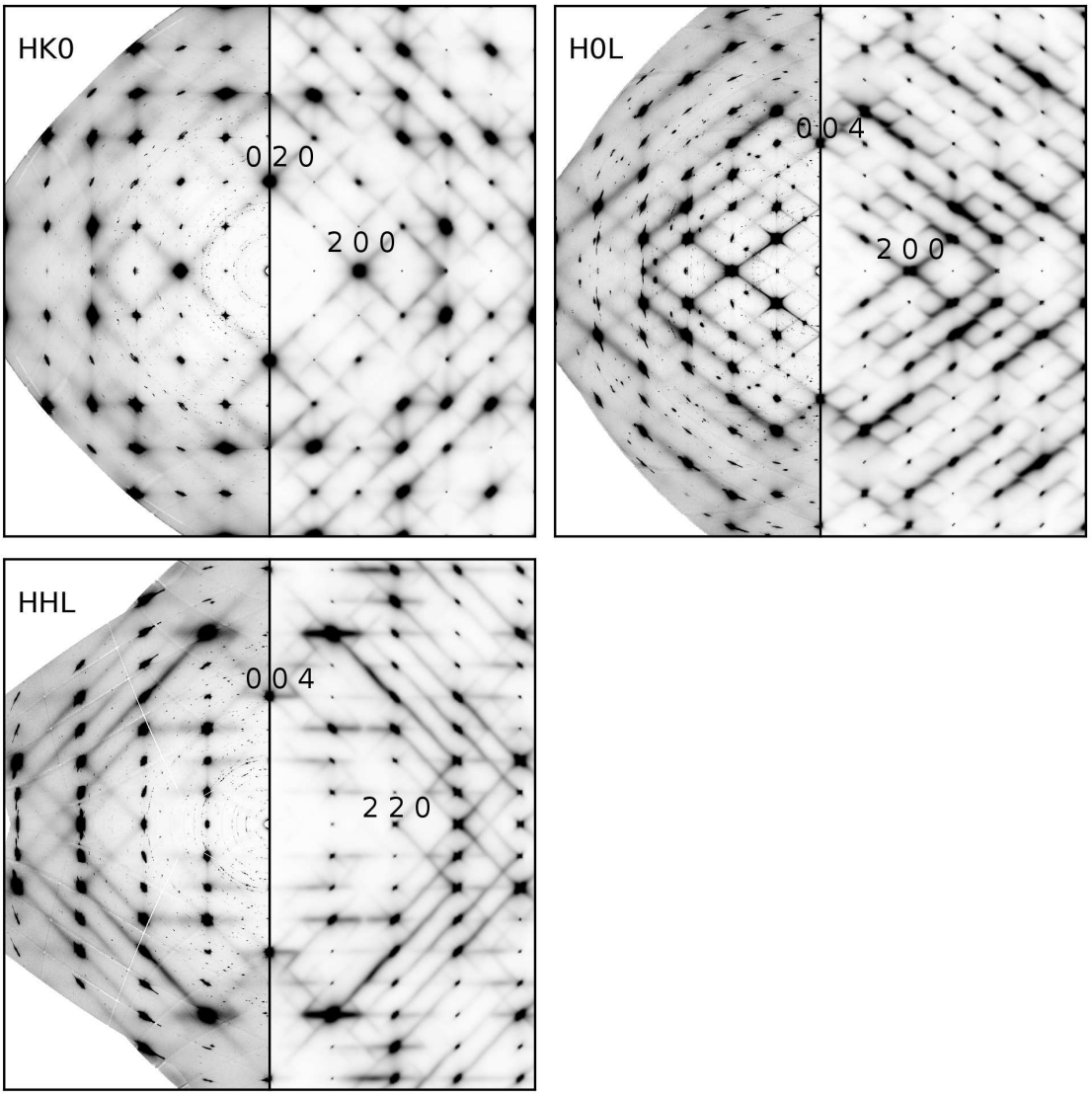

Figure 6.16: Experimental diffuse scattering (left part of individual panels) and calculated (right part of individual panels) TDS intensity distribution of α-cristobalite in the indicated reciprocal space sections. The experimental intensity distributions show signatures of the mosaic spread. See text for further details.

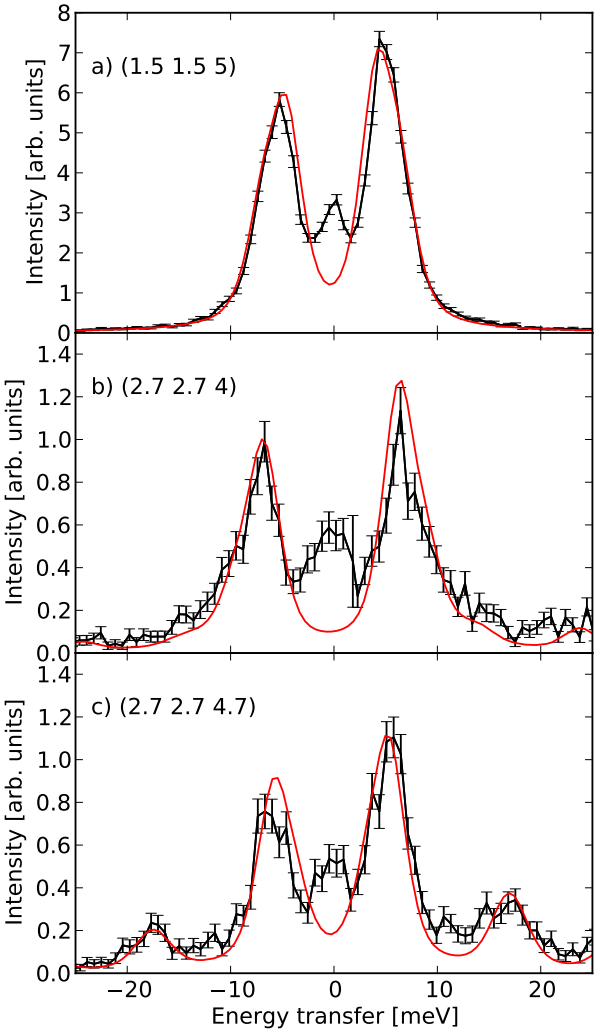

Figure 6.17: Experimental (black points with error bars) and theoretical (red line) IXS spectra from α-cristobalite at the indicated reciprocal space points. Theoretical intensities were convoluted with the experimental resolution function and the energy transfer was scaled by 1.039. The excitation in the spectrum at M point (a) contains the contribution of two branches, see Figure 6.19.

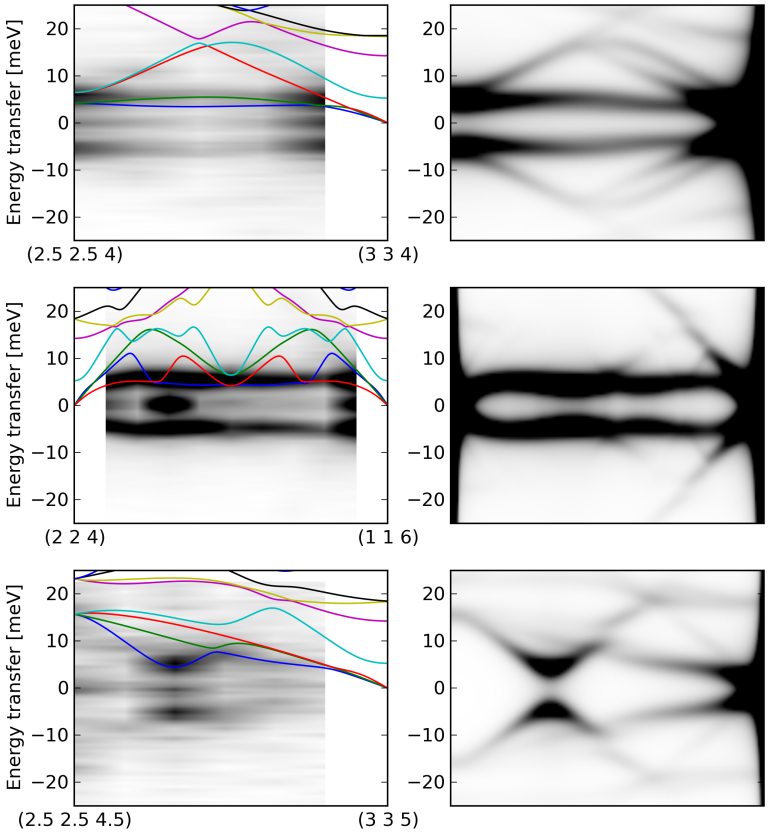

Figure 6.18: Experimental IXS intensity maps (first row) from α-cristobalite crystal together with theoretical intensity maps along the indicated directions (second row). The experimental maps in a) consist of 5 and in b) and c) of 8 measured spectra with linear $\boldsymbol{q}$-spacing and energy steps of 0.7 meV. The momentum- and energy- transfers are linearly interpolated to 200 q-points and 72 energy steps. The theoretical dispersion relations are traced as lines. The theoretical maps were calculated from the eigenvectors and eigenfrequencies for 200 points along a given direction in reciprocal space and convoluted with the experimental resolution function of the spectrometer. The absolute intensity is scaled for best visualisation of the inelastic features.

The streaks along <1 1 0> and <1 1 2> and some more directions were explored by IXS. A few prototypical scans are shown in Figure 6.17 and compared to calculated spectra. Some more IXS scans are summarised in the intensity maps along certain directions in Figure 6.18. After stretching the calculated energies by ≈4% the theoretical spectra describe quite well both position and intensity of the phonons. The scaling factor was determined from the X-VDOS, and its value is justified further below. The overall agreement of experiment and calculation is good. The minima of the lowest energy phonon branch are slightly underestimated in the showcases. A small elastic line is also present in all spectra. Figure 6.17a) and b) shows the IXS intensity map along <1 1 0> and <1 1 2>, respectively. Remarkably, we note quite flat phonon branches with energies around 5 meV. The calculation underestimates the energies of these bands slightly.

Calculated dispersion relations along high symmetry directions together with experimental values from the IXS measurements are shown in Figure 6.19. The phonon energies at the Γ point are compared to infrared (Swainson et al., 2003) and Raman measurements (Bates, 1972, Sigaev et al., 1999) as well as to *ab initio* calculated values from Coh and Vanderbilt (2008). We note good agreement of our calculation with all experimental values, whereas the calculated values from Coh and Vanderbilt (2008) are significantly different.

The X-VDOS for α-cristobalite is shown in Figure 6.20 a) and the calculated real VDOS in Figure 6.20 d). A linear scaling of all calculated phonon energies by 1.039 leads to an almost perfect agreement of experimental and theoretical X-VDOS over the complete energy range. We observe some very small discrepancies between experiment and theory, which are mainly due to the limited accuracy of sampling the reciprocal space with powder IXS spectra. The first peak in the VDOS is observed at a slightly higher energy as calculated (discrepancy is 0.9 meV after the applied scaling). The underestimation of the calculated energies can be attributed to the limited accuracy of the exchange correlation function within the local density approximation and the fact that the calculation does not include any temperature effects (see Refson et al. (2006) for a detailed discussion). The partial density of states (Figure 6.20 b and c)) separate the contribution of silicon and oxygen atoms. Focusing on the low energy part of the partial VDOS (Figure 6.20 e)) we find that the first peak located at 4.56 meV is slightly dominated by the vibration of the oxygen atoms. The low energy VDOS of α-quartz is plotted in Figure 6.20 f) for comparison. We note that the first peak of the VDOS of α-cristobalite is located at much lower energy than in α-quartz. In α-cristobalite the partial contribution of oxygen atoms is slightly higher than in α-quartz.

The localisation of critical points contributing most to the first peak of the VDOS was conducted by the simultaneous application of two filters. An energy filter of ΔE= 0.3 meV was applied to the *ab initio* calculated phonon energies of the

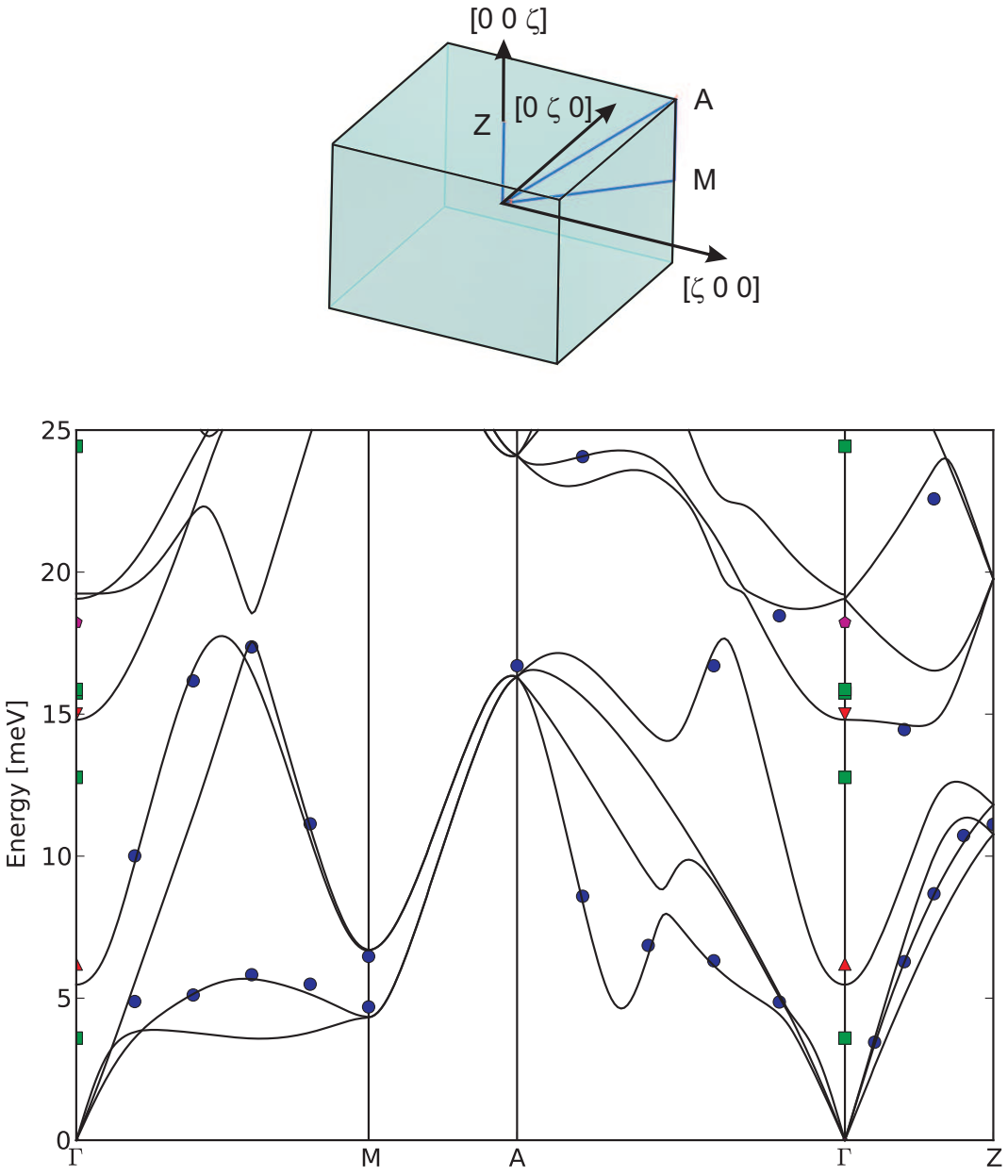

Figure 6.19: Brillouin zone of α-cristobalite together with calculated dispersion relations along high symmetry directions (black lines) and experimental values from the IXS measurements (blue points).The phonon energies at the Γ point are compared to Infrared (Swainson et al., 2003) (magenta diamonds) and Raman measurements (Bates, 1972) (red triangles up) and (Sigaev et al., 1999) (red triangles down) as well as *ab initio* calculated values from Coh and Vanderbilt (2008) (green squares). The energies of our calculation are scaled by 1.039.

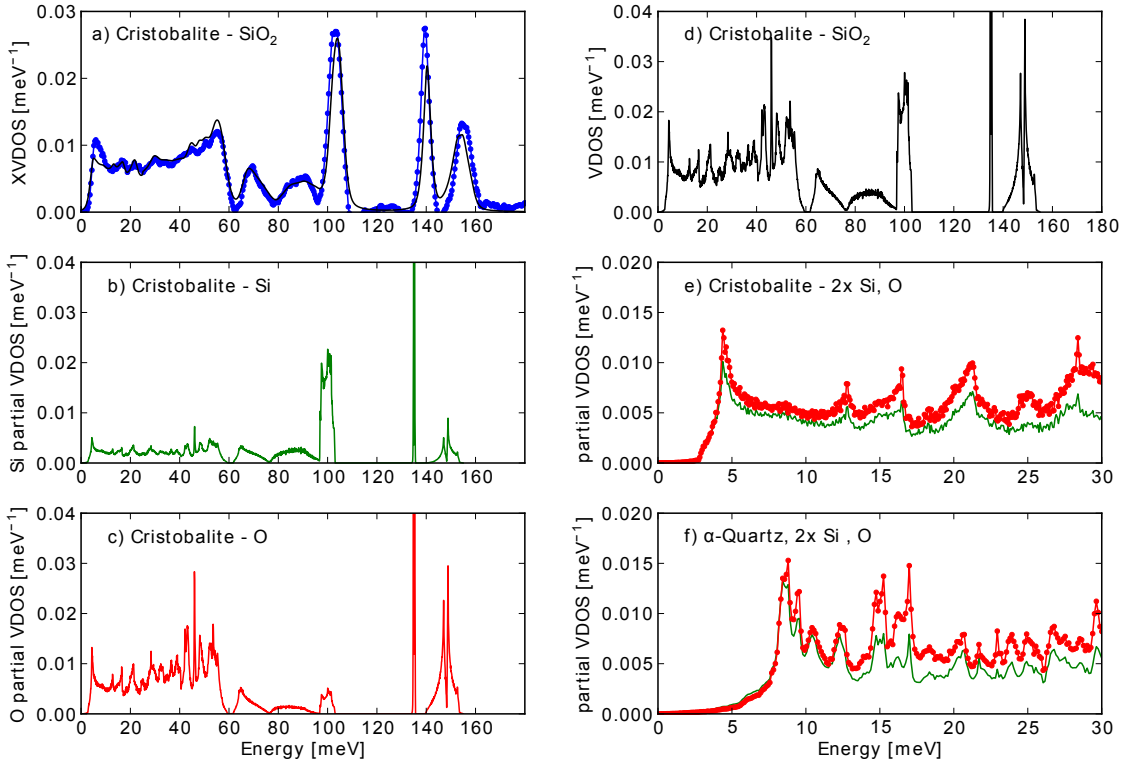

Figure 6.20: a) Experimental (blue points) and calculated (black line) X-VDOS of α-cristobalite. The calculated X-VDOS was convoluted with the experimental resolution function and the energies scaled by ≈4%. The partial VDOS of oxygen and silicon and the VDOS are shown in b), c) and d), respectively. The partial VDOS of oxygen (red dots) and silicon (green line) of the low energy part are compared in (e), where the silicon contribution is multiplied by a factor of two. f) Partial VDOS of oxygen (red dots) and silicon (green line) in the low-energy range of α-quartz. The silicon contribution is multiplied by a factor of two.

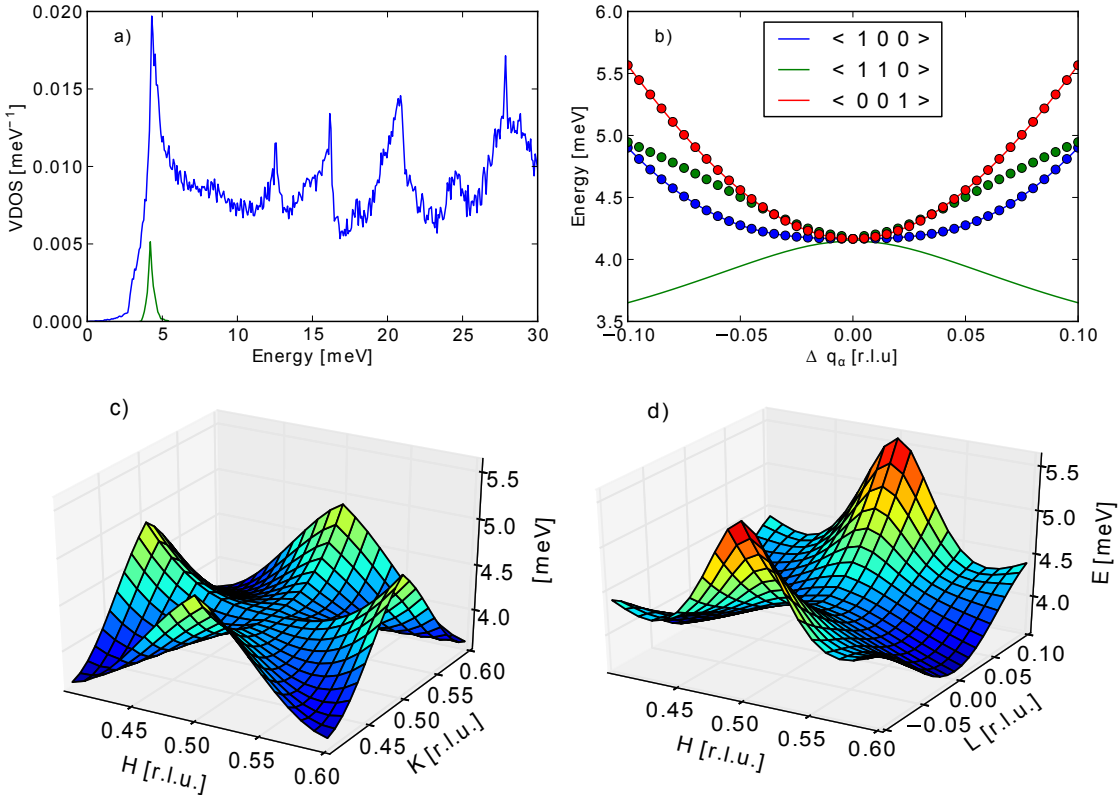

Figure 6.21: Contribution and topology of the critical point responsible for the first van Hove singularity in α-cristobalite. a) VDOS (blue) and the contribution of the energy surface containing the critical point at M (1/2 1/2 0) within $\Delta q = 1\text{nm}^{-1}$ (green). b) Dispersion relations of the two branches containing the critical point along the indicated directions. The straight lines belong to the energy surface containing the saddle point, the dots belong to the sheet containing a minimum. c) and d) Energy surface projections of the dispersion surface containing the saddle point in the HK0 and HHL plane, respectively.

first Brillouin zone, and $1/|\nabla_{\boldsymbol{q}} E(\boldsymbol{q})|$ was computed within this energy window. The investigation reveals two saddle points with the same phonon energy contributing to the first peak in the VDOS of α-cristobalite. The computation of the local contribution within a cube in reciprocal space of $\Delta q = 1$ nm^{-1} shows that the first peak arises mainly from the region around the M point (1/2 1/2 0). The local contribution is shown in Figure 6.21 a). The phonon dispersion surface containing the critical point shows a double degeneracy along <1 0 0>, <0 1 0> and <0 0 1>, which is split along the <1 1 0> direction, see Figure 6.21 b). The lower sheet forms a saddle point whereas the upper sheet forms a minimum which is of parabolic nature close to M. The peak in the VDOS arises thus from the lower branch (see discussion in Section 6.1). The topology of the energy surface projected on the HK0 and HHL plane is shown in Figure 6.21 c) and d). A second saddle point with the same phonon energy located at (0.47 0.2 0.33) was found to have a smaller local contribution to the VDOS.

The VDOS of the silica polymorphs α-quartz, coesite and α-cristobalite and the displacement patterns of the vibration responsible for the first peak are compared in Figure 6.22. We note, that the low energy part of the VDOS is different. In particular the first peak in the VDOS is located at different energies. Quite remarkable is the fact that critical points which are responsible for the first peak are located at the zone boundary in the case of all three silica polymorphs under investigation. The topology of the energy surface in the vicinity of the critical points is different, but despite this, the associated displacement patterns are very similar: The largest displacement is observed for oxygen. The vibration consists mainly of a tetrahedron tilt, accompanied by a small distortion. The study from Chumakov et al. (2013) revealed that the number of excess states above the Debye levels in the VDOS of ambient silica glass and α-cristobalite are very similar (6.2(9) % and 6.8(9)%, respectively). It was furthermore shown that the excess states for both glass and crystal are located nearly at the same energy. Taking into account the similarity observed in the displacement patterns of the investigated three silica polymorphs we can now conclude, that the vibration causing the Boson peak in silica glasses must be similar as well on a local scale.

Conclusions

We have seen, that the lattice dynamics of α-cristobalite can be very well described by our lattice dynamics calculation. The thermal diffuse scattering shows a rich structures, including features which were predicted by the theory of rigid unit modes. The validated calculation allowed us to draw a unifying picture for the displacement patterns of the vibration responsible for the first peak in the VDOS of all investigated silica polymorphs.

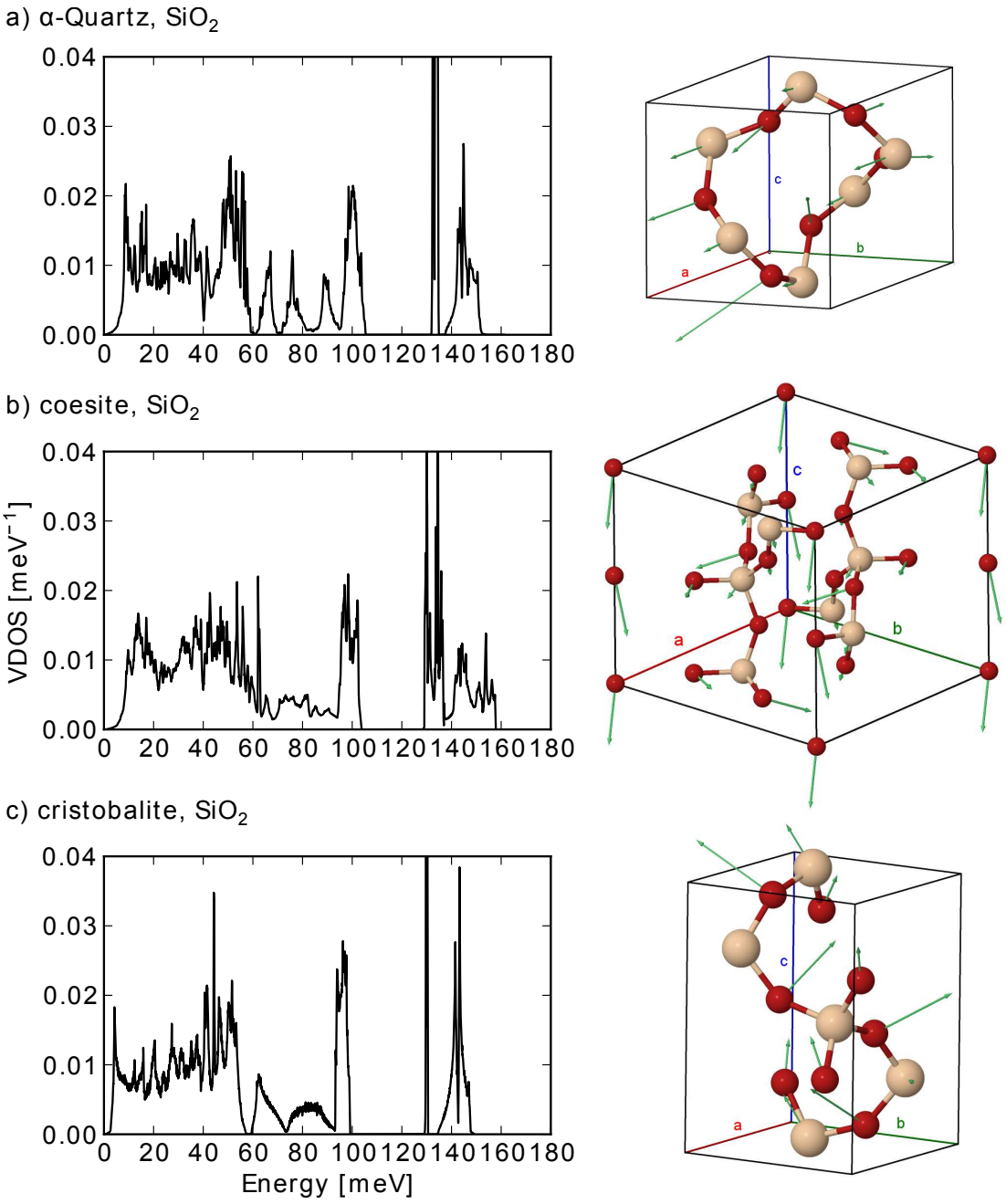

Figure 6.22: VDOS of SiO_2 α-quartz (a), coesite (b) and α-cristobalite (c) and the displacement patterns of the associated vibrations.

6.4 Metallic tin polymorphs

The lattice dynamics of the metallic tin β and γ polymorphs has been studied by a combination of diffuse scattering, inelastic x-ray scattering and density functional perturbation theory. The shape TDS intensity distributions were investigated in detail. The influence of the electron subsystems on inter-ionic interactions were analysed and the effect of the β-tin structure with a non-centrosymmetric environment of atoms considered.

Introduction

Metallic tin crystallizes in a body-centred tetragonal lattice (space group $I4_1/amd$) at ambient conditions, known as white tin ($\beta-$Sn). Despite the fact that the stability range of white tin lies between 291and $\approx$ 450 K (Kubiak, 1986) it can be supercooled far below the transition temperature maintaining the crystal structure. Below $\approx$ 4.2 K it becomes a type-I superconductor which can be described in the frame of BCS theory (Matthias et al., 1963), indicating strong electron-phonon coupling (Rowe, 1967). The $\alpha - \beta$ phase transition in tin is possibly the simplest and prototypical case of an entropy-driven structural transformation determined by the vibrational properties of the two phases (Pavone et al., 1998).

Alloying tin with indium results in a substitutionally disordered crystal with a primitive hexagonal lattice containing one atom per unit cell (Raynor and Lee, 1954), called γ-tin. It is a convenient model system in the study of lattice dynamics and electron-phonon interactions (Ivanov et al., 1987), because its phonon dispersion relations consist only of acoustic branches and it is stable at ambient conditions. The γ-phase of pure tin (Kubiak, 1986) is orthorhombic and differs thus slightly from the primitive hexagonal lattice. It is stable between $\approx$ 450 K and the melting point of tin (505 K).

Diffuse scattering of white tin has a long history. First Laue photographs showing a "diffuse background with regions of maximum intensities" were published in 1943 (Arlman and Kronig, 1943) and "considered in the light of thermal theory" in 1946 (Bouman et al., 1946). Elastic constants were derived from the diffuse features in 1955 (Prasad and Wooster, 1955). Phonon dispersion relations have been largely studied in the past, in particular by inelastic neutron scattering (INS) (Parratt, 1967, Rowe, 1967, Rowe et al., 1965) and density functional perturbation theory (Pavone et al., 1998). The available data are nevertheless limited to high-symmetry directions and the determination of the eigenfrequencies. The rich Fermi surface of $\beta-$Sn (Deviller et al., 1974) suggests a complex topology of electron-phonon interaction, studied by Ivanov et al. (1995).

Experimental Details

The diffuse x-ray scattering experiment was conducted at the Swiss-Norwegian Beamlines at ESRF (BM01) and the ID29 ESRF beamline. Monochromatic X-rays with wavelength 0.7 Å were scattered from a needle-like single crystal of 100×100 μm cross section at room temperature. Single crystal of β- and γ-tin were provided by Alexander Ivanov (Institue Laue-Langevin, Grenoble, France). They were cut by a diamond saw and polished with diamond powder. The final size was obtained by short etching in concentrated HCl acid. The sample was rotated orthogonal to the beam direction over an angular range of 360° and diffuse scattering pattern were recorded in transmission geometry. Preliminary experiments were performed with a mar345 detector (Marresearch GmbH). The follow-up experiments were employing a PILATUS 6M detector (Kraft et al., 2009) at ID29, where the diffuse scattering patterns were collected in shutterless mode with fine angular slicing of 0.1°. The orientation matrix and the geometry of the experiment were refined using the CrysAlis (Oxford diffraction Ltd.) software package, 2D and 3D reconstructions were prepared using locally developed software. The single crystal IXS study was carried out at beamline ID28 at the ESRF. The spectrometer was operated at 17.794 keV incident energy, providing an energy resolution of 3.0 meV full-width-half-maximum. IXS scans were performed in transmission geometry along selected directions in reciprocal space. See Chapter 4 and 5 details.

Calculation

First-principle lattice dynamics calculations were performed with the CASTEP package (Clark et al., 2005, Refson et al., 2006) using the DFPT solver for metallic systems (de Gironcoli, 1995). The local density approximation (LDA) and general gradient approximation (GGA) within the density functional theory formalism were used as implemented with a plane wave basis set and norm-conserving pseudopotentials. For the exchange correlation functional the Perdew and Zunger parametrization (Perdew and Zunger, 1981) of the numerical results of Ceperley and Alder (Ceperley and Alder, 1980) were used in LDA and the density-gradient expansion for exchange in solids and surfaces (PBEsol functional) (Perdew et al., 2008) in GGA. The self-consistent electronic minimization was performed with density mixing in the Pulay scheme and the occupancies were smeared out by a Gaussian function of 0.1 eV full-width-half-maximum. The Sn pseudo-potential was of the optimized norm conserving type generated using the Vanderbilt scheme with a single projector for each of the 5s and 5p electrons, with a cut-off radius of $r_c = 1.9\ a_0$. The pseudopotentials for the LDA and PBEsol calculations were created using the CASTEP on-the-fly technology, optimized separately for each

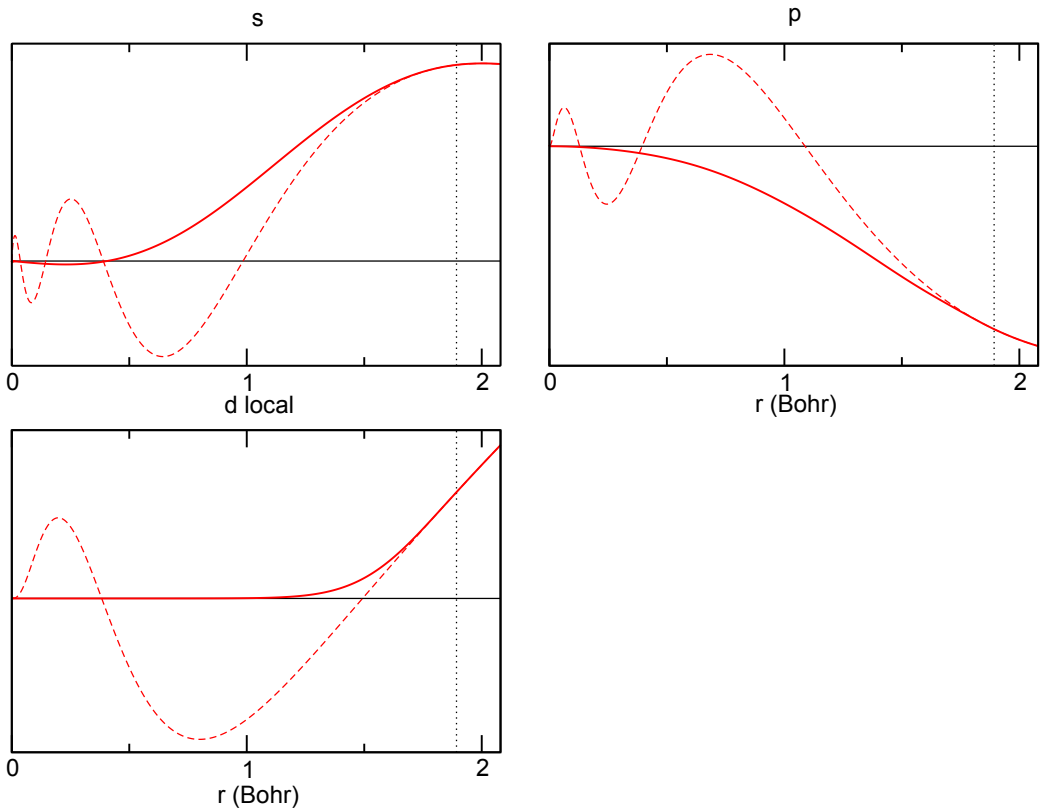

Figure 6.23: All electron (dashed line) and pseudo- (full line) wave functions of the 5s, p and d orbitals. The vertical dotted line indicates the cut-off radius.

Table 6.3: Lattice constants of β-Sn from calculation and experiment (Swanson and Tatge, 1953).

	LDA	PBEsol	Experiment
a = b	5.755 Å	5.808 Å	5.831 Å
c	3.114 Å	3.144 Å	3.182 Å

exchange and correlation functional and carefully tested for transferability [1]. The pseudo potential is compared to an all-electron calculation in Figure 6.23. The pseudation makes the wave functions nodeless, but they are identical above the cut-off radius. The pseudo-potential was tested for prediction of lattice parameters in β- and γ tin as well as tin monoxide and compared to previously published potentials (Meyer et al., 2001). The convergence of internal forces with respect to the plane wave cut-off and sampling of the electronic grid were carefully tested. In order to accurately describe the Fermi surface a very dens electronic grid is required. The self-consistent electronic minimisation was performed with density mixing in the Pulay scheme and the occupancies were smeared out by a Gaussian function of 0.1 eV full-width-half-maximum. The systems were converged in plane waves with an upper bond error for internal forces of $< 10^{-3}$ eV/Å which required a plane wave cut-off of 320 eV and $24 \times 24 \times 24$ Monkhorst-Pack grid sampling of the first Brillouin zone. The systems were converged in plane waves with an upper bond error for internal forces of $< 10^{-3}$ eV/Å which required a plane wave cut-off of 380 eV and $24 \times 24 \times 24$ Monkhorst-Pack grid sampling of the first Brillouin zone. The Fermi surface of β-tin as obtained from the electronic structure calculation is illustrated in Figure 6.24. A complex topology is visible in 3D reciprocal space. The H0L section is in good agreement with previous calculations and experiment (Deviller et al., 1974).

The structure optimization was performed using the Broyden-Fletcher-Goldfarb-Shannon method (Pfrommer et al., 1997) by varying lattice and internal parameters. The equilibrium lattice constants of β-Sn as obtained in LDA and PBEsol are reported in Table 6.3. The cell parameters agree within 2.2 % with the experimental values in LDA and 1.2 % in PBEsol. Phonon frequencies and eigenvectors were computed by perturbation calculations on a $8 \times 8 \times 8$ Monkhorst-Pack grid and further Fourier interpolated in the cumulant scheme including all image force constants (Parlinski et al., 1997). The well converged internal forces yield a maximum error in phonon energies of < 0.2 meV. The acoustic sum rule correction was applied to the calculated dynamical matrix in order to account for translational in-

[1] The CASTEP on-the-fly stings used in this work are 2|1.9|1.9|1.5|9.6|10.8|11.7|50N: 51N(qc = 4.1) in LDA and 2|1.9|1.9|1.5|9.6|10.8|11.7|50N: 51N(qc = 5.05) in PBEsol.

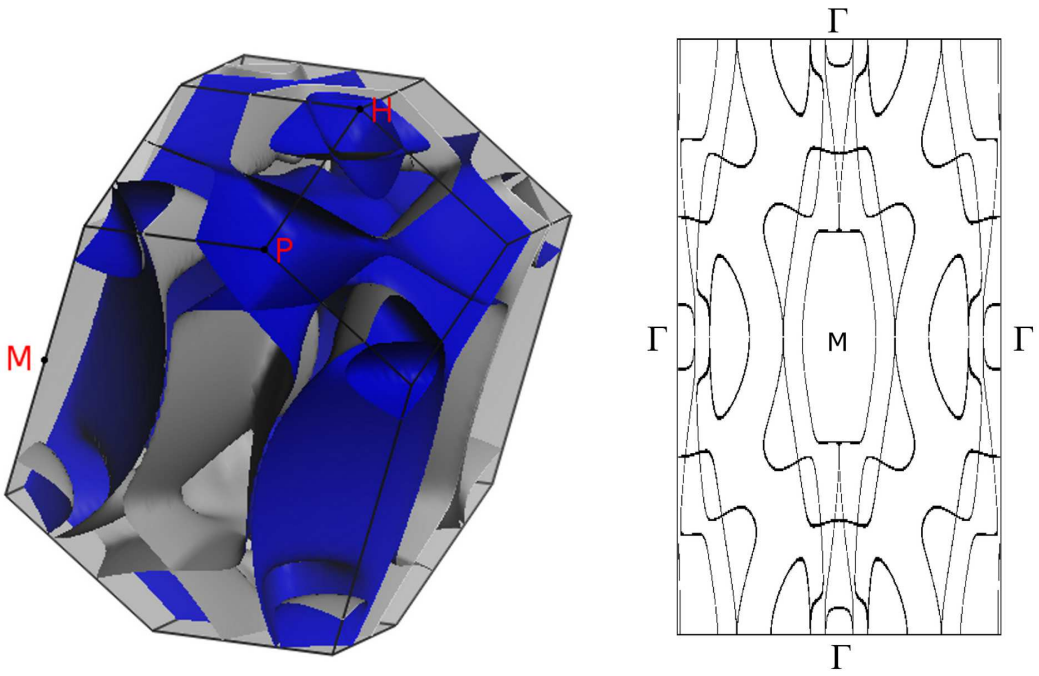

Figure 6.24: Fermi surface of β-tin as obtained from the electronic structure calculation in 3D recirocal space and in the H0L plane.

variance with maximal correction of 2 meV at Γ. The lattice dynamics calculation for γ-tin was performed in LDA with the same parameters and pseudopotential as used for β-Sn. The primitive hexagonal structure was imposed for the unit cell containing one Sn atom. The optimized cell parameters were a = b = 3.1667 Å and c = 2.9722 Å, in agreement within 1.4 % with the experimental values (a = b = 3.213 Å and c = 2.999 Å (Kubiak and K., 1974)). TDS and IXS intensities were calculated assuming the validity of both harmonic and adiabatic approximation using in house developed software (Mirone and Wehinger, 2012). The scattering intensities were calculated in first order approximation.

Results and Discussion

The calculated dispersion relations for β-tin along high symmetry directions as obtained in LDA and PBEsol are compared to experimental results from IXS and to previously published results (Ivanov et al., 1987, Parratt, 1967, Rowe et al., 1965) in Figure 6.25. Both experimental and calculated dispersion relations show several anomalies, due to the complex electronic structure with long range force constants and the interplay of electrons and phonons. Some anomalies are indicated in Figure 6.25. The influence of the applied sum rule on the phonon branches and the anomalies was carefully tested. The transformation was found to have minimal impact on the optical branches and the anomalies, but created an artefact close to the M point, labelled G in Fig 6.25. Despite the fact that the lattice constants within the LDA are underestimated by the calculation, we note a good agreement for the acoustic phonon branches and the phonon anomalies. The dispersion relations are in close agreement with previous calculations by Pavone et al. (1998). Some of the experimentally observed anomalies are better reproduced by the present calculation. In particular the anomalies labelled A - F are more accurately described. The highest energy optical mode shows several anomalies in both experiment and our calculation whereas the same branch is almost completely flat in the previous calculation. The anomalies are in fact sensitive to the Fermi surface which is described more accurate in the present calculation due to a finer k-point sampling and a smaller smearing width of the occupancies. We are therefore confident that the present calculation accounts sufficiently well for the electron-ion interaction. We note a slight over-estimation of the highest optical branch and a slight underestimation of the transverse acoustic branch in the Γ-H-M direction - the intersection of two equivalent mirror planes. A phonon with wave vector in this direction is purely longitudinal or transverse and the transverse modes are doubly degenerate. The acoustic Δ_4 branch along the Γ-X direction (see Figure 6.25) is slightly softer than experimentally observed. This may be an artefact due to the acoustic sum rule violation and correction. The reproducibility of the the optical phonon branches is improved in the PBEsol calculation but the acoustic branch

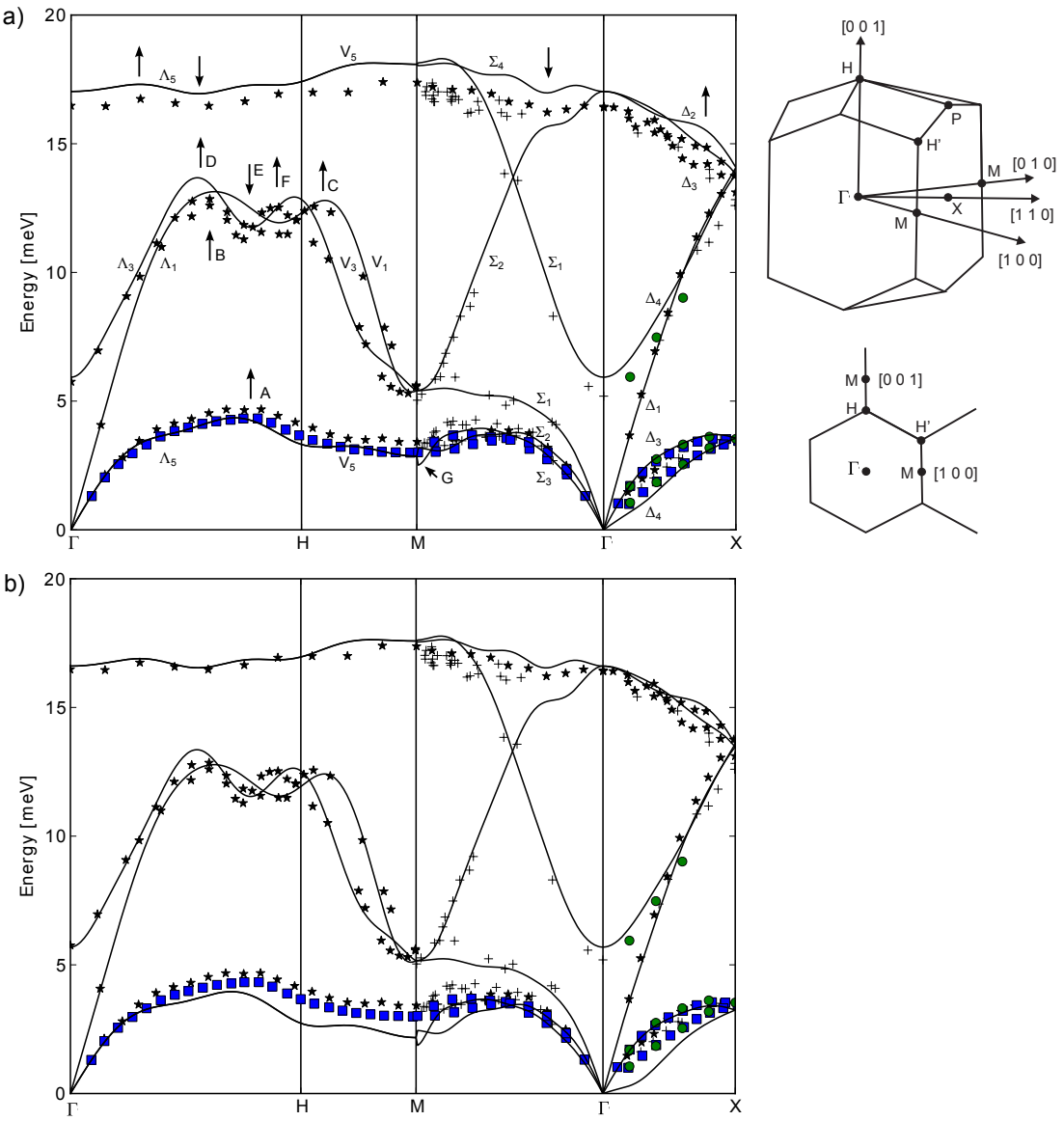

Figure 6.25: Dispersion relations of β-tin along the indicated high symmetry directions. The calculations (solid lines - a) LDA and b) PBEsol) are compared to experimental values from IXS measurements at 300K (circles), INS at 300K (squares) (Ivanov et al., 1995) and (+) (Parratt, 1967) and INS at 110K ($\star$) (Rowe, 1967). The dispersion relations along the Γ-X direction are labelled according to the symmetry classification proposed in (Chen, 1967). The differences between the experimental data sets are due to different experimental conditions: Data were taken at different temperatures, with different statistics and resolution in momentum and energy transfer. Note the pronounced anomalies in the dispersion relations (arrows). The labelled anomalies are discussed in the text. The first Brillouin zone and a section of the H0L plane in reciprocal space are shown on the right.

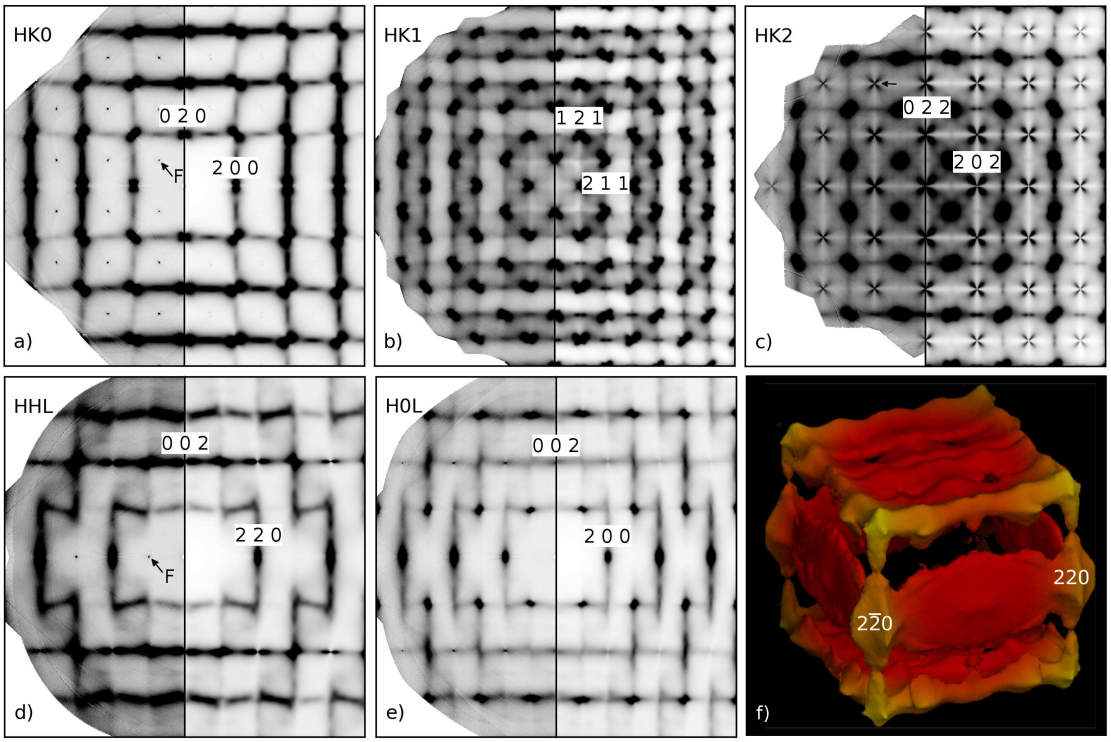

Figure 6.26: a) - e) Experimental diffuse scattering (left part of individual panels) and calculated (right part of individual panels) TDS intensity distribution of β-tin in the indicated reciprocal space sections. Note the almost forbidden reflections in a), c) and d) (arrows labelled F), visible due to the electron density asymmetry (Merisalo and Soininen, 1979). f) Experimental 3D isosurface of TDS in colour denoting the distance from (0 0 0).

along Γ-H-M and the acoustic Δ_4 branch along Γ-X are significantly softer. The discrepancy in the Δ_4 branch may again be related to the acoustic sum rule violation and correction, whereas the difference in the acoustic branch along Γ-H-M is related to the different approximation in the exchange and correlation functional. The shape of the phonon anomalies are, however, well described in both approximations. In the following the results of the LDA calculation were used because this study focuses on the low energy phonons.

Reciprocal space sections and a three-dimensional isosurface of diffuse scattering as obtained from experiment and calculated TDS intensity distributions are shown in Figure 6.26. Corrections for polarisation and projection (Holt et al., 1999), and the Laue symmetry of the system were applied. All shapes of diffuse features are remarkably well reproduced by the calculation in harmonic approximation. This implies that higher order scattering processes and anharmonic effects

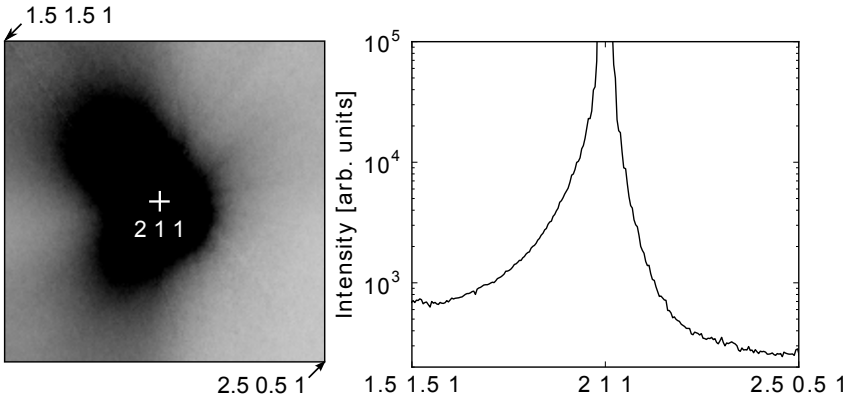

Figure 6.27: Experimental diffuse scattering of β-tin crystal in the vicinity of the 211 reflection in the HK1 plane.

at room temperature are much less pronounced than previously thought (Takahashi et al., 2006). The pronounced elastic anisotropy is reflected by the butterfly shape of TDS in the vicinity of the Brillouin zone centers Γ in the HK0 plane. The very different sound velocities result in a large contrast in TDS intensities close to Γ for different directions. In fact, the TDS intensities scale $\approx 1/\omega^2$ close to Γ. Non-typical diffuse features features are observed in the HK2n+1 and HK2n reciprocal space sections:

(i) An asymmetry in diffuse scattering of individual features is observed in the HK2n+1 reciprocal space sections. It is most pronounced around the (211) reflection, see Figure 6.27. The HK2n+1 pattern as a hole are symmetric in agreement with the Laue symmetry of the system. The asymmetry of the diffuse scattering in the vicinity of the (211) reflections is further investigated by IXS measured at selected reduced momentum transfer q-values along the asymmetric TDS profile. IXS spectra are reported in Figure 6.28. Comparing the two pairs of experimental spectra at wave vectors with equivalent q one observes a difference in the integrated intensities corresponding to TDS and an energy shift of the main excitation. The calculation shows that the experimentally observed excitation contains the contribution of both Δ_4 and Δ_3 acoustic branches. The drastic change of spectral weight between the two branches leads to an energy shift of the envelope function. The Δ_4 optic branch, which is almost completely suppressed on one side, shows the same particularity.

(ii) A cross-like feature is observed around the almost forbidden reflections in the HK2 planes (these reflections become visible due to the asymmetry in the electron density distribution (Merisalo and Soininen, 1979)). IXS is used to clarify the nature of the cross-like TDS feature. IXS scans along [ξ ξ 2] are summarized in an intensity map in Figure 6.29. The inelastic intensity close to (0 0 2) is dominated

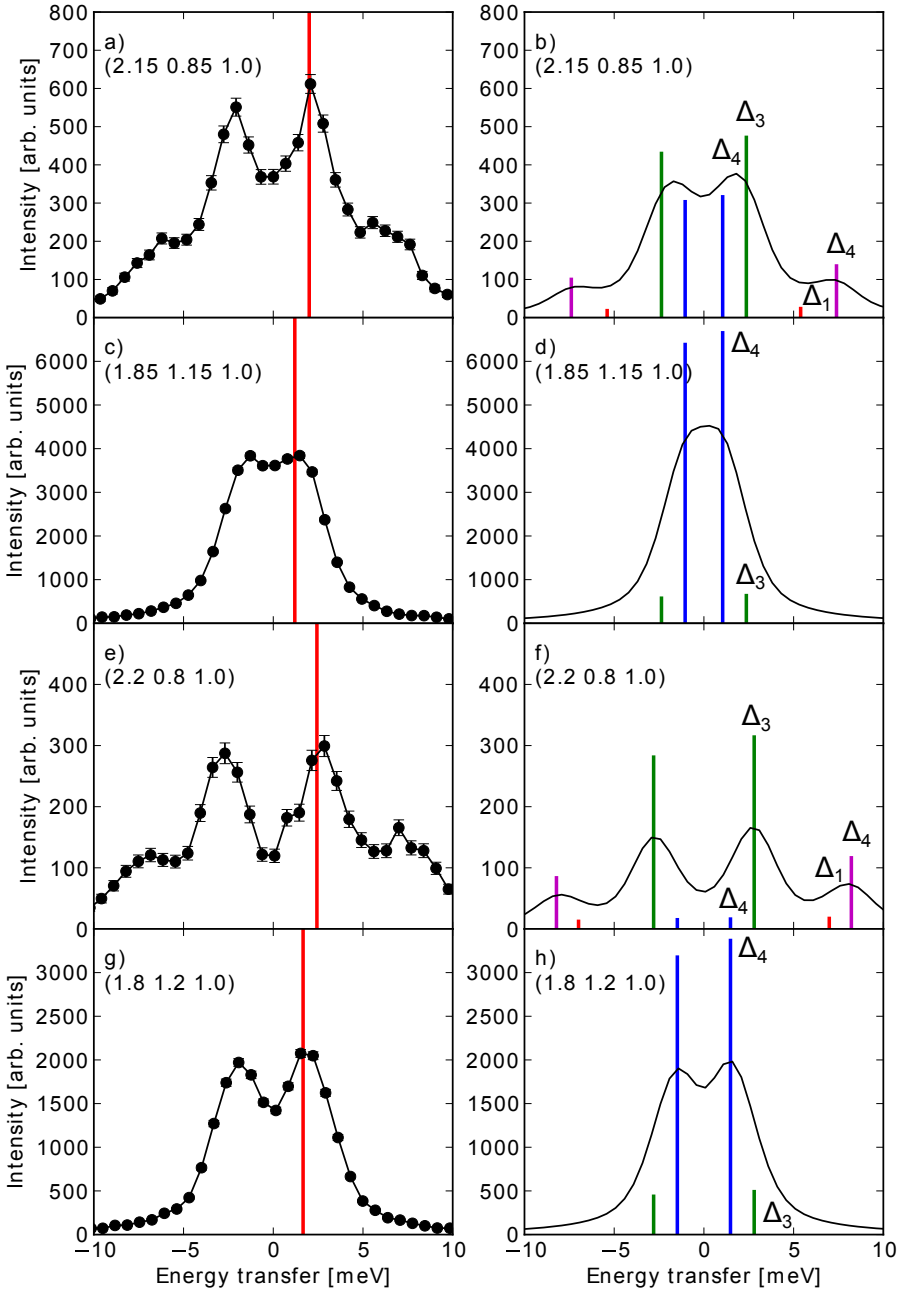

Figure 6.28: Experimental IXS spectra (left panels) of β-tin on different momentum transfers in the HK1 plane. The reduced momentum transfer q of panels a) and c) is equivalent, the same holds for panels e) and g). The peak position of the envelope function of the two acoustic branches is indicated by vertical lines in the experimental spectra. The inelastic contribution of the different branches (vertical lines) as obtained from the DFPT calculation and its convolution with the experimental resolution are shown for the corresponding momentum transfers in the right panels. The vertical lines are scaled by a factor 1/2 in respect to the convoluted spectra for best visualisation.

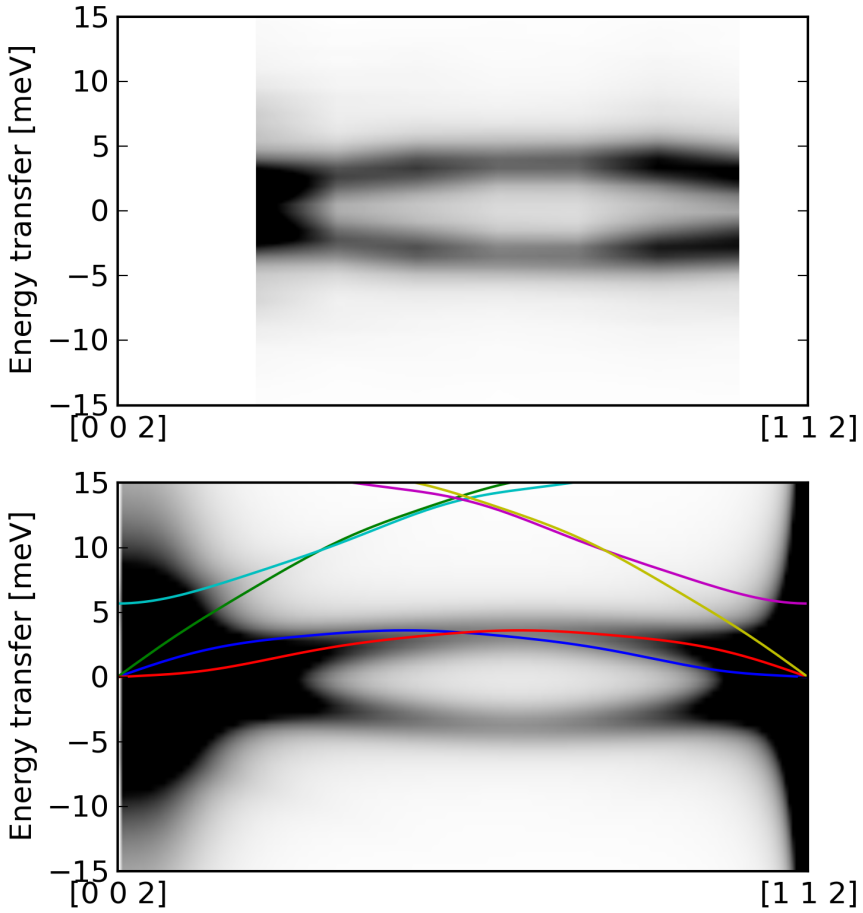

Figure 6.29: IXS intensity maps from (002) to (112) as obtained from experiment (upper panel) and calculation (lower panel). The experimental map consists of eight IXS spectra with a q-spacing of 0.1 r.l.u and 0.7 meV energy step, linearly interpolated to a 200×85 grid. The calculated IXS intensity is convoluted with the experimental resolution function of 3.0 meV full-width-half-maximum. The dispersion of the different branches is plotted as lines.

by the acoustic Δ_4 branch with a significant contribution of the optic Δ_4 branch, determined from the experiment at (0.1 0.1 2) to be 10.8 %. The intensity close to (1 1 2) is dominated by the acoustic Δ_3 branch with vanishing contribution of the optic Δ_4 branch. The intensity along [ξ 0 2] and [0 ξ 2] is suppressed. The diffuse features in the HK2n reciprocal space sections remain symmetric.

The measured phonon energies and IXS intensities are in good agreement with the calculation in the illustrated direction. The three-dimensional isosurface of diffuse scattering intensities, depicted in Figure 6.26 f), allows one to identify the shape of diffuse features. We note plate-like, elongated cross-like and asymmetric shapes. The topology of the diffuse scattering is in fact quite complex and its investigation requires a fine sampling of 3D reciprocal space. The inspection of only a few planes in reciprocal space may provide an incomplete picture, the authors of a previous study (Takahashi et al., 2006) could only identify rod-like features. The Fermi surface topology of β-tin is much more complex than in the case of zinc, where a directional tracing of the Kohn anomalies was undertaken (Bosak et al., 2009b). This is not possible in the case of β-tin, as the interaction of phonons with the conduction electrons is of complex nature and the anomalies in the dispersion curves are not sufficiently pronounced to allow a tracing of TDS anomalies. Furthermore, the complexity of the electronic system does not allow for an attribution of the anomalies to specific nesting geometries of the Fermi surface as it was possible for vanadium (Bosak et al., 2008).

The study on β-tin was extended to γ-tin. Calculated dispersion relations along high symmetry directions are compared to experimental results from INS (Ivanov et al., 1987) in Figure 6.30. The calculation describes the experimental results very well, including the phonon anomalies. Reciprocal space sections of diffuse scattering as obtained from experiment and calculated TDS are confronted to the results of β-tin in Figure 6.31. The diffuse scattering in γ-tin is almost perfectly reproduced by the calculation. The similarity of the compared TDS intensity distributions of β and γ-tin can be appreciated. It reflects the symmetry relation of the two phases which have common subgroups, consequently some symmetry elements are retained at the γ-β transition (Raynor and Lee, 1954). The vectorial relationship between the two structures is given by

$$\begin{pmatrix} \boldsymbol{a}_\beta \\ \boldsymbol{b}_\beta \\ \boldsymbol{c}_\beta \end{pmatrix} \approx \begin{pmatrix} -1 & 1 & 0 \\ 0 & 0 & 2 \\ 1 & 1 & 0 \end{pmatrix} \begin{pmatrix} \boldsymbol{a}_\gamma \\ \boldsymbol{b}_\gamma \\ \boldsymbol{c}_\gamma \end{pmatrix}, \tag{6.4}$$

where the vectors $\boldsymbol{a}$, $\boldsymbol{b}$ and $\boldsymbol{c}$ denote the unit cell vectors with corresponding indices for the β and γ phase. see Figure 6.32 for illustration. The phase transition is induced by the Γ-point mode in β-tin and the L-point mode in γ-tin (Ivanov et al., 1991). The Γ-H-M direction in β-tin for instance corresponds to the Γ-K-M direction in γ-tin. We note that the anomalies in the dispersion relation

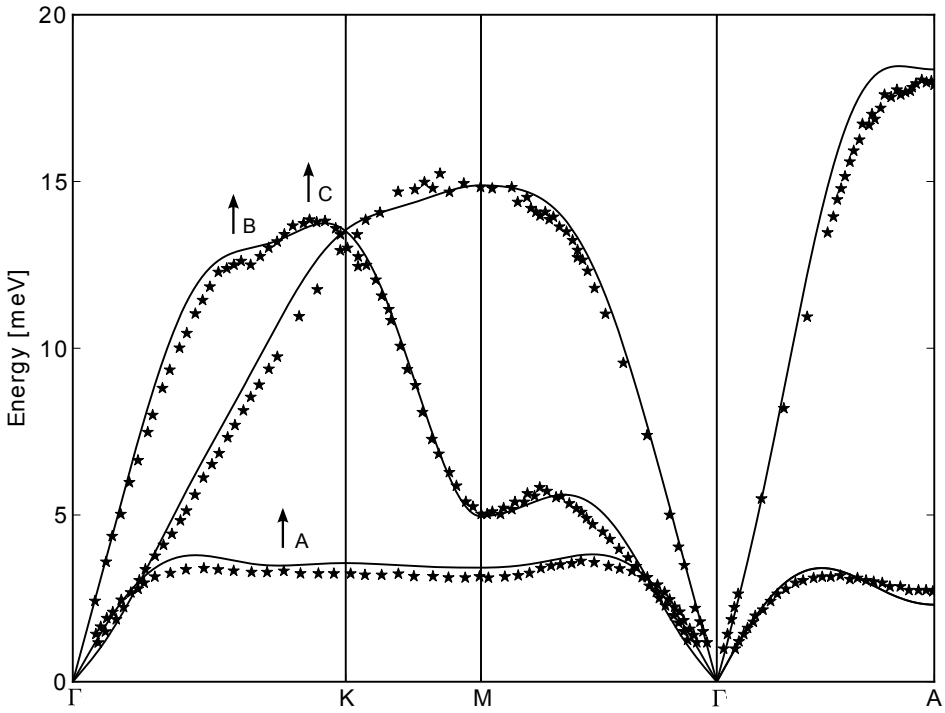

Figure 6.30: Phonon dispersion relations of γ-tin along the indicated high symmetry directions. The calculation (solid lines, pure Sn) is compared to experimental values of a $Sn_{0.8}In_{0.2}$ single crystal from (Ivanov et al., 1987) ($\star$). The labelled anomalies are discussed in the text.

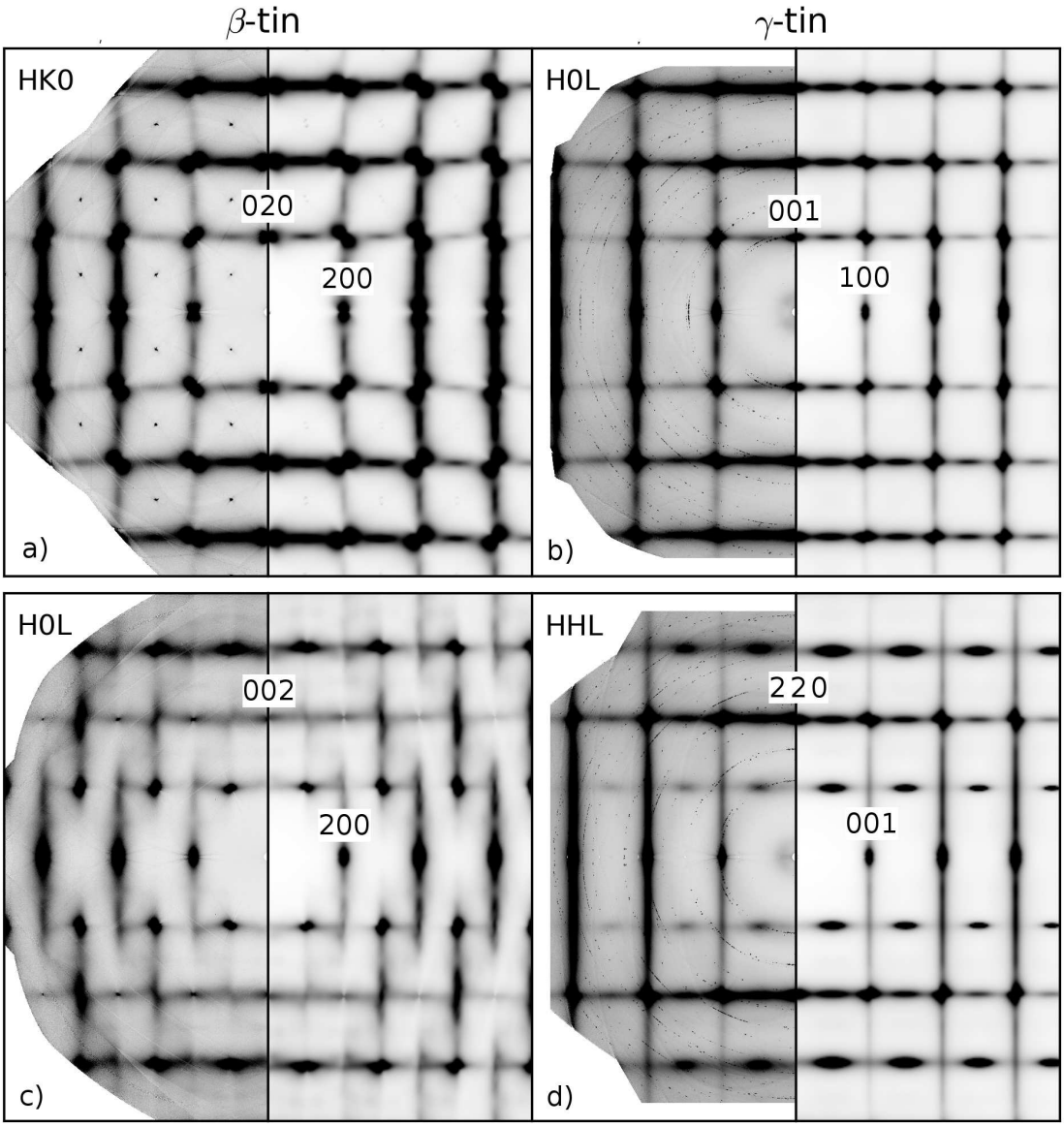

Figure 6.31: Experimental diffuse scattering (left part of individual panels) and calculated (right part of individual panels) TDS intensity distribution of β-tin (a) and (c) and γ-tin (b) and (d) in the indicated reciprocal space sections. The experimental TDS intensity distribution of γ-tin was obtained from a $Sn_{0.8}In_{0.2}$ single crystal, whereas the calculated one results from pure Sn.

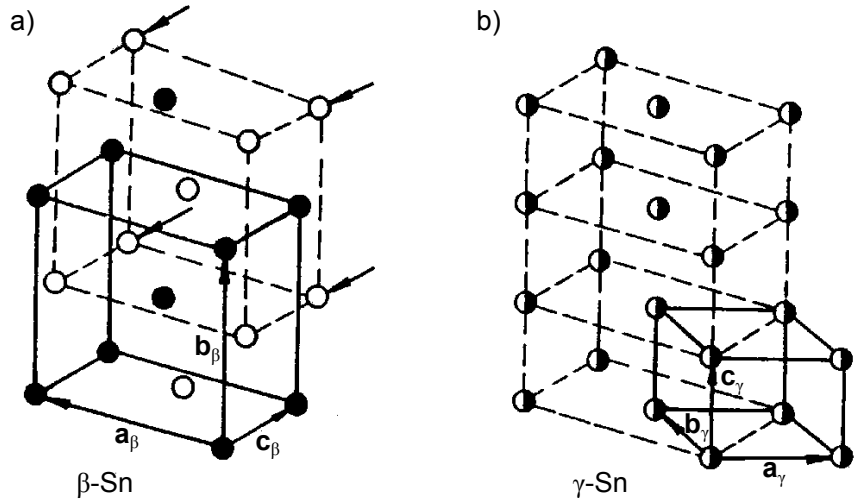

Figure 6.32: Structural relationship between β-tin (a) and γ-tin from Ivanov et al. (1991). The arrows indicated the directions of atomic displacements for β-tin (Γ-point mode) and for γ-tin (L-point mode). The full and open circles represent the atoms in the two different body-centered tetragonal sublattices of β-Sn.

labelled B and C (see Figure 6.30) appear at the same position as in β-tin, see Figure 6.25. The change in slope labelled A is less pronounced in γ-tin, resulting in a smoother intensity distribution of diffuse scattering. The structure of the two phases is different, the momentum transfer dependency of the underlying electronic potential is, however, similar. In fact the interatomic distances and force constants are very comparable in the two structures. A strong asymmetry in diffuse scattering as observed in the HK2n+1 reciprocal space sections in β-tin is not present in the γ-phase. The particularity in diffuse scattering in β-tin is thus a symmetry related feature.

Conclusions

We provide an accurate description of the lattice dynamics of the metallic tin β and γ polymorphs. It was shown that the diffuse and inelastic scattering from phonons can be described to a good approximation in the frame of one-phonon scattering within the harmonic approximation. The observed features are reproduced in great detail by DFPT at arbitrary momentum transfers. The strong influence of the electron subsystem on inter-ionic interactions causes anomalies in the phonon dispersion relations. An unusual asymmetry of thermal diffuse scattering is observed in β-tin which is related to the non-symmorphic structure. The comparison of TDS from β- and γ-tin reveals a strong resemblance and reflects

the symmetry relation between the two structures and a strong similarity of the underlying potential.

6.5 Ice

Single crystals of natural ice-Ih, extracted from the subglacial Vostok lake accretion ice layer (Antarctic) were investigated by means of diffuse and inelastic x-ray scattering. The diffuse scattering was identified as mainly inelastic and rationalised by an *ab initio* lattice dynamics calculation for ordered ice (XI phase). A Monte-Carlo simulation was used to model the static disorder contribution to the diffuse scattering and allowed to reconsider previously published data of neutron diffuse scattering on heavy ice as the sum of thermal diffuse scattering and static disorder contribution. The experiment illustrates nicely the sensitivity of inelastic x-ray scattering to the hydrogen.

Introduction

In the ice-Ih phase the oxygen atoms are arranged in a wurzite structure, and the hydrogen atoms are placed randomly in one of the two energy minima in between each pair of oxygens while only two nearest neighbours are allowed (Bernal and Fowler, 1933, Pauling, 1935). The average structure is hexagonal with space group $P6_3/mmc$. It is the only ice phase existing in the crust. At temperatures below 72 K an ordered structure (ice XI) becomes stable. The hydrogen ordering reduces the symmetry from hexagonal to orthorhombic ($Cmc2_1$). The dynamical properties of ice have been subject of many experimental and theoretical studies, see Section 1.4, but a quantitative study of diffuse scattering in H_2O ice Ih has not been reported.

Here we investigate natural single crystal ice-Ih samples, extracted from the subglacial Vostok lake accretion ice layer at a depth of 3621 m and cut from the core - kindly provided by V. Ezhov and S. Bulat (St. Petersburg Nuclear Physics Institute). The expedition was primarily undertaken to reconstruct past climate variations (Petit et al., 2005). In parallel, the ice core was studied to understand how microbial cells could survive for long time periods at deep subfreezing temperatures (Abyzov, 1993). The characteristic grain size for crystals from this accretion is reported to be approximately 1 m. Diffuse and inelastic x-ray scattering are the instruments of experimental work while *ab initio* lattice dynamics calculations and Monte-Carlo modelling are used to rationalise the results.

Experimental methods

The crystals were gently shaped by a scalpel blade to rod-like samples of about 2 mm in diameter. They were glued by a water drop to a sample holder made out of glass, mounted on a rotation stage and cooled by a nitrogen cryostream. The temperature was keept at 175 ± 1K. The sample was etched prior to the measurement by cold methanol, resulting in a smooth and transparent surface. The crystalline

quality was verified by x-ray diffraction at the Swiss-Norwegian Beamlines at the ESRF (BM01A). The pilot diffuse scattering measurements were performed by A. Bosak and D. Chernyshov at BM01A using a mar345 detector (Marresearch GmbH). The follow-up experiment was performed at beamline ID29 at the ESRF, where the diffuse scattering patterns were collected with a PILATUS 6M detector (Kraft et al., 2009). The crystals were in both cases exposed to monochromatic X-rays with a wavelength of 0.700 Å. The sample was rotated orthogonal to the beam direction over an angular range of 360° and diffuse scattering patterns were recorded in transmission geometry. The orientation matrix was refinement using the CrysAlis software package (Oxford diffraction Ltd.). For the final reciprocal space reconstructions we applied corrections for polarisation and for solid angle conversion associated with the planar projection. All the test samples were found to be good quality single crystals, showing narrow rocking curves. The absence of diffuse streaks indicates that the crystals are largely stacking-fault free.

The IXS experiment was performed on beamline ID28 at the ESRF. The instrument was operated at 17.794 keV, providing an overall energy resolution of 3.0 meV FWHM. The momentum transfers were chosen by an appropriate setting of the scattering angle and the crystal orientation in the horizontal scattering plane. The momentum resolution was set to $\approx$0.25 nm^{-1} $\times$ 0.75 nm^{-1} in the horizontal and vertical plane, respectively. Further details of the experimental setup can be found in Chapter 4. IXS measurement were performed at constant momentum transfer with an exposure time of $\approx$20 s per energy point.

Calculations

Different approaches of *ab initio* electronic structure calculations for ice-Ih have been proposed (Kuo et al., 2005) and a lattice dynamics calculation following the proposed approximation is in principle possible. However, such calculations are very demanding. We circumvent this difficulty to some extend, using ordered ice XI (Jackson et al., 1997). Such an approximation appears to be valid in reasonable extend in terms of oxygen dynamics, and provides some insight into the hydrogen dynamics and its contribution to the scattering.

The *ab initio* lattice dynamics calculation of H_2O ice-XI was performed using DFPT (Gonze and Lee, 1997) as implemented in the CASTEP code (Clark et al., 2005, Refson et al., 2006). In contrast to the calculations performed on the silica and tin polymorphs the use of a general gradient approximation in the Perdew-Burke-Ernzhof regime (Perdew et al., 1996) was found to be most appropriate for the accurate description of the bond lengths. The calculations were performed in the plane-wave formalism using norm conserving pseudo-potentials form the Bennett & Rappe Pseudo-potential Library (Bennet and Rappe). The geometry was optimised on a $7 \times 7 \times 4$ Monkhorst-Pack grid with a plane wave cut-off energy of

820 eV, ensuring the convergence of internal forces to <10−3 eV/Å. The relaxed lattice parameters for H_2O ice XI with space group $Cmc2_1$ are a = 4.396 Å, b = 7.654 Å and c = 7.188 Å. These values correspond to a ≈ 6% smaller volume than experimentally determined for D_2O ice XI. Indeed, replacing hydrogen by deuterium causes a volume increase due to anomalous nuclear quantum effects, which are well described within density functional theory (Pamuk et al., 2012). The lattice dynamics calculation of D_2O was performed using the same pseudo-potentials and lattice parameters as for light ice XI, thus neglecting these effects. The dynamical matrix was computed on a $5 \times 5 \times 4$ Monkhorst-Pack grid by perturbation calculation and further Fourier interpolated for the calculation of TDS and IXS intensities. The scattering intensities were computed in first order approximation using in house developed software. The lattice parameters were rescaled to the experimental lattice parameters of ice Ih and the O-H bond length was brought to the value 0.95Å by the translation along the O-O direction for the calculation of the x-ray patterns. The stretching value is justified by x-ray diffraction. Individual Debye-Waller factors were calculated from the dynamical matrix and averaged over all positions of the same atomic species in order to produce isotropic values. The temperature dependence of the averaged Debye-Waller factors is shown in Figure 6.33. Due to the difference in mass the values for deuterium atoms are smaller than for hydrogen. A slight difference of the the Debye-Waller factors for the oxygen atoms in the two environment is also noticeable. The calculated values for oxygen are about 20% smaller then experimentally observed (Kuhs and Lehmann, 1986) at low temperatures but deviate by ca. 60% at 220K. The deviation at high temperature may partly be explained by anharmonic contributions.

Monte Carlo simulations were performed by A. Bosak to model the static component of the diffuse scattering. 128 fully disordered model clusters were generated starting from 64 × 64 × 64 cells of ice XI crystals which contained in total 2^{22} protons. These model clusters produced a sufficiently large number of self-closed random walks and guarantee thus Pauling's model (Pauling, 1935). Cyclic boundary conditions were imposed and closed walks were preferred to prevent the creation of residual (charged) defects. The static disorder of oxygen atoms was taken into account by displacing the oxygen atoms are displaced along the H-O-H angle bissectrix by 0.05 Å in consistence with experimental and theoretical values (Kuhs and Lehmann, 1986, Kuo et al., 2005). The intensity of total scattering, normalised per formula unit, is calculated as

$$I(\boldsymbol{Q}) \approx I_{TDS}(\boldsymbol{Q}) + I_{stat}(\boldsymbol{Q}) \tag{6.5}$$

where

$$I_{TDS}(\boldsymbol{Q}) = \frac{\hbar}{Z_{dyn}} \sum_j \frac{1}{\omega_{\boldsymbol{Q},j}} coth\Big(\frac{\hbar\boldsymbol{\omega}_{\boldsymbol{Q},j}}{2k_BT}\Big) | \sum_s \frac{f_s}{\sqrt{m_s}} e^{-M_s} (\boldsymbol{Q}\boldsymbol{e}_{\boldsymbol{Q},j,s}) e^{-i\boldsymbol{Q}\boldsymbol{\tau}_s} |^2. \tag{6.6}$$

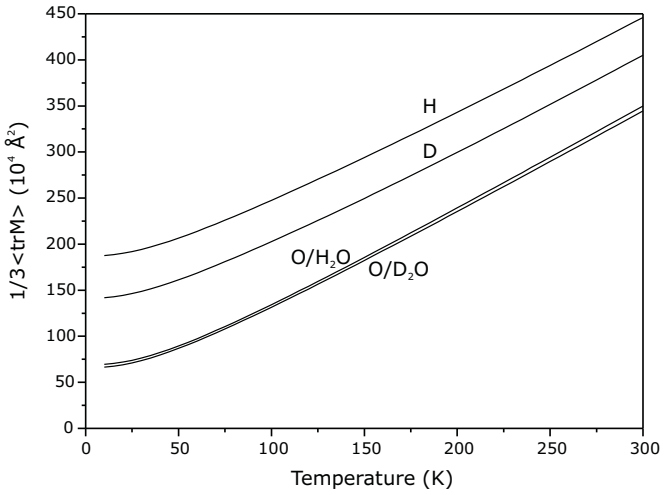

Figure 6.33: Temperature dependence of the calculated Debye-Waller factors for the different species in H_2O and D_2O ice XI polymorphs.

is the TDS intensity and

$$I_{stat}(\boldsymbol{Q}) = \frac{1}{Z_{stat}} |\sum_s f_s e^{-M_s - i\boldsymbol{Q}\boldsymbol{\tau}_s}|^2 \tag{6.7}$$

corresponds to the contribution of disorder. Z_{dyn} is the number of formula units in the primitive cell (4 for ice XI) and Z_{stat} is the total number of formula units used in the simulation (here 2^{28}).

Results and discussion

Experimental diffuse scattering intensity distributions in high symmetry reciprocal space sections are compared to *ab initio* calculated TDS and previously published semi-quantitative data (Owston, 1949) in Figure 6.34. We note a very structured intensity distribution and an excellent agreement between experiment and calculation. All features are well described. The experimental results are in agreement with the (incomplete) data from 1949, which shows that despite the limitations of the technique at that time the data were of good quality. From the resemblance of the diffuse scattering with TDS we can conclude that at least for the low-energy modes - which contribute most to the TDS intensity due to the ω^2-dependence in the long wavelength limit - the *ab initio* calculation of the proton-ordered ice XI describes quite well the dynamics of ice Ih both in terms of eigenvalues and eigenvectors of the oxygen atoms.

The static disorder contribution to the diffuse scattering as computed from the Monte Carlo simulation is compared to experimental diffuse scattering in Figure

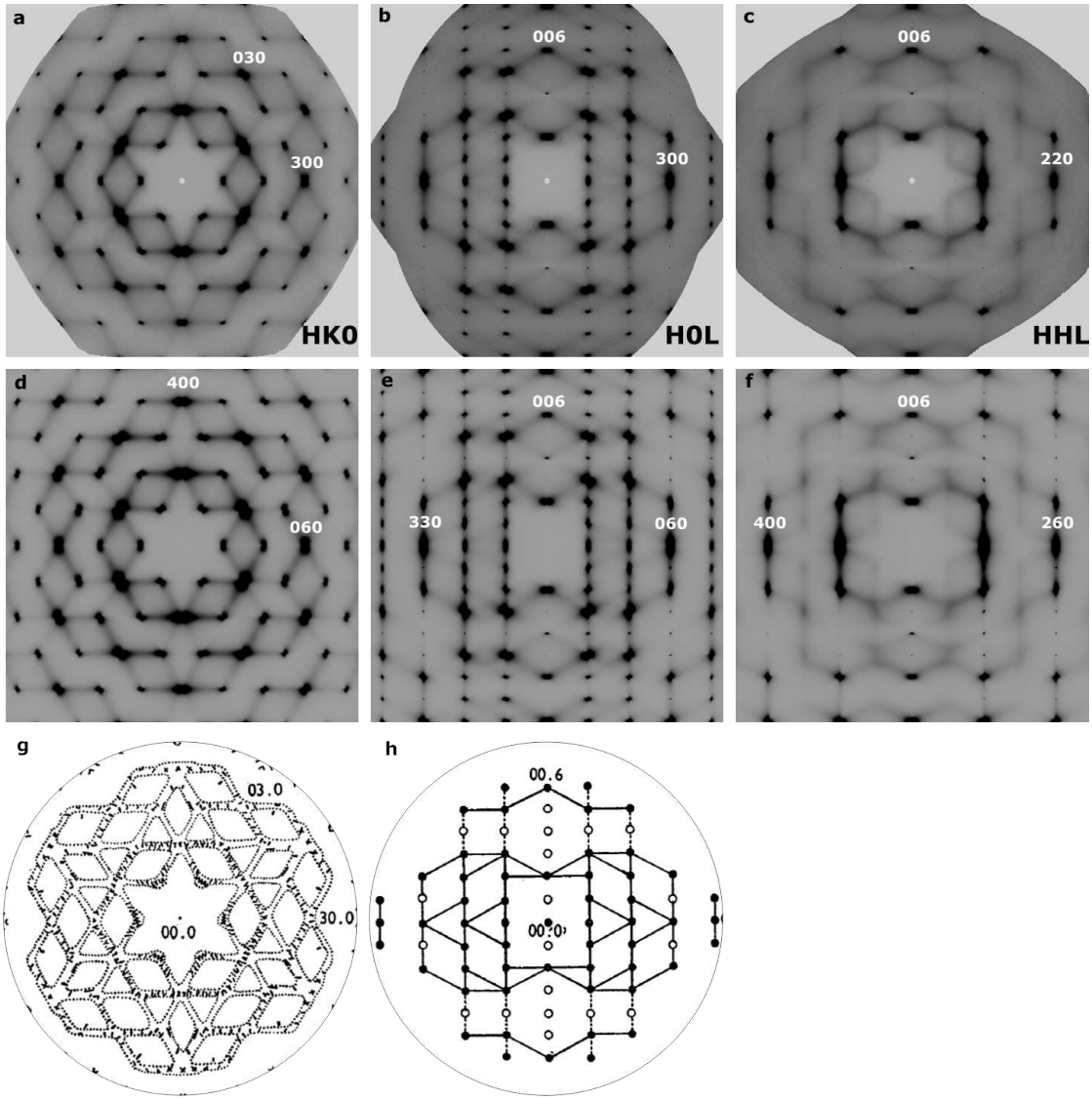

Figure 6.34: Diffuse x-ray scattering intensity distributions of crystalline H_2O ice Ih at 175 K (a, b, c) compared to the *ab initio* calculation for the ice XI approximant (d, e, f). For the cell relationships see Figure 6.35 c. Note the inequivalence of left and right halves of panels (e) and (f) and the absence of a six-fold axis in panel (d). (g) and (h) show the semi-quantitative data from Owston (1949).

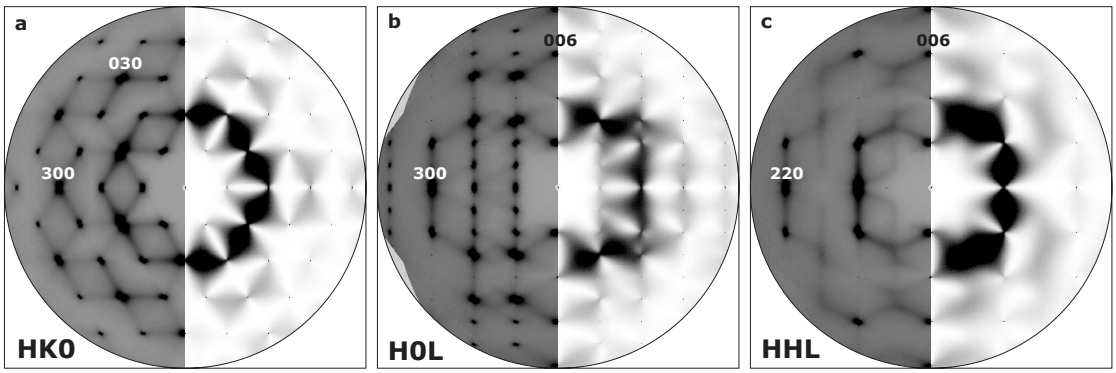

Figure 6.35: Diffuse x-ray scattering intensity distributions of H_2O ice Ih at 175 K (left part of individual panels) compared to the calculated static x-ray contribution (right part of individual panels) for the indicated reciprocal space sections.

6.35. The intensity of the calculated patterns is magnified for best visualisation of the diffuse features. The absolute contribution of static disorder is very weak compared to TDS. We note that the regions with small contribution from static disorder roughly coincide with the minima of TDS. Consequently, there is no region where the static component could be observed separately.

Selected directions in reciprocal space were investigated by IXS and compared to the calculation in Figure 6.36. We note that the intensity distribution is well described by the calculation. The relationships between the hexagonal and orthorhombic unit cell are illustrated in Figure 6.36 c). Note that the [ζ ζ 0] and [0 ζ 0] directions in ice XI become degenerate in ice Ih. The experimental intensity map Figure 6.36d) can be described by the average of the intensities of the two directions in ice XI, except for $(2\ 0\ 0)_h$ point. The measured phonon energies are systematically lower than the calculated ones for ice XI. The presented IXS maps provide the only available data on experimental phonon dispersions of H_2O ice and serve as proof that the lattice dynamics in the low energy region of ice Ih can be described in good approximation by the lattice dynamics of the ordered phase.

A detailed inspection of the calculated TDS maps in Figure 6.34 reveals some asymmetry in the scattering intensity distribution and the absence of the six fold symmetry in the HK0 plane, which is again due to the difference in structure. The asymmetry of scattering intensity in the proximity of the (004) reflection and, to some extent in the proximity of the other reflections in the HK4 layer, is due to the hydrogen contribution to the scattering factor, as illustrated in Figure 6.37. The TDS intensity distribution of the H0L plane of ice XI (corresponds to HHL in ice Ih) is calculated with and without the contribution of hydrogen scattering. The scattering around the (004) reflection disappears if the hydrogen contribution is neglected. Diffuse scattering around this reflection is indeed observed, see Figure

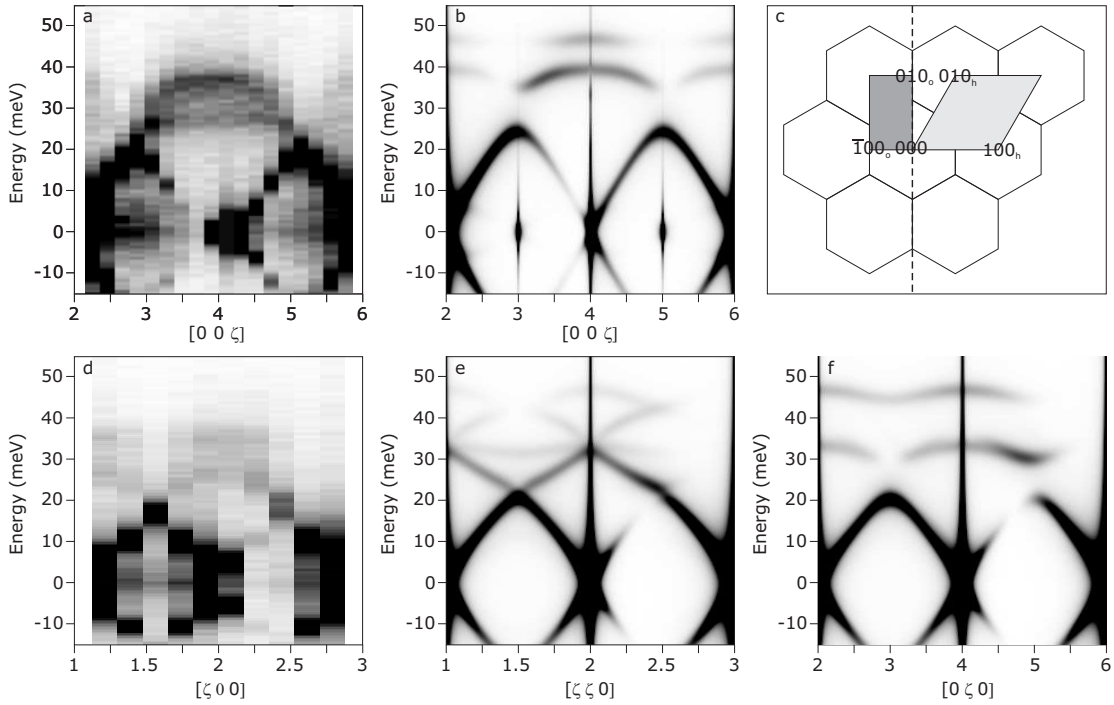

Figure 6.36: Measured (a, d) IXS intensity maps of H_2O ice Ih at 175 K together with the corresponding calculated IXS map for ice XI (b, e, f) along the indicated directions in reciprocal space (b, e, f). Both (e) and (f) correspond to (d) as these directions become degenerate in the disordered Ih phase. Panel (c) illustrates the relationships between the hexagonal unit cell of Ih ice (index h) and the orthorhombic unit cell of ice XI (index o).

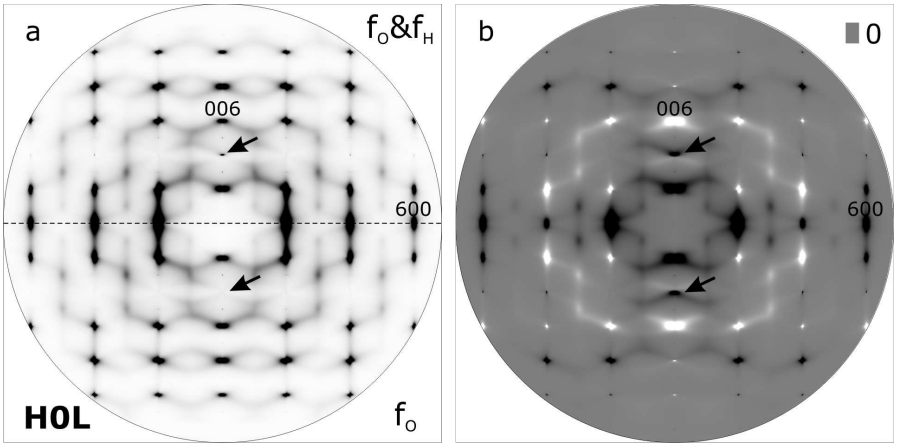

Figure 6.37: (a) TDS intensity distribution in the H0L plane calculated for ice XI (equivalent to the HHL plane in ice Ih) at 175 K using both hydrogen and oxygen scattering factors (upper part) and oxygen scattering factor only (lower part). (b) Difference between the two maps of panel (a). The intensity difference is multiplied by a factor four. Zero difference is projected to gray, negative difference is lighter and positive difference darker. Arrows point towards the region of interest around the (004) reflection.

6.34b). The observation that IXS and TDS are sensitive to the scattering from hydrogen is not fully unexpected, but can be considered as non-trivial experimental observation.

The Monte Carlo simulation for the static contribution to the diffuse scattering arising from hydrogen disorder and the *ab initio* calculation of D_2O ice were used for the revision of published neutron scattering data (Li et al., 1994). Previously, the experimental patterns were modelled via reverse Monte Carlo procedure (Beverley and Nield, 1997). The authors had to include an additional frozen-in displacement to mimic the thermal diffuse scattering. With the help of the *ab initio* calculation we can evaluate the observed scattering as the sum of TDS and a disorder-related component. The result is illustrated in Figure 6.38, where the experimental data from (Li et al., 1994) is compared to the intensity distribution arising from TDS, the static contribution, and to the sum of the two. We clearly note that the contribution from static hydrogen disorder, which is exclusively governed by the ice rules, contributes much stronger to neutron scattering than to x-ray scattering, but despite the low temperature of 10 and 20 K the contribution from TDS remains significant. Taking into account both contributions the neutron scattering is very well described. This proves that Pauling's model remains a very good approximation in the description of ice.

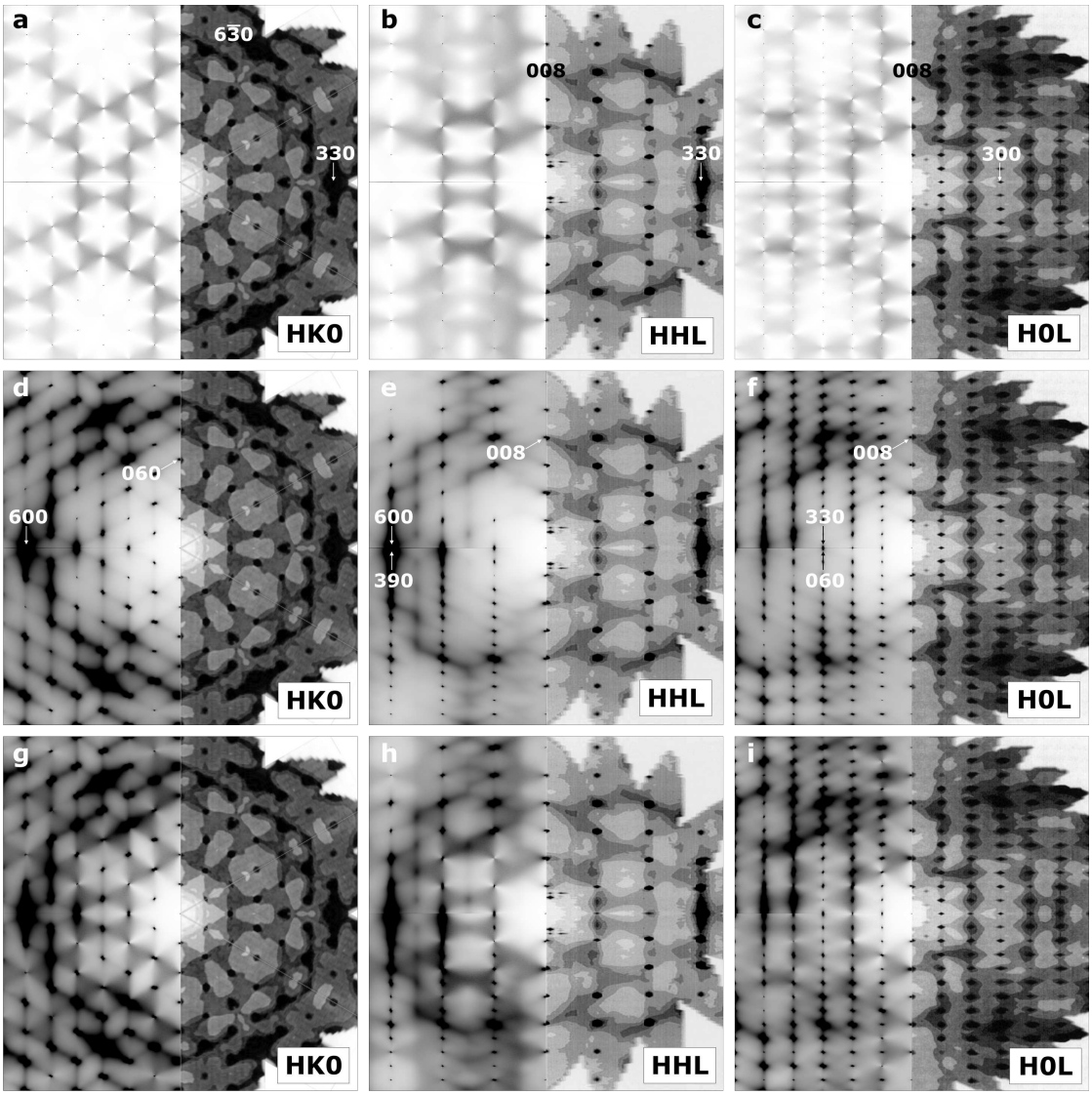

Figure 6.38: Diffuse neutron scattering intensity distribution measured by Li et al. (1994) for Ih ice crystal in the indicated reciprocal space sections (right part of individual panels). The temperature was 10 K for the HK0 plane and 20 K for H0L and HHL planes. The diffuse scattering intensity distribution is compared to the calculated contribution from static displacements of hydrogen atoms only (a, b, c), TDS only (d, e, f), and static displacement plus inelastic component (g, h, i). The calculated TDS intensity distributions are divided in two sub-panels. The upper and lower parts show separately the contribution of two planes in ice XI which become degenerate in ice Ih. The same intensity scale is applied for all calculated intensity distributions.

Conclusions

In summary, we have shown that the x-ray diffuse scattering in ice Ih is almost entirely due to TDS and can be well described by the lattice dynamics of the ordered ice XI polymorph. Despite the fact that the measured low energy part of the dispersion relations in high symmetry directions is lower than the calculated one for ice XI, we note a good agreement of measured and calculated intensities. This implies that the phonon eigenvectors of the low energy branches must be similar in both ordered and disordered ice, in particular for the oxygen atoms. Within the discussed assumptions, our model provides valuable information, for example, for the estimation of purely phonon Debye-Waller factors and separation of the disorder contribution (so called 'static Debye-Waller factor'). We furthermore notice that IXS and, obviously, TDS are sensitive to the scattering arising from the hydrogen atoms. The calculation strategy for the static disorder contribution allowed us to model neutron diffuse scattering as the sum of thermal diffuse scattering and disorder component which is exclusively governed by Pauling's ice rules. The numerical recipes can be transferred to numerous frustrated systems; see Section 7.1 for further discussion.

Chapter 7

Conclusions and Outlook

This chapter evaluates the applied methodology of combining TDS, IXS and *ab initio* lattice dynamics calculations and concludes system specific results. The impact of the actual study and future trends are discussed.

7.1 Conclusions

Based on the benchmark studies performed on the silica polymorphs α-quartz, coesite and α-cristobalite, germanium dioxide in α-quartz structure, the tin β- and γ- polymorphs and ice Ih we have seen that the combination of TDS, IXS and *ab initio* lattice dynamics calculations provides a powerful tool in the study of lattice dynamics of crystals. TDS experiments can serve as a rigorous benchmark for parameter-free calculations even for relatively complex structures, in particular if they are complemented with IXS on powder, single crystals or both of them. It is thus possible to recover the full description of the lattice dynamics (in harmonic approximation). Characteristic features in the lattice dynamics can be localised by the inspection of TDS intensity distributions in 3D reciprocal space. Selected regions are further investigated by an energy resolved measurement employing IXS. The full set of experimental data is then confronted to the calculation. Thus validated calculation allows for a detailed analysis of interesting features in the lattice dynamics, not only in terms of phonon energies, but also accessing the phonon eigenvectors. For the systems under investigation both TDS and IXS intensities can be convincingly described in the frame of one-phonon scattering within harmonic approximation, including characteristic details in the fine structure. The implementation of an appropriate 2D pixel detector for TDS studies at the IXS spectrometer ID28 (ESRF) allows the combined study of IXS and TDS for the same sample position in delicate sample environments, involving high pressure cells, cryostats, laser heating, etc. System-specific results are summarised in the

following.

Silica polymorphs

The extended studies of the silica polymorphs α-quartz, coesite and α-cristobalite were conducted with particular interest on the first peak in the vibrational density of states. The combination of TDS, IXS and lattice dynamics calculations from first principles were used for the study of the lattice dynamics at arbitrary momentum transfers. The VDOS, obtained from powder IXS spectra, probes the ensemble of vibrational states and was used to determine an overall scaling factor for the *ab initio* calculation. The application of a nearly identical linear scaling factor of a few percent for all tetrahedral coordinated silica polimorphs leads to a very good agreement between *ab initio* calculated and measured phonon energies. The recovery of the full lattice dynamics allowed for the localisation of the critical points responsible for Van Hove singularities and the attribution of their vibrational character and the topology in energy-momentum space. With the help of the calculations decisive conclusions for lattice dynamical features in the relatively complex structure of the silica polymorphs could be drawn.

The first peak in the VDOS is located at different energies for the three silica polymorphs. Quite remarkable, the critical points responsible for the first peak are located at the zone boundary in the case of all three silica polymorphs under investigation. For α-quartz and germanium dioxide in α-quartz structure the same point in reciprocal space is responsible for the first peak. The topology of the energy surface in the vicinity of the critical points is different, but despite this, the associated displacement patterns are very similar: The largest displacement is observed for oxygen. The vibration consists mainly of a tetrahedron tilt, accompanied by a small distortion. The study from Chumakov et al. (2013) revealed that the numbers of excess states above the Debye levels in the VDOS of ambient silica glass and α-cristobalite are very similar and that the excess states for both glass and crystal are located nearly at the same energy. The same is true for densified glass and α-quartz, if the densities are matched. Taking into account the similarity observed in the displacement patterns of the investigated three silica polymorphs we can now conclude, that the vibration causing the Boson peak in silica glass must be similar as well on a local scale.

In the framework of the silica polymorphs we are now able to provide accurate models of the lattice dynamics of α-quartz, coesite, α-cristobalite and stishovite (Bosak et al., 2009a). The calculation for these polymorphs can be extended to high pressures and allow the derivation of thermodynamical properties. The prediction of the lattice dynamics for new high pressure phases like seifertite and others (Dubrovinsky et al., 2004) should be possible within the employed calculation scheme.

Metallic tin polymorphs

For the tin polymorphs a strong resemblance of the diffuse scattering intensity distribution in β- and γ-tin was observed. The similarity reflects the symmetry relation between the two phases and also shows the strong similarity of the underlying electronic potential. The non-centrosymmetric environment of atoms in β-tin results in a non-typical asymmetry of thermal diffuse scattering. The strong influence of electron subsystems on inter-ionic interactions creates anomalies in the phonon dispersion relations in β- and γ-tin. The complex electron phonon coupling is nevertheless properly accounted for by the calculation.

Ice

New data on the lattice dynamics of H_2O ice Ih were obtained by the investigation of natural ice single crystals from the subglacial Antarctic Vostok lake accretion layer. X-ray diffuse scattering was found to be almost entirely due to TDS and can be well described by the *ab initio* lattice dynamics of the ordered ice XI polymorph. The study illustrated that IXS and, obviously, TDS are sensitive to the scattering arising from the hydrogen atoms. A Monte Carlo simulation corresponding to Pauling's model was used to model the static disorder component to the diffuse scattering. This component becomes important in neutron scattering and the two models together were successfully used to reanalyse previously published data on diffuse neutron scattering on ice Ih. The numerical recipes used for the calculation of static disorder contributions can be transferred to a number of frustrated systems, starting from so called spin ices with pyrochlore structure and beyond.

7.2 Future prospectives

The combined approach of TDS, IXS and lattice dynamics calculations can be applied to a broad class of crystalline systems with interesting lattice dynamics features. These comprise for example charge density wave systems, superconductors, multiferroics, relaxors and materials at extreme pressure. In particular promising is the extension to extreme pressures. X-rays can be focused to a few microns thus IXS studies on high pressures using diamond anvil cells become feasible (Antonangeli et al., 2004, Farber et al., 2006). Pressures up to ≈ 1 Mbar can be applied and combined with very high or low temperatures (Antonangeli et al., 2008, Leroux et al., 2012). The full reconstruction of the lattice dynamics may not be possible, due to geometrical constraints imposed by the sample environment and Compton scattering if diamond anvil cells are used. Of interest for Earth and Planetary science is the possibility to determine the elastic constants from TDS measurements under high pressure and high temperature.

The methodology may be also extended to lattice dynamics studies beyond the harmonic approximation, for example melting processes or non-equilibrium phonons (McWhan et al., 1982, Trigo et al., 2010).

Diffuse neutron and diffuse x-ray scattering techniques can be as complementary as INS and IXS are. For example, the combination of INS and IXS provides a unique technique to separate inelastic scattering arising from magnons and phonons.

Conclusions

7.3 Conclusions (français)

En se basant sur les études de systèmes de référence tels que les polymorphes de silice α-quartz, coésite et α-cristobalite, les polymorphes de l'étain en phase β et γ, et la glace Ih, nous avons constaté que la combinaison de la TDS, IXS et des calculs *ab initio* s'avère être un outil puissant dans l'étude de la dynamique de réseaux de monocristaux. Les expériences de la TDS peuvent servir de référence fiable pour les calculs de premier principes, même pour des structures relativement complexes, en particulier s'ils sont complétés par des études IXS sur la poudre, sur des monocristaux ou sur les deux. Il est alors possible de récupérer la description complète de la dynamique de réseau (en approximation harmonique). L'analyse des distributions en intensité de la TDS en 3D dans l'espace réciproque permet de localiser des caractéristiques de la dynamique de réseau. Certaines régions de l'espace réciproque sont sélectionnées pour une mesure IXS haute résolution en énergie. L'ensemble des données expérimentales est alors confronté aux calculs. Ceux-ci alors validés, permettent une analyse détaillée des caractéristiques essentielles de la dynamique de réseau, non seulement en termes d'énergies de phonons, mais également en termes de vecteurs propres. Pour les systèmes de référence on peut constater que les intensités TDS et IXS peuvent être décrites en bonne estimation dans le cadre de la diffusion de première ordre en approximation harmonique, y compris la finesse des détails caractéristiques.

La mise en œuvre d'un détecteur à pixels hybride bidimensionnel adapté pour les études TDS sur le spectromètre IXS (la ligne de lumière ID28 à l'ESRF) permet l'étude combinée d'IXS et TDS à la même position pour l'échantillon. De cette manière, les variations de la dynamique de réseau sur des stimuli externes (température et pression) peuvent être étudiées aux environnements d'échantillons délicats, comme des cellules à haute pression, cryostats, chauffage laser, etc.

Les résultats spécifiques pour les systèmes de références sont résumés en détail dans la version anglaise.

Les principaux résultats pour les polymorphes de silice sont : l'identification de l'origine du premier pic dans la densité d'états vibrationnels pour tous les poly-

morphes, ainsi que la mise en évidence d'une forte similarité entre les polymorphes. Le premier pic dans la VDOS est situé à différentes énergies pour les trois polymorphes de silice. Tout à fait remarquable, les points critiques responsables pour ce pic sont situés au bord de la zone Brillouin. La topologie de la surface d'énergie au voisinage des points critiques est différente, mais malgré cela, les modes de déplacement associés sont très semblables: le plus grand déplacement est observé pour l'oxygène. Les vibrations correspondent principalement a une inclinaison tétraédrique, accompagnée d'une petite distorsion.

Pour les polymorphes d'étain, on observe une forte ressemblance de la distribution des intensités TDS. Celle-ci reflète la relation de symétrie des deux phases et la similarité dans le potentiel électronique. L'environnement non-centrosymétrique des atomes entraîne une non-habituelle asymétrie de distribution des intensités TDS.

L'étude de la glace révèle que la diffusion diffuse des rayons X est presque entièrement due à la TDS et peut être décrite par les calculs *ab initio* relatant la dynamique de réseau pour la glace (ice XI). L'étude a montré que IXS et, évidemment TDS, sont sensibles à la diffusion provenant des atomes d'hydrogène La diffusion diffuse de neutrons - déjà publié - peut être modélisée par la somme de TDS (définie approximativement de la glace en phase XI) et d'une contribution provenant du désordre d'hydrogène.

Une perspective pour de futures applications est présentée en détail dans la version anglaise. La méthodologie proposée peut être appliquée à une large classe de systèmes cristallins avec une dynamique de réseau intéressante, par exemple des supraconducteurs, des systèmes d'onde de densité de charge, des multiferroiques, relaxeurs et des matériaux à la pression extrême, etc. Ces études peuvent être étendues sur les échantillons dans des conditions extrêmes en température et en pression et sur l'étude de la dynamique de réseau anticipant l'approximation harmonique. L'usage combiné de rayons X et de neutrons est également une option intéressante.

Bibliography

S. S. Abyzov. Microorganisms in the antarctic ice. In E. Friedmann, editor, *Antarctic Microbiology*, pages 265–295. Wiley-Liss, New York, 1993.

W. A. Adeagbo, A. Zayak, and P. Entel. Ab initio study of the structure and dynamical properties of crystalline ice. *Phase Transitions*, **78**(1-3):179–196, 2005. doi: 10.1080/01411590412331316609.

R. J. Angel, C. S. J. Shaw, and G. V. Gibbs. Compression mechanisms of coesite. *Phys. Chem. Miner.*, **30**(3):167–176, 2003. doi: 10.1007/s00269-003-0303-9.

C. A. Angell. Formation of glasses from liquids and biopolymers. *Science*, **267** (5206):1924–1935, 1995. doi: 10.1126/science.267.5206.1924.

N. Antolin, O. D. Restrepo, and W. Windl. Fast free-energy calculations for unstable high-temperature phases. *Phys. Rev. B*, **86**:054119, 2012. doi: 10.1103/PhysRevB.86.054119.

D. Antonangeli, M. Krisch, G. Fiquet, D. L. Farber, C. M. Aracne, J. Badro, F. Occelli, and H. Requardt. Elasticity of cobalt at high pressure studied by inelastic x-ray scattering. *Phys. Rev. Lett.*, **93**:215505, 2004. doi: 10.1103/PhysRevLett.93.215505.

D. Antonangeli, M. Krisch, D. L. Farber, D. G. Ruddle, and G. Fiquet. Elasticity of hexagonal-closed-packed cobalt at high pressure and temperature: A quasiharmonic case. *Phys. Rev. Lett.*, **100**:085501, 2008. doi: 10.1103/PhysRevLett.100.085501.

J. J. Arlman and R. Kronig. Investigation of lattice defects by means of X-rays. I. Tin. *Physica*, **10**(10):795 – 800, 1943. doi: 10.1016/S0031-8914(43)80003-3.

R. I. Barabash, G. E. Ice, and P. E. A. Turchi. *Diffuse Scattering and the Fundamental Properties of Materials*. Momentum Press, New York, 2009.

S. Baroni, S. de Gironcoli, A. Dal Corso, and P. Giannozzi. Phonons and related crystal properties from density-functional perturbation theory. *Rev. Mod. Phys.*, **73**:515–562, 2001. doi: 10.1103/RevModPhys.73.515.

T. Bartels-Rausch, V. Bergeron, J. H. E. Cartwright, R. Escribano, J. L. Finney, H. Grothe, P. J. Gutiérrez, J. Haapala, W. F. Kuhs, J. B. C. Pettersson, S. D. Price, C. I. Sainz-Díaz, D. J. Stokes, G. Strazzulla, E. S. Thomson, H. Trinks, and N. Uras-Aytemiz. Ice structures, patterns, and processes: A view across the icefields. *Rev. Mod. Phys.*, **84**:885–944, 2012. doi: 10.1103/RevModPhys.84.885.

J. Bates. Raman spectra of α and β cristobalite. *J. Chem. Phys.*, **57**:4042–4047, 1972. doi: 10.1063/1.1678878.

J. W. Bennet and A. M. Rappe. Pseudopotential database. URL `http://www.sas.upenn.edu/rappegroup/research/pseudo-potential-gga.html`.

S. M. Bennington, J. Li, M. J. Harris, and D. K. Ross. Phonon softening in ice Ih. *Phys. B*, **263–264**(0):396 – 399, 1999. ISSN 0921-4526. doi: 10.1016/S0921-4526(98)01396-9.

A. Bergamin, G. Cavagnero, and G. Mana. Lattice parameter and thermal expansion of monocrystalline silicon. *J. Appl. Phys*, **82**:5396, 1997. doi: 10.1063/1.366308.

J. D. Bernal and R. H. Fowler. A theory of water and ionic solution, with particular reference to hydrogen and hydroxyl ions. *J. Chem. Phys.*, **1**(8):515–548, 1933. doi: 10.1063/1.1749327.

M. N. Beverley and V. M. Nield. Analysis of single-crystal neutron diffuse scattering from ice Ih. *J. Phys. Chem. B*, **101**(32):6188–6191, 1997. doi: 10.1021/jp9632495.

F. Bloch. über die Quantenmechanik der Elektronen in Kristallgittern. *Zeitschrift für Physik*, **52**(7-8):555–600, 1929. ISSN 0044-3328. doi: 10.1007/BF01339455.

M. Born and K. Huang. *Dynamical theory of Crystal lattices*. Oxford University Press, Oxford, 1954.

M. Born and R. Oppenheimer. Zur quantentheorie der molekeln. *Ann. Phys.*, **389**(20):457–484, 1927. ISSN 1521-3889. doi: 10.1002/andp.19273892002.

A. Bosak and D. Chernyshov. On model-free reconstruction of lattice dynamics from thermal diffuse scattering. *Acta Crystallogr., Sect. A*, **64**(Part 5):598–600, 2008. doi: 10.1107/S0108767308020060.

A. Bosak and M. Krisch. Phonon density of states probed by inelastic x-ray scattering. *Phys. Rev. B*, **72**:224305, 2005. doi: 10.1103/PhysRevB.72.224305.

A. Bosak, M. Hoesch, D. Antonangeli, D. Farber, I. Fischer, and M. Krisch. Lattice dynamics of vanadium: Inelastic x-ray scattering measurements. *Phys. Rev. B*, **78**:020301, 2008. doi: 10.1103/PhysRevB.78.020301.

A. Bosak, I. Fischer, M. Krisch, V. Brazhkin, T. Dyuzheva, B. Winkler, D. Wilson, D. Weidner, K. Refson, and V. Milman. Lattice dynamics of stishovite from powder inelastic x-ray scattering. *Geophys. Res. Lett.*, **36**(19), 2009a. doi: 10.1029/2009GL040257.

A. Bosak, M. Hoesch, M. Krisch, D. Chernyshov, P. Pattison, C. Schulze-Briese, B. Winkler, V. Milman, K. Refson, D. Antonangeli, and D. Farber. 3D imaging of the fermi surface by thermal diffuse scattering. *Phys. Rev. Lett.*, **103**:076403, 2009b. doi: 10.1103/PhysRevLett.103.076403.

A. Bosak, M. Krisch, D. Chernyshov, B. Winkler, V. Milman, K. Refson, and C. Schulze-Briese. New insights into the lattice dynamics of α-quartz. *Z. Kristallogr.*, **227**(2):84–91, 2012. doi: 10.1524/zkri.2012.1432.

J. Bouman, J. J. Arlman, and L. L. Van Reijen. Investigations of lattice defects by means of X-rays: IV. the diffuse pattern of tin single crystals. *Physica*, **12** (6):353 – 370, 1946. doi: 10.1016/S0031-8914(46)80055-7.

H. Boysen and W. Adlhart. Resolution corrections in diffuse scattering experiments. *J. Appl. Crystallogr.*, **20**(3):200–209, 1987. doi: 10.1107/S0021889887086825.

B. N. Brockhouse et al. Inelastic scattering of neutrons in solids and liquids. *IAEA, Vienna*, **113**, 1961.

U. Buchenau, N. Nücker, and A. J. Dianoux. Neutron scattering study of the low-frequency vibrations in vitreous silica. *Phys. Rev. Lett.*, **53**:2316–2319, 1984. doi: 10.1103/PhysRevLett.53.2316.

M. J. Buerger and G. E. Klein. Correction of x-ray diffraction intensities for lorentz and polarization factors. *J. Appl. Phys.*, **16**(7):408–418, 1945. doi: 10.1063/1.1707608.

E. Burkel. Phonon spectroscopy by inelastic x-ray scattering. *Rep. Prog. Phys.*, **63**(2):171, 2000. doi: 10.1088/0034-4885/63/2/203.

W. R. Busing and H. A. Levy. Angle calculations for 3- and 4-circle X-ray and neutron diffractometers. *Acta Crystallographica*, **22**(4):457–464, 1967. doi: 10.1107/S0365110X67000970.

J. W. Campbell, M. M. Harding, and B. Kariuki. Spatial-distortion corrections, for laue diffraction patterns recorded on image plates, modelled using polynomial functions. *J. Appl. Crystallogr.*, **28**(1):43–48, 1995. doi: 10.1107/S0021889894008824.

D. M. Ceperley and B. J. Alder. Ground state of the electron gas by a stochastic method. *Phys. Rev. Lett.*, **45**:566–569, 1980. doi: 10.1103/PhysRevLett.45.566.

E. C. T. Chao, E. M. Shoemaker, and B. M. Madsen. First natural occurrence of coesite. *Science*, **132**:3421, 1960. doi: 10.1126/science.132.3421.220.

S. H. Chen. Group-theoretical analysis of lattice vibrations in metallic β-Sn. *Phys. Rev.*, **163**:532–546, 1967. doi: 10.1103/PhysRev.163.532.

A. Chumakov, G. Monaco, A. Fontana, B. Bosak, R. Hermann, D. Bessas, B. Wehinger, A. Crichton, M. Krisch, R. Rüffer, G. Baldi, G. Carini Jr, G. D'Angelo, E. Gilioli, G. Tripodo, M. Zanatta, B. Winkler, V. Milmann, K. Refson, M. Dove, N. Dubrovinskia, L. Dubrovinsky, R. Kedig, and Y. Yue. The role of disorder in the thermodynamics and atomic dynamics of glasses. *submitted*, 2013.

A. I. Chumakov, G. Monaco, A. Monaco, W. A. Crichton, A. Bosak, R. Rüffer, A. Meyer, F. Kargl, L. Comez, D. Fioretto, H. Giefers, S. Roitsch, G. Wortmann, M. H. Manghnani, A. Hushur, Q. Williams, J. Balogh, K. Parliński, P. Jochym, and P. Piekarz. Equivalence of the boson peak in glasses to the transverse acoustic van hove singularity in crystals. *Phys. Rev. Lett.*, **106**:225501, 2011. doi: 10.1103/PhysRevLett.106.225501.

S. Clark, M. Segall, C. Pickard, P. Hasnip, M. Probert, K. Refson, and M. Payne. First principles methods using CASTEP. *Z. Kristallogr.*, **220**:567–570, 2005. doi: 10.1524/zkri.220.5.567.65075.

L. Coes. A new dense crystalline silica. *Science*, **118**:131, 1953. doi: 10.1126/science.118.3057.131.

S. Coh and D. Vanderbilt. Structural stability and lattice dynamics of SiO_2 cristobalite. *Phys. Rev. B*, **78**:054117, 2008. doi: 10.1103/PhysRevB.78.054117.

A. S. Cote, I. Morrison, X. Cui, S. Jenkins, and D. K. Ross. Ab-initio density-functional lattice-dynamics studies of ice. *Can. J. Phys.*, **81**(1-2):115–122, 2003. doi: 10.1139/p03-003.

D. T. Cromer and J. B. Mann. X-ray scattering factors computed from numerical Hartree–Fock wave functions. *Acta Crystallogr., Sect. A*, **24**(2):321–324, 1968. doi: 10.1107/S0567739468000550.

A. Dal Corso and F. Mauri. Wannier and bloch orbital computation of the nonlinear susceptibility. *Phys. Rev. B*, **50**:5756–5759, 1994. doi: 10.1103/PhysRevB.50.5756.

S. de Gironcoli. Lattice dynamics of metals from density-functional perturbation theory. *Phys. Rev. B*, **51**:6773–6776, 1995. doi: 10.1103/PhysRevB.51.6773.

D. de Sanctis, A. Beteva, H. Caserotto, F. Dobias, J. Gabadinho, T. Giraud, A. Gobbo, M. Guijarro, M. Lentini, B. Lavault, T. Mairs, S. McSweeney, S. Petitdemange, V. Rey-Bakaikoa, J. Surr, P. Theveneau, G. Leonard, and C. Mueller-Dieckmann. ID29: a high-intensity highly automated ESRF beamline for macromolecular crystallography experiments exploiting anomalous scattering. *J. Synchrotron Radiat.*, **19**(3):455–461, 2012. doi: 10.1107/S0909049512009715.

D. W. Dean, R. M. Wentzcovitch, N. Keskar, J. R. Chelikowsky, and N. Binggeli. Pressure-induced amorphization in crystalline silica: Soft phonon modes and shear instabilities in coesite. *Phys. Rev. B*, **61**:3303–3309, 2000. doi: 10.1103/PhysRevB.61.3303.

A. Debernardi, S. Baroni, and E. Molinari. Anharmonic phonon lifetimes in semiconductors from density-functional perturbation theory. *Phys. Rev. Lett.*, **75**: 1819–1822, 1995. doi: 10.1103/PhysRevLett.75.1819.

M. A. C. Deviller, M. M. M. P. Matthey, and A. R. De Vroomen. Fermi-surface of white tin from a RAPW interpolation compared with experiment. *Phys. Status Solidi B*, **63**(2):471–484, 1974. doi: 10.1002/pssb.2220630206.

W. A. Dollase. Reinvestigation of the structure of low cristobalite. *Z. Kristallogr.*, **121**(5):369–377, 1965. doi: 10.1524/zkri.1965.121.5.369.

B. Dorner, H. Grimm, and H. Rzany. Phonon dispersion branches in α-quartz. *J. Phys. C: Solid State Phys.*, **13**(36):6607, 1980. doi: 10.1088/0022-3719/13/36/014.

M. T. Dove, A. K. A. Pryde, V. Heine, and K. D. Hammonds. Exotic distributions of rigid unit modes in the reciprocal spaces of framework aluminosilicates. *J. Phys.: Condens. Matter*, **19**(27):275209, 2007. doi: 10.1088/0953-8984/19/27/275209.

L. S. Dubrovinsky, N. A. Dubrovinskaia, V. Prakapenka, F. Seifert, F. Langenhorst, V. Dmitriev, H. P. Weber, and T. Le Bihan. A class of new high-pressure silica polymorphs. *Phys. Earth Planet. Inter.*, **143–144**(0):231 – 240, 2004. doi: 10.1016/j.pepi.2003.06.006.

E. Duval, A. Boukenter, and T. Achibat. Vibrational dynamics and the structure of glasses. *J. Phys.: Condens. Matter*, **2**(51):10227, 1990. doi: 10.1088/0953-8984/2/51/001.

T. I. Dyuzheva, L. M. Lityagina, N. A. Bendeliani, N. A. Nikolaev, and G. I. Dorokhova. Hydrothermal synthesis of coesite (SiO_2). *Crystallogr. Rep.*, **43**(3): 511–513, 1998.

D. L. Farber, M. Krisch, D. Antonangeli, A. Beraud, J. Badro, F. Occelli, and D. Orlikowski. Lattice dynamics of molybdenum at high pressure. *Phys. Rev. Lett.*, **96**:115502, 2006. doi: 10.1103/PhysRevLett.96.115502.

H. Faxén. Die bei Interferenz von Röntgenstrahlen infolge der Wärmebewegung entstehende Streustrahlung. *Z. Phys.*, **17**:266–278, 1923. doi: 10.1007/BF01328684.

F. I. Fedorov. *Theory of Elastic Waves in Crystals*. Plenum Press, New York, 1968.

W. Frank, C. Elsässer, and M. Fähnle. *Ab initio* force-constant method for phonon dispersions in alkali metals. *Phys. Rev. Lett.*, **74**:1791–1794, 1995. doi: 10.1103/PhysRevLett.74.1791.

H. Fukazawa, S. Ikeda, M. Oguro, S. M. Bennington, and S. Mae. Phonon dispersion curves in KOD-doped ice observed by neutron scattering. *J. Chem. Phys.*, **118**(4):1577–1580, 2003. doi: 10.1063/1.1539846.

P. Giannozzi and S. Baroni. Vibrational and dielectric properties of C_{60} from density-functional perturbation theory. *J. Chem. Phys.*, **100**(11):8537–8539, 1994. doi: 10.1063/1.466753.

P. Giannozzi, S. Baroni, N. Bonini, M. Calandra, R. Car, C. Cavazzoni, D. Ceresoli, G. Chiarotti, M. Cococcioni, I. Dabo, A. Dal Corso, S. de Gironcoli, S. Fabris, G. Fratesi, R. Gebauer, U. Gerstmann, C. Gougoussis, A. Kokalj, M. Lazzeri, L. Martin-Samos, N. Marzari, F. Mauri, R. Mazzarello, S. Paolini, A. Pasquarello, L. Paulatto, C. Sbraccia, S. Scandolo, G. Sclauzero, A. Seitsonen, A. Smogunov, P. Umari, and R. Wentzcovitch. QUANTUM ESPRESSO:

a modular and open-source software project for quantum simulations of materials. *J. Phys.: Condens. Matter*, **21**(39):395502, 2009. doi: 10.1088/0953-8984/21/39/395502.

A. Gibaud, D. Harlow, J. B. Hastings, J. P. Hill, and D. Chapman. A high-energy monochromatic laue (monolaue) x-ray diffuse scattering study of $kMnF_3$ using an image plate. *J. Appl. Crystallogr.*, **30**(1):16–20, 1997. doi: 10.1107/S0021889896000696.

G. V. Gibbs, C. T. Prewitt, and K. J. Baldwin. A study of the structural chemistry of coesite. *Z. Kristallogr.*, **145**:108, 2003. doi: 10.1524/zkri.1977.145.1-2.108.

G. Gilat. Existence of an infinity in the frequency distribution $g(\nu)$ of monatomic body-centered cubic crystals. *Phys. Rev.*, **157**:540–543, 1967. doi: 10.1103/PhysRev.157.540.

X. Gonze. First-principles responses of solids to atomic displacements and homogeneous electric fields: Implementation of a conjugate-gradient algorithm. *Phys. Rev. B*, **55**:10337–10354, 1997. doi: 10.1103/PhysRevB.55.10337.

X. Gonze and C. Lee. Dynamical matrices, born effective charges, dielectric permittivity tensors, and interatomic force constants from density-functional perturbation theory. *Phys. Rev. B*, **55**:10355–10368, 1997. doi: 10.1103/PhysRevB.55.10355.

T. S. Grigera, V. Martin-Mayor, G. Parisi, and P. Verrocchio. Phonon interpretation of the 'boson peak' in supercooled liquids. *Nature*, **422**(6929):289–292, 2003. doi: 10.1038/nature01475.

E. L. Gromnitskaya, O. V. Stal'gorova, V. V. Brazhkin, and A. G. Lyapin. Ultrasonic study of the nonequilibrium pressure-temperature diagram of H_2O ice. *Phys. Rev. B*, **64**:094205, 2001. doi: 10.1103/PhysRevB.64.094205.

C. Halcoussis. PhD thesis, Rostock University, 1997.

B. He. *Two-Dimensional X-ray Diffracion*. John Wiley & Sons, Inc. Hoboken, New Jersey, 2008.

F. Hippert, E. Geissler, J. L. Hodeau, E. Leli'evre-Berna, and J. R. Regnard. *Neutron and X-ray Spectroscopy*. Springer, Dordrecht, 2006.

G. Hülsen, C. Brönnimann, and E. F. Eikenberry. Distortion calibration of the PILATUS 1M detector. *Nucl. Instrum. Methods Phys. Res., Sect. A*, **548**(3): 540 – 554, 2005. doi: 10.1016/j.nima.2005.05.032.

P. Hohenberg and W. Kohn. Inhomogeneous electron gas. *Phys. Rev.*, **136**:B864–B871, 1964. doi: 10.1103/PhysRev.136.B864.

M. Holt, Z. Wu, H. Hong, P. Zschack, P. Jemian, J. Tischler, H. Chen, and T. C. Chiang. Determination of phonon dispersions from X-ray transmission scattering: The example of silicon. *Phys. Rev. Lett.*, **83**:3317–3319, 1999. doi: 10.1103/PhysRevLett.83.3317.

M. Holt, P. Zschack, H. Hong, M. Y. Chou, and T. C. Chiang. X-ray studies of phonon softening in $TiSe_2$. *Phys. Rev. Lett.*, **86**:3799–3802, 2001. doi: 10.1103/PhysRevLett.86.3799.

M. Holt, P. Czoschke, H. Hong, P. Zschack, H. K. Birnbaum, and T. C. Chiang. Phonon dispersions in niobium determined by x-ray transmission scattering. *Phys. Rev. B*, **66**:064303, 2002. doi: 10.1103/PhysRevB.66.064303.

A. Ivanov, A. Rumiantsev, N. Mitrofanov, and M. Alba. Low-frequency lattice dynamics of γ-tin. *Phys. B*, **174**(1–4):79 – 82, 1991. doi: 10.1016/0921-4526(91)90581-X.

A. Ivanov, N. Mitrofanov, and A. Rumiantsev. Fermi surface and fine structure of the phonon dispersion curves of white tin. *Phys. B*, **213–214**(0):423 – 426, 1995. doi: 10.1016/0921-4526(95)00177-B.

A. S. Ivanov, A. Y. Rumiantsev, B. Dorner, N. L. Mitrofanov, and V. V. Pushkarev. Lattice dynamics and electron-phonon interaction in γ-tin. *J. Phys. F: Met. Phys.*, **17**(9):1925, 1987. doi: 10.1088/0305-4608/17/9/017.

S. M. Jackson, V. M. Nield, R. W. Whitworth, M. Oguro, and C. C. Wilson. Single-crystal neutron diffraction studies of the structure of ice XI. *The Journal of Physical Chemistry B*, **101**(32):6142–6145, 1997. doi: 10.1021/jp9632551.

L. G. Khvostantsev, L. F. Vereshchagin, and A. P. Novikov. Device of toroid type for high pressure generation. *High Temp. - High Pressures*, **9**:637, 1977.

H. Kimizuka, S. Ogata, and J. Li. Hydrostatic compression and high-pressure elastic constants of coesite silica. *J. Appl. Phys.*, **103**:053506, 2008. doi: 10.1063/1.2888558.

T. Kobayashi and T. Kuroda. Snow crystals. In I. Sunagawa, editor, *Morphology of Crystals*. Terra Scientific Publishing, Tokyo, 1987.

J. Kohanoff. *Electronic Structure Calculaitons for Solids and Molecules*. Cambridge University Press, Cambridge, 2006.

V. Kohn and A. Chumakov. DOS: Evaluation of phonon density of states from nuclear resonant inelastic absorption. *Hyperfine Interact.*, **125**(1-4):205–221, 2000. doi: 10.1023/A:1012689705503.

W. Kohn. Image of the fermi surface in the vibration spectrum of a metal. *Phys. Rev. Lett.*, **2**:393–394, 1959. doi: 10.1103/PhysRevLett.2.393.

W. Kohn and L. J. Sham. Self-consistent equations including exchange and correlation effects. *Phys. Rev.*, **140**:A1133–A1138, 1965. doi: 10.1103/PhysRev.140.A1133.

M. M. Koza, H. Schober, B. Geil, M. Lorenzen, and H. Requardt. Crystalline inelastic response of high-density amorphous ice. *Phys. Rev. B*, **69**:024204, 2004. doi: 10.1103/PhysRevB.69.024204.

P. Kraft, A. Bergamaschi, C. Broennimann, R. Dinapoli, E. F. Eikenberry, B. Henrich, I. Johnson, A. Mozzanica, C. M. Schlepütz, P. R. Willmott, and B. Schmitt. Performance of single-photon-counting PILATUS detector modules. *J. Synchrotron Radiat.*, **16**(3):368–375, 2009. doi: 10.1107/S0909049509009911.

M. Krisch and F. Sette. *Inelastic X-ray Scattering from Phonons. Light Scattering in solids, Novel Materials and Techniques, Topics in Applied Physics 108.* Springer-Verlag, 2007.

R. Kubiak. Evidence for the existence of the γ form of tin. *J. Less-Common Met.*, **116**(2):307 – 311, 1986. doi: 10.1016/0022-5088(86)90663-6.

R. Kubiak and L. K. Crystal-structure and thermal-expansion of In_3Sn and $InSn_4$. *Bull. Acad. Pol. Sci., Ser. Sci. Chim.*, **22**(4):281–286, 1974.

W. F. Kuhs and M. S. Lehmann. Crystalline hydrates. In F. Franks, editor, *Water Science Reviews*. Cambridge University Press, 1986.

W. F. Kuhs, C. Sippel, A. Falenty, and T. C. Hansen. Extent and relevance of stacking disorder in 'ice Ic'. *Proceedings of the National Academy of Sciences*, **109**(52):21259–21264, 2012. doi: 10.1073/pnas.1210331110.

J.-L. Kuo, M. L. Klein, and W. F. Kuhs. The effect of proton disorder on the structure of ice-Ih: A theoretical study. *The Journal of Chemical Physics*, **123** (13):134505, 2005. doi: 10.1063/1.2036971.

L. D. Landau and E. M. Lifshitz. *Statistical Physics, 3.rd Edition*, volume 5 of Course of Theoretical Physics. Pergamon Press, Oxford, 1980.

R. M. F. Leal, S. C. M. Teixeira, V. Rey, V. T. Forsyth, and E. P. Mitchell. Absorption correction based on a three-dimensional model reconstruction from visual images. *J. Appl. Crystallogr.*, **41**(4):729–737, 2008. doi: 10.1107/S0021889808011898.

M. Leroux, M. Le Tacon, M. Calandra, L. Cario, M.-A. Méasson, P. Diener, E. Borrissenko, A. Bosak, and P. Rodière. Anharmonic suppression of charge density waves in 2H-NbS2. *Phys. Rev. B*, **86**:155125, 2012. doi: 10.1103/PhysRevB.86.155125.

L. Levien and C. Prewitt. High-pressure crystal-structure and compressibility of coesite. *Am. Mineral.*, **66**(3-4):324–333, 1981. URL `http://www.minsocam.org/ammin/AM66/AM66_324.pdf`.

J. C. Li, V. M. Nield, D. K. Ross, R. W. Whitworth, C. C. Wilson, and D. A. Keen. Diffuse neutron-scattering study of deuterated ice Ih. *Philos. Mag. B*, **69**(6):1173–1181, 1994. doi: 10.1080/01418639408240187.

E. Lippincott, A. Vanvalkenburg, C. Weir, and E. Bunting. Infrared studies on polymorphs of silicon dioxide and germanium dioxide. *J. Res. Natl. Bur. Stand.*, **61**(1):61–70, 1958.

L. G. Liu, T. P. Mernagh, and W. O. Hibberson. Raman spectra of high-pressure polymorphs of SiO_2 at various temperatures. *Phys. Chem. Miner.*, **24**(6):396–402, 1997. doi: 10.1007/s002690050053.

E. Malsen. X-ray absorption. In *International Tables for Crystallography*, volume C, pages 520–529. IUCR by Kluwer Academic Publisher, 1992.

A. A. Maradudin, E. W. Montroll, G. H. Weiss, and I. I. P. *Theory of lattice dynamics in the harmonic approximation*. Academic Press, 1971.

K. Mark. *Meteorite Craters*. The University of Arizona Press, 1995.

Marresearch GmbH. URL `http://www.marresearch.com/mar345/introduction.html`.

C. Masciovecchio, U. Bergmann, M. Krisch, G. Ruocco, F. Sette, and R. Verbeni. A perfect crystal x-ray analyser with mev energy resolution. *Nucl. Instrum. and Methods in Phys. Res. Sec. B*, **117**(339):181–186, 1996. doi: 10.1016/0168-583X(95)01288-5.

B. T. Matthias, T. H. Geballe, and V. B. Compton. Superconductivity. *Rev. Mod. Phys.*, **35**:1–22, 1963. doi: 10.1103/RevModPhys.35.1.

D. B. McWhan, P. Hu, M. A. Chin, and V. Narayanamurti. Observation of optically excited near-zone-edge phonons in GaAs by diffuse x-ray scattering. *Phys. Rev. B*, **26**:4774–4776, 1982. doi: 10.1103/PhysRevB.26.4774.

M. Merisalo and J. Soininen. Covalency of bonding in β-Sn. *Phys. Rev. B*, **19**: 6289–6294, 1979. doi: 10.1103/PhysRevB.19.6289.

M. Meyer. *Construction of a multi-purpose x-ray CCD detector and its implementation on a 4-circle kappa goniometer*. PhD thesis, Université de Lausanne, 1998.

M. Meyer, G. Onida, M. Palummo, and L. Reining. *Ab initio* pseudopotential calculation of the equilibrium structure of tin monoxide. *Phys. Rev. B*, **64**: 045119, 2001. doi: 10.1103/PhysRevB.64.045119.

A. Mirone and B. Wehinger. ab2tds. *unpublished*, 2012. URL `https://forge.epn-campus.eu/projects/ab2tds`.

P. Mohanty, Y. Fei, and K. Landskron. Synthesis of periodic mesoporous coesite. *J. Am. Chem. Soc.*, **131**(28):9638–9639, 2009. doi: 10.1021/ja903286m.

P. Mohanty, V. Ortalan, N. D. Browning, I. Arslan, Y. Fei, and K. Landskron. Direct formation of mesoporous coesite single crystals from periodic mesoporous silica at extreme pressure. *Angew. Chem., Int. Ed.*, **49**(25):4301–4305, 2010. doi: 10.1002/anie.201001114.

G. Monaco and V. M. Giordano. Breakdown of the debye approximation for the acoustic modes with nanometric wavelengths in glasses. *Proc. Natl. Acad. Sci. U. S. A.*, **106**(10):3659–3663, 2009. doi: 10.1073/pnas.0808965106.

H. J. Monkhorst and J. D. Pack. Special points for brillouin-zone integrations. *Phys. Rev. B*, **13**:5188–5192, 1976. doi: 10.1103/PhysRevB.13.5188.

N. Mounet. *Structural, vibrational and thermodynamical properties of carbon allotropes from first-principles: diamond, graphite, and nanotubes*. PhD thesis, Massachusetts Institute of Technology, 2005.

B. J. Murray, D. A. Knopf, and A. K. Bertram. The formation of cubic ice under conditions relevant to earth's atmosphere. *Nature*, **434**, 2005. doi: 10.1038/nature03403.

M. Oguro and T. Hondoh. Stacking faults in ice crystals. In I. Sunagawa, editor, *Lattice defects in Ice crystals*. Hokkaido University Press, Sapporo, 1988.

H. Ott. Der Einfluss der Temperatur auf die Röntgenstreuung fester Körper nach der Quantenmechanik. *Ann. Phys.*, **415**(2):169–196, 1935. doi: 10.1002/andp.19354150206.

P. G. Owston. Diffuse scattering of X-rays by ice. *Acta Crystallogr.*, **2**(4):222–228, 1949. doi: 10.1107/S0365110X4900059X.

Oxford diffraction Ltd. URL `http://technoinfo.co.uk/catalog/12.html`.

B. Pamuk, J. M. Soler, R. Ramírez, C. P. Herrero, P. W. Stephens, P. B. Allen, and M.-V. Fernández-Serra. Anomalous nuclear quantum effects in ice. *Phys. Rev. Lett.*, **108**:193003, 2012. doi: 10.1103/PhysRevLett.108.193003.

K. Parlinski, Z. Q. Li, and Y. Kawazoe. First-principles determination of the soft mode in cubic ZrO_2. *Phys. Rev. Lett.*, **78**:4063–4066, 1997. doi: 10.1103/PhysRevLett.78.4063.

L. Parratt. Lattice dynamics of white tin. *Proc. R. Soc. Lond. A*, **300**:25–44, 1967.

L. Pauling. The structure and entropy of ice and of other crystals with some randomness of atomic arrangement. *J. Am. Chem. Soc.*, **57**(12):2680–2684, 1935. doi: 10.1021/ja01315a102.

P. Pavone, S. Baroni, and S. de Gironcoli. $\alpha \leftrightarrow \beta$ phase transition in tin: A theoretical study based on density-functional perturbation theory. *Phys. Rev. B*, **57**:10421–10423, 1998. doi: 10.1103/PhysRevB.57.10421.

J. P. Perdew and A. Zunger. Self-interaction correction to density-functional approximations for many-electron systems. *Phys. Rev. B*, **23**:5048–5079, 1981. doi: 10.1103/PhysRevB.23.5048.

J. P. Perdew, K. Burke, and M. Ernzerhof. Generalized gradient approximation made simple. *Phys. Rev. Lett.*, **77**:3865–3868, 1996. doi: 10.1103/PhysRevLett.77.3865.

J. P. Perdew, A. Ruzsinszky, G. I. Csonka, O. A. Vydrov, G. E. Scuseria, L. A. Constantin, X. Zhou, and K. Burke. Restoring the density-gradient expansion for exchange in solids and surfaces. *Phys. Rev. Lett.*, **100**:136406, 2008. doi: 10.1103/PhysRevLett.100.136406.

J. R. Petit, I. Alekhina, and S. Bulat. Antarctica: exploring a subglacial lake and searching for life in an extreme environment. In M. Gargaud, H. Martin, and J. Reisse, editors, *Lectures in Astrobiology*, volume 1 of *Advances in Astrobiology and Biogeophysics*, pages 227–288. Springer, Berlin, 2005.

V. F. Petrenko and R. W. Whitworth. *Physics of ice*. Oxford University Press, 1991.

B. G. Pfrommer, M. Côté, S. G. Louie, and M. L. Cohen. Relaxation of crystals with the quasi-newton method. *J. Comput. Phys.*, **131**(1):233 – 240, 1997. doi: 10.1006/jcph.1996.5612.

R. M. Pick, M. H. Cohen, and R. M. Martin. Microscopic theory of force constants in the adiabatic approximation. *Phys. Rev. B*, **1**:910–920, 1970. doi: 10.1103/PhysRevB.1.910.

J. J. Pluth, J. V. Smith, and J. Faber. Crystal structure of low cristobalite at 10, 293, and 473 K: Variation of framework geometry with temperature. *J. Appl. Phys.*, **57**:1045–1049, 1985. doi: 10.1063/1.334545.

S. C. Prasad and W. A. Wooster. The study of the elastic constants of white tin by diffuse x-ray reflexion. *Acta Crystallogr.*, **8**(11):682–686, 1955. doi: 10.1107/S0365110X55002119.

I. B. Ramsteiner, A. Schöps, H. Reichert, H. Dosch, V. Honkimäki, Z. Zhong, and J. B. Hastings. High-energy X-ray diffuse scattering. *J. Appl. Crystallogr.*, **42** (3):392–400, 2009. doi: 10.1107/S0021889809011492.

G. V. Raynor and J. A. Lee. The tin-rich intermediate phases in the alloys of tin with cadmium, indium and mercury. *Acta Metall.*, **2**(4):616 – 620, 1954. doi: 10.1016/0001-6160(54)90197-2.

K. Refson, P. R. Tulip, and S. J. Clark. Variational density-functional perturbation theory for dielectrics and lattice dynamics. *Phys. Rev. B*, **73**:155114, 2006. doi: 10.1103/PhysRevB.73.155114.

B. Renker. Phonon dispersion in D_2O-ice. *Phys. Lett. A*, **30**(9):493 – 494, 1969. ISSN 0375-9601. doi: 10.1016/0375-9601(69)90265-5.

J. M. Rowe. Crystal dynamics of metallic β-Sn at 110°K. *Phys. Rev.*, **163**:547–551, 1967. doi: 10.1103/PhysRev.163.547.

J. M. Rowe, B. N. Brockhouse, and E. C. Svensson. Lattice dynamics of white tin. *Phys. Rev. Lett.*, **14**:554–556, 1965. doi: 10.1103/PhysRevLett.14.554.

S. Scheidegger, M. A. Estermann, and W. Steurer. Correction of specimen absorption in x-ray diffuse scattering experiments with area-detector systems. *J. Appl. Crystallogr.*, **33**(1):35–48, 2000. doi: 10.1107/S0021889899011929.

W. Schirmacher, G. Diezemann, and C. Ganter. Harmonic vibrational excitations in disordered solids and the "boson peak". *Phys. Rev. Lett.*, **81**:136–139, 1998. doi: 10.1103/PhysRevLett.81.136.

H. Schober, M. M. Koza, A. Tölle, C. Masciovecchio, F. Sette, and F. Fujara. Crystal-like high frequency phonons in the amorphous phases of solid water. *Phys. Rev. Lett.*, **85**:4100–4103, 2000. doi: 10.1103/PhysRevLett.85.4100.

W. Schülke. *Electron dynamics by inelastic X-ray scattering*. Oxford University Press, Oxford, 2005.

S. K. Sharma, J. F. Mammone, and M. F. Nicol. Raman investigation of ring configurations in vitreous silica. *Nature*, **292**(5819):140–141, 1981. doi: 10.1038/292140a0.

V. N. Sigaev, E. N. Smelyanskaya, V. G. Plotnichenko, V. V. Koltashev, A. A. Volkov, and P. Pernice. Low-frequency band at 50 cm^{-1} in the Raman spectrum of cristobalite: identification of similar structural motifs in glasses and crystals of similar composition. *J. Non-Cryst. Solids*, **248**(2-3):141 – 146, 1999. doi: 10.1016/S0022-3093(99)00242-2.

J. R. Smyth, J. V. Smith, G. Artioli, and A. Kvick. Crystal structure of coesite, a high-pressure form of silica, at 15 and 298 k from single-crystal neutron and x-ray diffraction data: test of bonding models. *J. Phys. Chem.*, **91**(4):988–992, 1987. doi: 10.1021/j100288a043.

N. V. Sobolev, B. A. Fursenko, S. V. Goryainov, J. F. Shu, R. J. Hemley, H. K. Mao, and F. R. Boyd. Fossilized high pressure from the earth's deep interior: The coesite-in-diamond barometer. *Proc. Natl. Acad. Sci. U. S. A.*, **97**(22): 11875–11879, 2000. doi: 10.1073/pnas.220408697.

M. Stanton, W. C. Phillips, Y. Li, and K. Kalata. Correcting spatial distortions and nonuniform response in area detectors. *J. Appl. Crystallogr.*, **25**(5):549–558, 1992. doi: 10.1107/S0021889892004035.

D. Strauch and B. Dorner. Phonon eigenvector determination in GaAs by inelastic neutron scattering. *J. Phys. C: Solid State Phys.*, **19**(16):2853, 1986. doi: 10.1088/0022-3719/19/16/006.

D. Strauch and B. Dorner. Lattice dynamics of α-quartz. I. experiment. *J. Phys.: Condens. Matter*, **5**(34):6149, 1993. doi: 10.1088/0953-8984/5/34/003.

T. Strässle, A. M. Saitta, S. Klotz, and M. Braden. Phonon dispersion of ice under pressure. *Phys. Rev. Lett.*, **93**:225901, 2004. doi: 10.1103/PhysRevLett.93.225901.

I. P. Swainson, M. T. Dove, and D. C. Palmer. Infrared and Raman spectroscopy studies of the $\alpha - \beta$ phase transition in cristobalite. *Phys. Chem. Miner.*, **30** (6):353–365, 2003. doi: 10.1007/s00269-003-0320-8.

H. E. Swanson and E. Tatge. Standard x-ray diffraction powder patterns. *Natl. Bur. Stand.*, **539**:1–95, 1953.

M. Takahashi, K. Ohshima, and Y. Noda. Measurement of diffuse scattering in β-tin single crystal. *Nihon Genshiryoku Kenkyu Kaihatsu Kiko JAEA- Review*, 2006.

H. Tanaka. Physical origin of the boson peak deduced from a two-order-parameter model of liquid. *J. Phys. Soc. Jpn.*, **70**(5):1178–1181, 2001. doi: 10.1143/JPSJ.70.1178.

S. N. Taraskin, Y. L. Loh, G. Natarajan, and S. R. Elliott. Origin of the boson peak in systems with lattice disorder. *Phys. Rev. Lett.*, **86**:1255–1258, 2001. doi: 10.1103/PhysRevLett.86.1255.

M. Trigo, J. Chen, V. H. Vishwanath, Y. M. Sheu, T. Graber, R. Henning, and D. A. Reis. Imaging nonequilibrium atomic vibrations with x-ray diffuse scattering. *Phys. Rev. B*, **82**:235205, 2010. doi: 10.1103/PhysRevB.82.235205.

K. Umemoto, R. M. Wentzcovitch, S. Baroni, and S. de Gironcoli. Anomalous pressure-induced transition(s) in ice XI. *Phys. Rev. Lett.*, **92**:105502, 2004. doi: 10.1103/PhysRevLett.92.105502.

L. Van Hove. The occurrence of singularities in the elastic frequency distribution of a crystal. *Phys. Rev.*, **89**:1189–1193, 1953. doi: 10.1103/PhysRev.89.1189.

I. Waller. Zur Frage der Einwirkung der Wärmebewegung auf die Interferenz von Röntgenstrahlen. *Z. Phys.*, **17**:398–408, 1923. doi: 10.1007/BF01328696.

B. E. Warren. *X-ray Diffraction*. Addison-Weley, Reading, 1966.

D. J. Weidner and H. R. Carleton. Elasticity of coesite. *J. Geophys. Res.*, **82**(8): 1334–1346, 1977. doi: 10.1029/JB082i008p01334.

M. H. Whangbo, E. Canadell, P. Foury, and J. P. Pouget. Hidden fermi surface nesting and charge density wave instability in low-dimensional metals. *Science*, **252**(5002):96–98, 1991. doi: 10.1126/science.252.5002.96.

Q. Williams, R. Hemley, M. Kruger, and R. Jeanloz. High-pressure infrared sepctra of α-quartz, coesite, stishovite and silica glass. *J. Geophys. Res.*, **98 B12**:22,157–22,170, 2000. doi: 10.1029/93JB02171.

B. T. M. Willis and C. J. Carlile. *Experimental Neutron Scattering*. Oxford University Pres, Oxford, 2009.

B. T. M. Willis and A. W. Pryor. *Thermal Vibrations in Crystallography*. Cambridge University Press, Cambridge, 1975.

R. L. Withers, J. G. Thompson, and T. R. Welberry. The structure and microstructure of α-cristobalite and its relationship to β-cristobalite. *Phys. Chem. Minerals*, **16**(6):517–523, 1989. doi: 10.1007/BF00202206.

W. A. Wooster. *Diffuse X-ray Reflections from Crystals*. Oxford University Press, 1962.

R. Xu, J. Wong, P. Zschack, H. Hong, and T.-C. Chiang. Soft phonons in δ-phase plutonium near the $\delta - \alpha'$ transition. *Europhys. Lett.*, **82**(2):26001, 2008. doi: 10.1209/0295-5075/82/26001.

R. Xu, H. Hong, and T. C. Chiang. Probing phonons and phase transitions in solids with x-ray thermal diffuse scattering. In R. Barabash, G. Ice, and P. E. A. Turchi, editors, *Diffuse Scattering and the Fundamental Properties of Materials*. Momentum Press, New York, 2009.

R. Q. Xu and T. C. Chiang. Determination of phonon dispersion relations by x-ray thermal diffuse scattering. *Z. Kristallogr.*, **220**(12):1009–1016, 2005. doi: 10.1524/zkri.2005.220.12.1009.

M. T. Yin and M. L. Cohen. Microscopic theory of the phase transformation and lattice dynamics of Si. *Phys. Rev. Lett.*, **45**:1004–1007, 1980. doi: 10.1103/PhysRevLett.45.1004.

List of publications

H. Reichert, F. Bencivenga, B. Wehinger, M. Krisch, F. Sette, and H. Dosch. High-frequency subsurface and bulk dynamics of liquid indium. *Phys. Rev. Lett.*, **98**: 096104, 2007. doi: 10.1103/PhysRevLett.98.096104.

B. Wehinger, M. Krisch, and H. Reichert. High-frequency dynamics in the near-surface region studied by inelastic x-ray scattering: the case of liquid indium. *New Journal of Physics*, **13**(2):023021, 2011. doi: 10.1088/1367-2630/13/2/023021.

G. Baldi, M. Zanatta, E. Gilioli, V. Milman, K. Refson, B. Wehinger, B. Winkler, A. Fontana, and G. Monaco. Emergence of crystal-like atomic dynamics in glasses at the nanometer scale. *Phys. Rev. Lett.*, **110**:185503, 2013. doi: 10.1103/PhysRevLett.110.185503.

A. Chumakov, G. Monaco, A. Fontana, B. Bosak, R. Hermann, D. Bessas, B. Wehinger, A. Crichton, M. Krisch, R. Rüffer, G. Baldi, G. Carini Jr, G. D'Angelo, E. Gilioli, G. Tripodo, M. Zanatta, B. Winkler, V. Milmann, K. Refson, M. Dove, N. Dubrovinskia, L. Dubrovinsky, R. Kedig, and Y. Yue. The role of disorder in the thermodynamics and atomic dynamics of glasses. *submitted*.

B. Wehinger, A. Bosak, A. Chumakov, A. Mirone, B. Winkler, N. Dubrovinskaia, V. Brazhkin, and T. Dyuzheva and M. Krisch. Lattice dynamics of coesite. *J. Phys.: Condens. Matter*, **25**:275401, 2013 doi: 10.1088/0953-8984/25/27/275401.

B. Wehinger, A. Bosak, G. Piccolboni, D. Chernychov, K. Refson, A. Ivanov, A. Rumiantsev and M. Krisch. Diffuse scattering in metallic tin polymorphs. *submitted*. preprint: `http://arxiv.org/abs/1310.3080`.

Award

Best poster prize at ESRF Science and students days, Val Cenis, 2011

Acknowledgments

I would like to thank everybody supporting my work! First Alexeï Bosak and Michael Krisch for supervising my thesis. Your support in both scientific and administrative questions was excellent. I appreciated the way you have supported me in working independently and developing my own ideas. Thank you for your help in carrying out the experimental work and your feedback on data analysis and theoretical calculations. I am looking very much forward to future common projects and long lasting collaborations.

In particular I would like to thank Harald Reichert for mentoring this thesis. I am pleased by the fact that you were all the time available for discussions and that you have taken so much time for me. Thank you for accompanying my scientific carrier from the very beginning with my first experiences as student assistant at the Max-Planck Institut für Metallforschung Stuttgart. A big thank you at this point also to Sigrid Berner and Ursula Wehinger for continuous interest on my curriculum vitae.

I would like to thank Alessandro Mirone for a very fruitful collaboration. Thank you for all your help in programming and for finding the computational methods which were required for the calculation of the scattering intensities and data analysis. I am pleased by your sophisticated way of programming involving also the very careful integration of all the theoretical formalism.

Thank you Keith Refson for your careful teaching on *ab initio* calculations. It was a real pleasure to work with you and I am looking forward to future collaboration. Thank you also for critical proofreading part of the thesis and publications.

Sasha Chumakov, I would like to thank you very much for all our fruitful discussions. I acknowledge in particular that you have provided me the IXS powder measurements of the silica polymorphs including the very careful analysis of these data.

It was a pleasure to work with and supervise my students Martin Ruminy and Giuseppe Piccolboni. Thank you for the fruitful work, all your questions and ideas. I wish you all the best for your future.

Thank you Dmitry Chernyshov for providing beam time for the diffuse scattering experiments, our fruitful discussions and your help on the work on tin and

ice.

Thank you Björn Winkler for our discussions on lattice dynamics calculations and your input to the work on coesite.

Thank you Daniele de Sanctis and Clemens Schulze-Brise for providing beam time for the diffuse scattering experiments.

Denis Gambetti, I would like to thank you very much for your excellent technical support. Your expertise was indispensable for the experiments. I was pleased to work with you.

Thank you Roberto Verbeni and Christian Henriquet your professional technical support and all the ideas for the realisation of my experiments.

Thank you Gaston Garbarino, Jeroen Jacobs, Sylvain Petitgirard and Ashkan Salamat for teaching me the use of high pressure equipment. Thank you very much for your patience and help. Thank you Gaston, Michael Hanfland and Mohamed Mezouar for providing beamtime and help in the sample characterization in the high pressure related studies and for fruitful scientific discussions.

Thank you Leonid Dubrovinsky, Natalia Dubrovinskaia, Vadim Brazhkin and Tatiana Dyuzheva for the synthesis of the coesite crystal and powder samples.

Thank you Alexander Ivanov and Alexander Rumiantsev for providing the single crystals of the tin polymorphs and your input on the tin work.

Erik Gallo, I would like to thank you for fruitful discussions on electronic structure calculations and many thanks for all the nice moments we had as office mates.

I would like to thank Elena Borissenko, Roman Burkovsky and Andy Walters for very fruitful team work at ID28 and all the discussions we had.

Thank you Gaël Goret, Gabrielle Förstner, Claudio Ferrero, Jerome Kieffer and Jean-Noël Bouvier for help in programming and excellent support in IT related questions.

I would like to thank Giacomo Baldi, Mark Jhonson, Maria Grazia Izzo, Alain Pasturel, Noël Jakse, and Matthias Gutmann for fruitful collaboration and discussions.

Thank you Victor Ezhov and Sergey Bulat for providing the excellent pieces of ice single crystals.

I would like acknowledge the courtesy of the Harvard Mineralogical museum and personnaly the collection curator Dr. Raquel Alonso-Perez for the high quality pieces of natural cristobalite crystals.

Thank you Alexeï, Michael, Keith, Pierre Ribault, Elena, Gilda Gaborieau, Isabelle Combe and Thomas Forrest for careful proof reading and constructive comments on the manuscript.

Thanks to the current and former members of the ESRF PhD committee, it was a pleasure to work with you Erika, Raphael, Aryan and Sri. At this point a big

thank you to Harald Reichert, Michael Krisch and Gilles Cezanne for supporting our PhD committee.

A very big thank you to my family, Fritz, Petra, Hannes, Paulina and Katharina. Thank you for supporting me all along my studies, from Stuttgart via Uppsala to Grenoble. Thank you that I can always rely on you.

I would like to thank all my friends making life enjoyable outside the Synchrotron, I would like to thank Tommy, Vratia, Bianca, Igor, Genia, Assia, Karel, Sylvain, Laura, Marco, Gaëtan, Dominik, Cedric, Claire, Bogdan, Cecile, Guiseppe, Anthony, Alexis, Claudia, Marta, Alissia, Sarah, Antoine, Martin, Elisa and Sebastian for all the nice moments we spent together.

Thank you Paola for your patience and full support.